MULTI-PLATFORM HYPERSPECTRAL TARGET DETECTION AND MODELLING IN DYNAMIC ATMOSPHERIC CONDITIONS

A thesis submitted

in partial fulfillment for the degree of

Doctor of Philosophy

by

SUDHANSHU SHEKHAR JHA

Department of Earth and Space Sciences

INDIAN INSTITUTE OF SPACE SCIENCE AND TECHNOLOGY

Thiruvananthapuram – 695547

June - 2021

CERTIFICATE

This is to certify that the thesis titled **MULTI-PLATFORM HYPERSPECTRAL TARGET DETECTION AND MODELLING IN DYNAMIC ATMOSPHERIC CONDITIONS** submitted by Mr. Sudhanshu Shekhar Jha to the Indian Institute of Space Science and Technology, Thiruvananthapuram, for the award of the degree of Doctor of Philosophy is a bonafide record of the research work done by him under my supervision. The contents of this thesis, in full, or in parts, have not been submitted to any other Institute or University for the award of any degree or diploma.

Dr. Rama Rao Nidamanuri

Professor (Remote sensing & Image processing)

Supervisor

Place: Thiruvananthapuram

June 2021

Counter signature of HoD with seal.

DECLARATION

I declare that this thesis titled **MULTI-PLATFORM HYPERSPECTRAL TARGET DETECTION AND MODELLING IN DYNAMIC ATMOSPHERIC CONDITIONS** submitted in fulfillment of the Degree of Doctor of Philosophy is a record of original work carried out by me under the supervision of **Dr. Rama Rao Nidamanuri**, and has not formed the basis for the award of any degree, diploma, associateship, fellowship or other titles in this or any other Institution or University of higher learning. In keeping with the ethical practice in reporting scientific information, due acknowledgments have been made wherever the findings of others have been cited.

Mr. Sudhanshu Shekhar Jha
SC16D055

Place: Thiruvananthapuram
June 2021

ACKNOWLEDGEMENTS

My Ph.D. journey is coming to an end, and looking back, I realise now that it would not have been possible to walk this path without the support and encouragement from several persons around me. I want to acknowledge the following individuals who have, in many ways, helped me reach where I stand today.

First and foremost, I express my most profound sense of gratitude and indebtedness to my thesis supervisor Prof. Rama Rao Nidamanuri, for his continuous support, encouragement, valuable research directions, and insightful discussions. Although I find myself at shorts of word to thank him, I am grateful to him for shaping and channelling my thought process towards becoming an independent researcher.

I thank my Doctoral committee members: Prof. B S Daya Sagar, Prof. K. Kurien Issac, Dr. L Gnanappazham, and Dr. Samir Mandal, for their encouragement and insightful comments. I extend my thanks to Prof. Anandmayee Tej for her initial support at the beginning of this research work. I also thank Prof. Raju K. George for providing his critical reviews on this research. I thank the thesis reviewers and the anonymous journal reviewers for their valuable comments and suggestions.

I am grateful to Dr. V. K. Dadhwal, Director, IIST, for providing me the opportunity to carry out my research work at IIST and his insightful discussions on several research problems. I thank Dr. A.M.Ramiya for her pragmatic suggestions in the early days of my doctoral study. I thank the staff members at the Department of Earth and Space Sciences (Ms. Divya, Ms. Aswathi, Ms.Celin, and Ms. Shalini) for their kind support for making a conducive ecosystem for this research work to be pursued and completed. I thank all the other staff members at IIST for making my stay period peaceful.

I would like to express my gratitude to my lab colleagues cum my friends Mr. Manohar Kumar C.V.S.S, Mr. Dubacharla Gyaneshwar, and Ms.Reji for helping me to

carry out my experimental fieldwork successfully. I thank my seniors, Dr. Dhaniya S. Pankaj and Dr. Gopakumar, for their kind gesture at the time of joining the department. I thank all the other master's students who have been a part of this lab throughout my stay at IIST to make the lab's environment lively and have fruitful discussions on several research ideas. I thank my friends - Krishna, Vinod, Jogender, and Deeraj for making my stay pleasant at IIST. I am thankful to Dr. Mili Ghosh (Associate Professor, Remote Sensing, BIT Mesra, Ranchi) for her constant motivation and support throughout my academic pursuits in the field of Remote Sensing.

Finding the right words to express my sense of indebtedness to my parents – Mr. Harishchandra Jha and Ms. Anita Jha, for their unconditional love and constant support throughout my academic pursuits is difficult. I thank them for shaping my thought process and develop a sense of critical thinking. As taught by my father, I never knew that the habit of questioning everything would someday prove to be an essential quality a research candidate must possess. I am grateful to my brother - Dr. Himanshu Shekhar Jha, and sisters- Ms. Nibha Kumar, Dr. Kumari Jyotsna, and Ms. Kanchan Jha, for all their love and guidance as senior Ph.D. fellows in our family.

Lastly, I would like to extend my acknowledgment for the financial support by the Department of Science and Technology (DST), New Delhi, Government of India, towards the completion of this thesis.

Sudhanshu Shekhar Jha
Thiruvananthapuram

ABSTRACT

Target detection in remote sensing imagery, mapping of sparsely distributed materials, has vital applications in defence security and surveillance, mineral exploration, agriculture, environmental monitoring, etc. The detection probability and the quality of retrievals are functions of various parameters of the sensor, platform, target-background dynamics, targets' spectral contrast, and atmospheric compensation efficiency. A comprehensive approach to analyse the effect of atmospheric processes and target environment for the detection of an engineered target in hyperspectral imagery is critical for real-time remote sensing-based target detection systems. The overall aim of the thesis is to analyse target detection in hyperspectral imagery under the complex atmospheric and imaging environment. Under this overarching aim, the objective of this thesis is threefold. The first objective is to explore the different aspects of a radiative transfer model which is used for modelling the atmospheric parameters for atmospheric correction of remote sensing data. The second objective is to conduct an experimental analysis of the target detection systems with respect to target positioning and different background setting. Finally, we analyse the target detection performance under the influence of the various combinations of atmospheric conditions.

As part of the first objective, we have developed an open-end atmospheric correction scheme named Flexible Atmospheric Compensation Technique (FACT) based on open source Second Simulation of the Satellite Signal in the Solar Spectrum (6S) radiative transfer model (RTM). The proposed FACT scheme utilizes a look-up architecture for simulating the responses of the RT model for various input parameters' combinations. The proposed FACT scheme has been evaluated exhaustively using spatio-spectral statistical error measures by comparing the performance with widely used atmospheric correction models. Results confirm that the proposed FACT scheme offers accuracy of about 95% for hyperspectral imaging sensors and close to 98% for multispectral imaging sensors. To evaluate the target detection in complex scenarios and background conditions, we acquired a benchmark multi-platform hyperspectral and multispectral remote sensing dataset named as 'Gudalur Spectral Target Detection

(GST-D)' dataset. Positioning artificial targets on different surface backgrounds, we acquired remote sensing data by terrestrial, airborne, and space-borne sensors. Various statistical and subspace detection algorithms were applied on the benchmark dataset for the detection of targets, considering the different sources of reference target spectra, background, and spectral continuity across the platforms. We validated the detection results using the receiver operation curve (ROC) for different cases of detection algorithms and imaging platforms. Results indicate, for some combinations of algorithms and imaging platforms, consistent detection of specific material targets with a detection rate of about 80%.

Finally, we carried out a quantitative assessment of atmospheric parameters' influence on the detectability of engineered targets. Specifically, critical atmospheric parameters such as aerosol optical thickness (AOT), standard atmospheric profiles, and standard aerosol models are considered to quantify their influence on top-of-atmospheric (TOA) radiance signal. We formulated the radiance spectral library by simulating TOA radiance spectra using the 6S RTM. We have considered two cases of target radiance spectra simulation, i.e., (i) corresponding to a grid of different AOT values for a predefined atmospheric and aerosol profile, and (ii) corresponding to varying combinations of atmospheric and aerosol profiles at a given AOT. The detection results indicate that change in the magnitude of AOT across atmospheric models has decision-bearing implications on the overall accuracy. The selection of the wrong atmospheric profile can potentially aggravate the numbers of FAs produced by a detection algorithm.

The methodological approaches for designing an open-source atmospheric correction model and findings related to spectral target detection are the significant contributions of this thesis. The benchmark dataset generated in this work is a valuable resource for addressing intriguing questions in target detection using hyperspectral imagery from a realistic landscape perspective. Overall, the thesis provides an insight into why there is an impending demand for better atmospheric correction models, how the atmospheric variables are related to underlying problems of detecting engineered materials, and, finally, highlights the role of atmospheric modelling for target detection systems.

Table of Contents

CERTIFICATE ..... **i**

DECLARATION ..... **iii**

ACKNOWLEDGEMENTS ..... **v**

ABSTRACT ..... **vii**

LIST OF TABLES ..... **xv**

LIST OF FIGURES ..... **xvii**

ABBREVIATIONS ..... **xxv**

1 INTRODUCTION **1**

1.1 Hyperspectral imaging spectroscopy 1

1.2 Atmospheric compensation in target detection 2

1.3 Target detection in hyperspectral imagery 3

1.4 Motivation and challenges 5

1.5 Research objectives 9

1.6 Structure of the Thesis 10

2 TARGET DETECTION ALGORITHMS: THEORETICAL BACKGROUND **13**

2.1 Target detection overview 13

2.2 Radiative transfer theory 15

2.3 Target detection methods 17

2.3.1 Spectral Angle Mapper (SAM) 19

2.3.2 Matched Filter (MF) 20

2.3.3 Adaptive Cosine Estimator (ACE) 21

2.3.4 Constrained Energy Minimization (CEM) 22

2.3.5 Orthogonal subspace projection (OSP) 23

2.3.6 Target constrained interference minimization filter (TCIMF) 24
2.4 Atmospheric parameters and target detection 24
2.5 Chapter Conclusions 26
3 REGION SENSITIVE ATMOSPHERIC CORRECTION MODEL 27
3.1 Introduction 27
3.2 Methodology 30
3.2.1 6S atmospheric correction scheme 30
3.2.2 Look-up table design 31
3.2.3 Aerosol optical thickness (AOT) estimation 32
3.2.4 Water vapour estimation 35
3.2.5 Experimental implementation 36
3.2.6 Datasets 37
3.2.7 Quantitative and comparative evaluation of the performance of FACT 37
3.3 Results and Analysis 38
3.3.1 Atmospheric correction of the AVIRIS-NG 39
3.3.2 Atmospheric correction of the Hyperion imagery 42
3.3.3 Atmospheric correction of the LANDSAT-8 OLI imagery 44
3.3.4 Atmospheric correction of the WorldView-3 imagery 46
3.3.5 Spectral-statistical performance of FACT 47
3.4 Discussion 50
3.5 Chapter Conclusions 52
4 ENGINEERED MATERIAL TARGET DETECTION USING MULTI-PLATFORM REMOTE SENSING SETUP 53
4.1 Introduction 53
4.2 Materials and Methods 55
4.2.1 Experimental Design 55
4.2.2 Data pre-processing 57

4.2.2.1 Reference Spectral Data Sources and Pre-Processing 57
4.2.2.2 Pre-Processing of Airborne and Spaceborne Imagery 58
4.2.3 Experimental Implementation of Target Detection 59
4.2.3.1 Target Detection Algorithms 60
4.2.4 Validation, and Quantitative Spectral Analysis 61
4.3 Results 63
4.3.1 In-Situ Measurements as Reference Target Spectra 64
4.3.1.1 Target Detection in Airborne Hyperspectral Imagery 64
4.3.1.2 Target Detection in Spaceborne Remote Sensing Imagery 67
4.3.2 Ground-Based Hyperspectral Imagery (THI) as Reference Target Spectra 69
4.3.2.1 Target Detection in Airborne Hyperspectral Imagery 69
4.3.2.2 Target Detection in Spaceborne Remote Sensing Imagery 71
4.3.3 Target Reference Spectra from the Airborne Hyperspectral Imagery 73
4.3.3.1 Target Detection in Airborne Hyperspectral Imagery 73
4.3.3.2 Target Detection in Spaceborne Multispectral Imagery 75
4.3.4 Target Reference Spectra from the Spaceborne Multispectral Imagery 77
4.3.5 Quantitative Spectral Similarity Analysis 78
4.4 Discussion 81
4.4.1 Spectral Conformity of the Reference Target Spectra from Ground to Spaceborne Platform 82
4.4.2 Target - Background Interaction: Role of Context 84
4.4.3 Detection Algorithms and their Functional Categorization 85
4.4.4 Key Elements of Influence in Target Detection 87
4.4.5 Experimental Dataset 89
4.5 Chapter Conclusions 89

5 INFLUENCE OF ATMOSPHERIC MODELLING ON SPECTRAL TARGET DETECTION IN MULTI-PLATFORM REMOTE SENSING DATA..... 91

5.1 Introduction 91

5.2 Materials and methods 94

5.2.1 Data pre-processing: reference target spectra and imagery pre-processing 94

5.2.2 Target signal simulation: Atmospheric processor 95

5.2.3 Target detection algorithms 97

5.2.4 Quantitative evaluation of detection performance and spectral analysis 97

5.3 Results 98

5.3.1 Target Detection performance from airborne imagery for simulated target spectra induced by AOT and atmospheric model assumption 99

5.3.1.1 Target detection performance under varying AOT condition 99

5.3.1.1.1 Detection statistics for point-based field spectra 99

5.3.1.1.2 Detection statistics for pixel-based target spectra 101

5.3.1.2 Target detection performance as a function of standard aerosol models for different standard atmospheric models at various AOT values 102

5.3.1.2.1 Detection statistics for point-based field spectra 102

5.3.1.2.2 Detection statistics for pixel-based target spectra 107

5.3.2 Spectral target detection from space-borne imagery for simulated target spectra induced by AOT and atmospheric model assumption 109

5.3.2.1 Target detection performance under varying AOT condition 109

5.3.2.1.1 Detection statistics for point-based field spectra 109

5.3.2.1.2 Detection statistics for pixel-based THI spectra 110

5.3.2.2 Target detection performance as a function of standard aerosol models for different standard atmospheric models at various AOT values 112

5.3.2.2.1 Detection statistics for point-based field spectra 112

5.3.2.2.1 Detection statistics for pixel-based THI spectra 113

5.3.3 Quantitative spectral similarity analysis of simulated Vs. image spectra 115

5.4 Discussion 117

5.4.1 Influence of spectral variation caused by varying AOT assumption on detection performance 118

5.4.2 Influence of atmospheric model assumption and respective mismatch on target detection performance..... 119

5.5 Chapter Conclusions 120

SUMMARY, CONCLUSIONS, AND FUTURE DIRECTIONS 123

6.1 Summary of the Chapters 123

6.2 Major Contributions..... 125

6.3 Recommendations for Future Research 126

REFERENCES 127

LIST OF PUBLICATIONS BASED ON THESIS 145

Papers in peer reviewed international journals..... 145

Conference Proceedings 145

LIST OF TABLES

1.1 List of a few portable hyperspectral sensors with their spectral properties and weight. ……... 7

3.1 Design of the LUT for the development of FACT (6S based) atmospheric correction method. …… 33

3.2 Datasets used for evaluation of the proposed FACT. …… 37

3.3 Spatial-Error statistics for the subset of different satellite imagery. ……..... 43

4.1 Target materials and naming convention used in the chapter. ……. 56

4.2 Spectral similarity measures between the point-based in-situ target reference spectra and the corresponding airborne, and space-borne target image spectra (spectral angle (SA) is measured in degrees and spectral gradient angle (SGA) in radians) Values in bold are statistically significant. ……. 80

4.3 Spectral similarity between the THI target reference spectra and the corresponding airborne, and space-borne target image spectra (SA is measured in degrees and SGA in radians). Values in bold are statistically significant. ……. 80

4.4 Spectral similarity between the airborne target reference spectra and the space-borne target image spectra (SA is measured in degrees and SGA in radians). Values in bold are statistically significant. ……..... 80

LIST OF FIGURES

1.1	Example of hyperspectral imagery with representative vegetation, soil, and road feature spectra. …….	2
1.2	Atmospheric processes showing scattering and absorbing components affecting the radiance reaching the remote sensors...	4
1.3	Different modes of the spectral target detection. …….	5
2.1	Spectral target detection chain for engineered materials……..	14
3.1	An overall architectural framework for the development of FACT (6S based) atmospheric correction method. ……	31
3.2	Results of atmospheric correction of AVIRIS-NG imagery: (*a*) – (*c*) False Colour Composites of the corrected imagery from the proposed FACT, FLAASH and NASA JPL's atmospheric correction scheme respectively; (*d*) – (*f*) Spatial –Mean Absolute Error (S-MAE) image between the proposed FACT-FLAASH, FLAASH-NASA JPL's and FACT-NASA JPL's scheme respectively. …….....	40
3.3	Results of atmospheric correction of AVIRIS-NG imagery: (*a*) – (*c*) False Colour Composites of the corrected imagery from the proposed FACT, FLAASH and NASA JPL's atmospheric correction scheme respectively; (*d*) – (*f*) Spatial – Root Mean Square Error (S-RMSE) image between the proposed FACT-FLAASH, FLAASH-NASA JPL's and FACT-NASA JPL's scheme respectively. ..…….	41
3.4	The (*a*) spatial-MAE and (*b*) spatial-RMSE histogram for the AVIRIS-NG corrected imagery by FLAASH, the proposed FACT and NASA JPL's correction method. ……	41
3.5	Results of atmospheric correction of Hyperion imagery: (*a*) False Colour Composites of the corrected imagery from the proposed FACT, (*b*) Mean Absolute error (*c*) and Root Mean Square Error image between the proposed FACT and FLAASH atmospheric correction method. ……..	44
3.6	The (*a*) spatial-MAE and (*b*) spatial-RMSE histogram for the HYPERION EO-1 imagery calculated between atmospherically corrected image by FLAASH and the proposed FACT. ……..	44
3.7	Results of atmospheric correction of LADSAT-8 OLI imagery: (*a*) False Colour Composites of the corrected imagery from the proposed FACT, (*b*) Mean Absolute error (*c*) and Root Mean	45

Square Error image between the proposed FACT and FLAASH atmospheric correction method. ……...

3.8 The (*a*) spatial-MAE and (*b*) spatial-RMSE histogram for the LANDSAT-8 OLI imagery calculated between atmospherically corrected image by FLAASH and the proposed FACT. …….. 45

3.9 Results of atmospheric correction of WorldView-3 imagery: (*a*) False Colour Composites of the corrected imagery from the proposed FACT, (*b*) Mean Absolute error (*c*) and Root Mean Square Error image between the proposed FACT and FLAASH atmospheric correction method. …….. 46

3.10 The (*a*) spatial-MAE and (*b*) spatial-RMSE histogram for the WorldView-3 imagery calculated between atmospherically corrected image by FLAASH and the proposed FACT. …….. 47

3.11 A spectral analysis (band wise RMSE calculation) for the imagery data of (*a*) AVIRIS-NG (*b*) Hyperion (*c*) LANDSAT-8 OLI and (*d*) WorldView-3 corrected by the FLAASH, the NASA JPL's and the proposed FACT correction method in case of AVIRIS-NG and by the FLAASH and the proposed FACT in other three cases. …….. 49

4.1 Conceptual design of the experimental set up used for the acquisition of multi-platform remote sensing data. …….. 56

4.2 (a) True color composite of the AVIRIS-NG hyperspectral imagery with the locations of the artificial targets earmarked; (b) location of targets—N3Y and N4B; (c) location of targets—C1W, N1G, and N2R; (d) ground truth map, and (e–f) enlarged view of the ground truth map for different targets. Field photographs (g–k) showing the artificial targets placed in the study area for imagery acquisition. ……... 57

4.3 Reference spectral signatures of the artificial target materials acquired from (a) in-situ point, and (b) in-situ pixel reflectance measurements. ……. 59

4.4 Methodological framework adopted for the target detection in multi-platform remote sensing imagery. …….. 60

4.5 Target detection performance comparison in airborne imagery for the in-situ target reference spectra. ROC for the detection from spectral angle SAM, ACE, CEM, and MF for the (a) N1G, (b) N2R, (c) C1W, (d) N3Y, and (e) N4B targets. ROC curves for the detection from OSP and TCIMF for the N1G, N2R, C1W, N3Y, and N4B targets for (f–j) 5, (k–o) 10, and (p–t) 15 background materials. …….. 66

4.6 Target detection score image from (a) airborne imagery using in-situ reference target spectra, and the enlarged detection score footprint for (b) N3Y, (c) N4B, (d) N1G, (e) N2R, and (f) C1W target (In all the target detection score images, a brighter pixel 66

indicates a higher target detection score and thus a higher probability for it to be declared as a target)……..

4.7 Target detection performance comparison from space-borne imagery for the in-situ target reference spectra. ROC curves for the detection from SAM, ACE, CEM, and MF for the (a) N1G, (b) N2R, (c) N3Y, (d) C1W, and (e) N4B targets. ROC curves for the subspace-based detector OSP and TCIMF for the N1G, N2R, N3Y, C1W, and N4B targets for (f–j) 5, (k–o) 10, and (p–t) 15 endmember/background materials. …….. 68

4.8 Target detection score image (a) from space-borne imagery using in-situ target reference spectrum and the enlarged detection score footprint for (b) N3Y, (c) N4B, (d) N1G, (e) N2R, and (f) C1W targets. …… 68

4.9 Target detection performance comparison in airborne imagery for the terrestrial hyperspectral imager (THI) target reference spectra. ROC curves for the detection from SAM, ACE, CEM, and MF for the (a) N1G, (b) N2R, (c) N3Y, and (d) N4B targets. ROC curves for the subspace-based detector OSP and TCIMF for the N1G, N2R, N3Y, and N4B targets for (e–h) 5, (i-l) 10, and (m–p) 15 endmember/background material. …….. 70

4.10 Target detection score image from (a) airborne imagery using THI target reference spectrum and the enlarged detection score footprint for (b) N3Y, (c) N4B, (d) N1G, and (e) N2R target. ….. 71

4.11 Target detection performance comparison in space-borne imagery for the THI target reference spectra. ROC curves for the detection from SAM, ACE, CEM, and MF for the (a) N1G, (b) N2R, (c) N3Y, and (d) N4B targets. ROC curves for the subspace-based detector OSP and TCIMF for the N1G, N2R, N3Y, C1W, and N4B targets for (e–h) 5, (i–l) 10, and (m–p) 15 endmember/background materials. …….. 72

4.12 Target detection score image from (a) space-borne imagery using THI target reference spectra and the enlarged detection score footprint for (b) N3Y, (c) N4B, (d) N1G, and (e) N2R target. ……..... 72

4.13 Target detection performance comparison in airborne imagery for the airborne target reference spectra. ROC curves for the detection from SAM, ACE, CEM, and MF for the (a) N1G, (b) N2R, (c) N3Y, (d) C1W, and (e) N4B targets. ROC curves for the subspace-based detector OSP and TCIMF for the N1G, N2R, N3Y, C1W, and N4B targets for (f-j) 5, (k-o) 10, and (p-t) 15 endmember/background materials. …….. 74

4.14 Target detection score image from (a) airborne imagery using airborne target reference spectrum and the enlarged detection score footprint for (b) N3Y, (c) N4B, (d) N1G, (e) N2R, and (f) C1W target. …….. 74

4.15 Target detection performance comparison in space-borne imagery for the airborne target reference spectra. ROC curves for the detection from SAM, ACE, CEM, and MF for the (a) N1G, (b) N2R, (c) N3Y, (d) C1W, and (e) N4B targets. ROC curves for the subspace-based detector OSP and TCIMF for the N1G, N2R, N3Y, C1W, and N4B targets for (f–j) 5, (k–o) 10, and (p–t) 15 endmember/background materials. …….. 76

4.16 Target detection score image from (a) space-borne imagery using airborne target reference spectrum and the enlarged detection score footprint for (b) N3Y, (c) N4B, (d) N1G, (e) N2R, and (f) C1W target. ……. 76

4.17 Target detection performance comparison in space-borne imagery for the airborne target reference spectra. ROC curves for the detection from SAM, ACE, CEM, and MF for the (a) N1G, (b) N2R, (c) N3Y, (d) C1W, and (e) N4B targets. ROC curves for the subspace-based detector OSP and TCIMF for the N1G, N2R, N3Y, C1W, and N4B targets for (f–j) 5, (k–o) 10, and (p–t) 15 endmember/background materials. …….. 77

4.18 Target detection score image from (a) space-borne imagery using space-borne target reference spectrum and the enlarged detection score footprint for (b) N3Y, (c) N4B, (d) N1G, (e) N2R, and (f) C1W target. ……. 78

4.19 Spectral comparison of the reference target spectra with the corresponding image target spectra for: (I) in-situ measurements of (a,f) N1G, (b,g) N2R, (c,h) C1W, (d,i) N3Y, and (e,j) N4B compared to airborne and space-borne image spectra respectively; (II) THI measurements of (a,e) N1G, (b,f) N2R,(c,g) N3Y, and (d,h) N4B compared to airborne and space-borne image spectra respectively; and (III) airborne measurements of (a) N1G, (b) N2R, (c) C1W, (d) N3Y, and (e) N4B compared to space-borne image spectra. ……. 79

4.20 False alarms at different levels of P_D for (I) identical target material (N1G and N2R) in the same context (vegetative) for the (a) best case, and (b) worst-case detection performance; (II) identical target material (N1G and N3Y) in a different context (vegetation and soil respectively) for (c) best case, and (d) worst-case detection performance. ……..... 85

4.21 (a) Visualization of the non-linear interaction of background signal with the target spectrum for the N2R and N1G targets, and (b) best case target detection continuum results of detection performance across imagery from all the platforms (G-ground, A-airborne, S-space-borne) for all the targets used in at a false alarm rate of 10^{-3} for the in-situ target reference spectra. …… 86

4.22 Various elements of a target detection system and their mutual correlation in the detection space. …… 88

5.1 Two different space-time target detection scenarios, with differing atmospheric conditions (Atm_U, Atm_K), leading to a potential mismatch of atmospheric parameters. 94

5.2 6S RT model-based target modelling system design for evaluating spectral target detection performance in multi-platform remote sensing imagery setup. 96

5.3 FM approach for simulation of the N1G target radiance spectra using Equation (5.1) for various AOT values using the in-situ reflectance spectra. 97

5.4 An example target detection result for the N1G target under varying AOT conditions by the MF target detection algorithm.... 99

5.5 Target detection in airborne imagery: variation of P_{FA} due to changes in AOT for target detection in airborne imagery. Illustrated are P_{FA} values when the $P_D = 75\%$ for targets (a) N1G, (b) N2R, (c) C1W, (d) N3Y, and (e) N4B with simulated TOA target radiance spectra at different AOT values between 0 and 5 using point-based target reflectance. 100

5.6 Airborne imagery detection results. Illustrated are PFA values when the $P_D = 75\%$ for targets (a) N1G, (b) N2R, (c) C1W, (d) N3Y, and (e) N4B with simulated TOA target radiance spectra at different AOT values between 0 and 5 using pixel-based THI target reflectance. 101

5.7 Airborne imagery detection results. Illustrated are PFA values when the $P_D = 75\%$ for the N1G target with simulated TOA target radiance spectra at (a-c) AOT = 0.48, (d-f) AOT = 0.89, and (g-i) AOT = 4.94 for different standard aerosol models (i.e., x-axis) at given standard atmospheric models (i.e., coloured line) using point-based target reflectance. 103

5.8 Airborne imagery detection results. Illustrated are PFA values when the $P_D = 75\%$ for the N2R target with simulated TOA target radiance spectra at (a-c) AOT = 0.48, (d-f) AOT = 0.89, and (g-i) AOT = 4.94 for different standard aerosol models (i.e., x-axis) at given standard atmospheric models (i.e., coloured line) using point-based target reflectance. 104

5.9 Airborne imagery detection results. Illustrated are PFA values when the $P_D = 75\%$ for the C1W target with simulated TOA target radiance spectra at (a-c) AOT = 0.48, (d-f) AOT = 0.89, and (g-i) AOT = 4.94 for different standard aerosol models (i.e., x-axis) at given standard atmospheric models (i.e., coloured line) using point-based target reflectance. 105

5.10 Airborne imagery detection results. Illustrated are PFA values when the $P_D = 75\%$ for the N3Y target with simulated TOA target radiance spectra at (a-c) AOT = 0.48, (d-f) AOT = 0.89, and (g-i) AOT = 4.94 for different standard aerosol models (i.e.,

x-axis) at given standard atmospheric models (i.e., coloured line) using point-based target reflectance…….. 106

5.11 Airborne imagery detection results. Illustrated are PFA values when the $P_D = 75\%$ for the N4B target with simulated TOA target radiance spectra at (a-c) AOT = 0.48, (d-f) AOT = 0.89, and (g-i) AOT = 4.94 for different standard aerosol models (i.e., x-axis) at given standard atmospheric models (i.e., coloured line) using point-based target reflectance…….. 107

5.12 Airborne imagery detection results. Illustrated are PFA values when the $P_D = 75\%$ for the N1G target with simulated TOA target radiance spectra at (a-c) AOT = 0.48, (d-f) AOT = 0.89, and (g-i) AOT = 4.94 for different standard aerosol models (i.e., x-axis) at given standard atmospheric models (i.e., coloured line) using pixel-based THI target reflectance. ……. 108

5.13 Airborne imagery detection results. Illustrated are PFA values when the $P_D = 75\%$ for the N4B target with simulated TOA target radiance spectra at (a-c) AOT = 0.48, (d-f) AOT = 0.89, and (g-i) AOT = 4.94 for different standard aerosol models (i.e., x-axis) at given standard atmospheric models (i.e., coloured line) using pixel-based THI target reflectance. ……. 109

5.14 Space-borne imagery detection results. Illustrated are PFA values when the $P_D = 50\%$ for the targets (a) N1G, (b) N2R, (c) C1W, (d) N3Y, and (e) N4B with simulated TOA target radiance spectra at different AOT values between 0 and 5 using the point-based target reflectance. …… 110

5.15 Space-borne imagery detection results. Illustrated are PFA values when the $P_D = 50\%$ for the targets (a) N1G, (b) N2R, (c) N3Y, and (d) N4B with simulated TOA target radiance spectra at different AOT values between 0 and 5 using pixel-based THI target reflectance. …… 111

5.16 Space-borne imagery detection results. Illustrated are PFA values when the $P_D = 50\%$ for the N3Y target with simulated TOA target radiance spectra at (a-c) AOT = 0.48, (d-f) AOT = 0.89, and (g-i) AOT = 4.94 for different standard aerosol models (i.e., x-axis) at given standard atmospheric models (i.e., coloured line) using the point-based target reflectance. …….. 112

5.17 Space-borne imagery detection results. Illustrated are PFA values when the $P_D = 50\%$ for the N4B target with simulated TOA target radiance spectra at (a-c) AOT = 0.48, (d-f) AOT = 0.89, and (g-i) AOT=4.94 for different standard aerosol models (i.e., x-axis) at given standard atmospheric models (i.e., coloured line) using the point-based target reflectance. ……... 113

5.18 Space-borne imagery detection results. Illustrated are PFA values when the $P_D = 50\%$ for the N2R target with simulated TOA target radiance spectra at (a-c) AOT = 0.48, (d-f) AOT =

0.89, and (g-i) AOT = 4.94 for different standard aerosol models (i.e., x-axis) at given standard atmospheric models (i.e., coloured line) using pixel-based THI target spectra. …….. 114

5.19 Space-borne imagery detection results. Illustrated are PFA values when the $P_D = 50\%$ for the N3Y target with simulated TOA target radiance spectra at (a-c) AOT = 0.48, (d-f) AOT = 0.89, and (g-i) AOT = 4.94 for different standard aerosol models (i.e., x-axis) at given standard atmospheric models (i.e., coloured line) using pixel-based THI target spectra. …….. 115

5.20 Spectral similarity score for the point-based in-situ target reference target spectra and the corresponding image spectra for (a, f, k, p) N1G, (b, g, l, q) N2R, (c, h, m, r) C1W, (d, i, n, s) N3Y, and (e, j, o, t) N4B targets at (a-j) AOT = 0.89 for different atmospheric (i.e., coloured lines) and aerosol models (i.e., x-axis where NA= no aerosol, C= Continental, M=Maritime, U=Urban and D= Desert). …… 116

5.21 Spectral similarity score for the point-based in-situ target reference target spectra and the corresponding image spectra for (a, f, k, p) N1G, (b, g, l, q) N2R, (c, h, m, r) C1W, (d, i, n, s) N3Y, and (e, j, o, t) N4B targets at (a-j) AOT = 0.89 for different atmospheric (i.e., coloured lines) and aerosol models (i.e., x-axis where NA= no aerosol, C= Continental, M=Maritime, U=Urban and D= Desert). …… 117

ABBREVIATIONS

6S	Second Simulation of the Satellite Signal in the Solar Spectrum
AC	Atmospheric Correction
ACE	Adaptive Cosine Estimator
ACORN	Atmosphere Correction Now
AOT	Aerosol Optical Thickness
ATCOR	Atmospheric and Topographic Correction
ATREM	Atmosphere Removal Algorithm
CEM	Constrained Energy Minimization
CIBR	Continuum Interpolated Band Ratio
COTS	Commercially Off-The-Shelf
CWV	Columnar Water Vapour
DDV	Dense Dark Vegetation
ELM	Empirical Line Method
EM	Electromagnetic
FA	False Alarms
FACT	Flexible Atmospheric Compensation Technique
FIR	Finite Impulse Response
FLAASH	Fast Line-Of-Sight Atmospheric Analysis of Spectral Hypercubes
FM	Forward Modelling
FMM	Finite Mixture Models
FPGA	Field Programmable Gate Arrays
G-STD	Gudalur-Spectral Target Detection
HATCH	High-Accuracy Atmospheric Correction for Hyperspectral data
IAR	Internal Average Reflectance
IM	Inverse Modelling
LR	Likelihood Ratio
LUT	Look-Up-Table
MF	Matched Filter

MLE	Maximum Likelihood Estimate
MODTRAN	Moderate Resolution Atmospheric Transmission
MVN	Multivariate Normal
OLI	Optical Land Imager
OSP	Orthogonal Subspace Projection
ROC	Receiver Operation Curve
ROI	Region Of Interest
RT	Radiative Transfer
RTM	Radiative Transfer Model
SA	Spectral Angle
SAM	Spectral Angle Mapper
SGA	Spectral Gradient Angle
SHARM	Spherical Harmonics
SID	Spectral Information Divergence
S-MAE	Spatial Mean Absolute Error
SNR	Signal To Noise Ratio
SRF	Sensor Response Function
S-RMSE	Spatial Root Mean Square Error
TCIMF	Target Constrained Interference Minimization Filter
THI	Terrestrial Hyperspectral Imager
TOA	Top-Of-Atmosphere

CHAPTER 1

INTRODUCTION

1.1 Hyperspectral imaging spectroscopy

Technological developments in imaging spectroscopy sensors have led to remote sensing data acquisition with very high spatio-spectral resolution over the last two decades. Present hyperspectral sensors enable continuous sampling of the data at a finer spectral interval (typically 1 $nm\ to$ 5 nm) in the range from 0.4 μm to 2.5 μm of the electromagnetic (EM) spectrum. Coupled with relatively higher spatial resolution, contemporary hyperspectral imagery provides a detailed characterization of the objects' surface reflectance, thereby enabling superior material discrimination (Camps-Valls et al., 2011), as shown in Figure 1.1. Since different materials have unique surface spectral reflectance, hyperspectral imagery provides a wide range of solutions for land surface characterization at various scales (Manolakis, Lockwood, and Cooley 2016). Hyperspectral imagery has been successfully used in applications such as defence (Makki et al., 2017) , mineralogy (Bishop et al., 2011), precision agriculture (Adão et al., 2017; Chen et al., 2019), etc. Although hyperspectral imagery is rich in spectral information, there are some serious challenges in its usage for everyday problems. A series of phenomena such as atmospheric perturbations, time-varying sensor properties, and surface-EM signal interaction cause substantial at-sensor signal distortion, making it challenging to deploy hyperspectral imaging in applications requiring a high degree of accuracy and scalability.

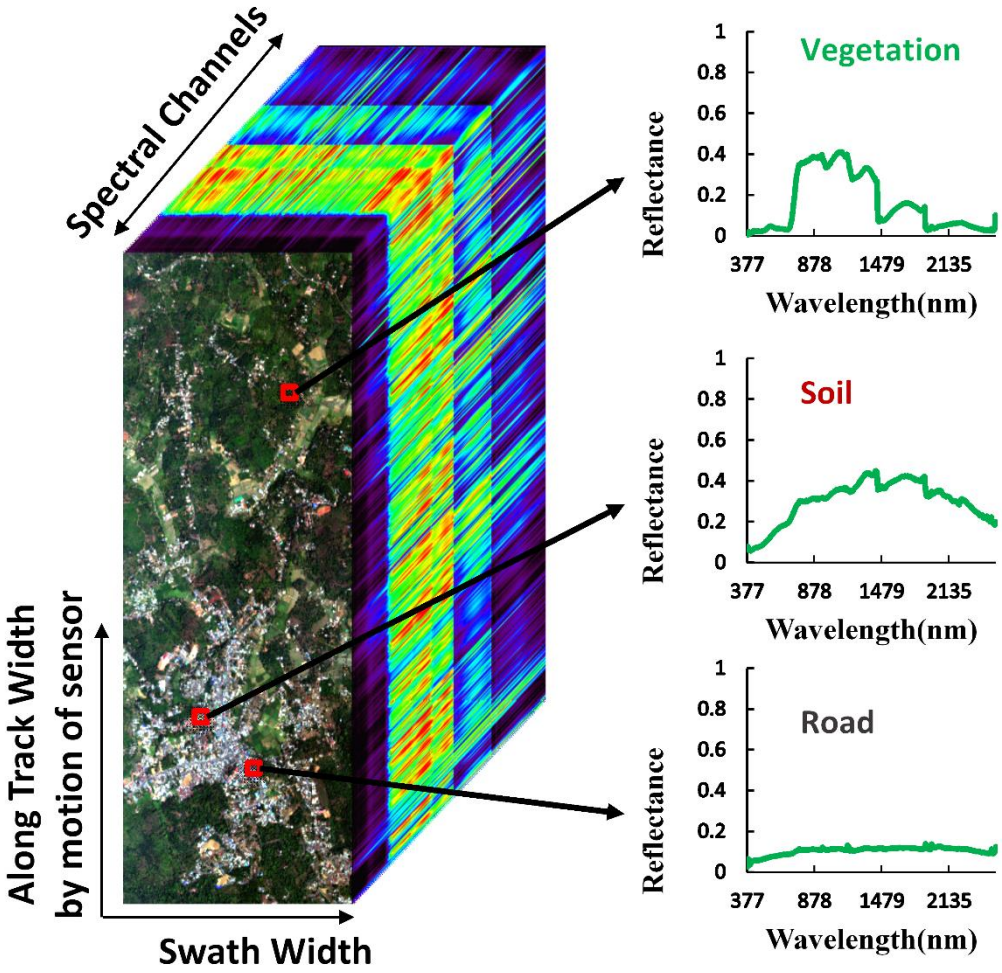

Figure 1.1: Example of hyperspectral imagery with representative vegetation, soil, and road feature spectra

1.2 Atmospheric compensation in target detection

EM signals reaching any remote sensor suffers double attenuation – first from the source of illumination (sun) to the target surface and second from the target surface to the remote sensor due to the atmosphere, as shown in Figure 1.2. Scattering and absorption are the two predominant atmospheric phenomena caused by aerosols, gaseous particles, clouds, and water vapor. Compensating for atmosphere induced distortion in the EM signal is known as atmospheric correction/compensation. The atmospheric correction process converts the sensor reaching spectral radiance of the scene to the surface spectral reflectance. Atmospheric compensation can be typically executed using either an in-scene technique such as empirical line method (ELM) or

physical-based models - also known as radiative transfer models (RTM), such as MODerate resolution atmospheric TRANsmission (MODTRAN), Second Simulation of the Satellite Signal in the Solar Spectrum (6S), etc.

In remote sensing context, when the sensor reaching radiance is converted to surface reflectance using the available RTMs (such as 6S, MODTRAN), the process is termed as inverse modelling/atmospheric correction (IM/AC) mode of data pre-processing (shown in Figure 1.2). The remotely sensed imagery, together with the known acquisition metadata- such as imaging geometry, visibility, atmospheric models, aerosol models, etc.- is fed into the RTM to obtain an atmospherically compensated imagery. It is common to use the AC mode of data pre-processing for numerous remote sensing applications, including target detection. The AC approach for quantifying remote sensing products typically involves intensive computing resources (owing to big remote sensing data). It is time-consuming (pixel by pixel inversion), proving a bottleneck for near real-time applications such as anomaly detection or target detection. An alternative approach, termed forward modelling (FM), uses in-situ reflectance data of the objects at the ground and approximate their at-sensor radiance using the available acquisition parameter (shown in Figure 1.2). This method requires less computational resource as the modelling process is limited to only a few spectra, unlike the pixel to pixel-based inversion process in the AC approach.

1.3 Target detection in hyperspectral imagery

Locating sparsely populated objects of interest in an image is termed target detection in literature (Eismann, 2012). From the perspective of hyperspectral imaging, we exploit the characteristic spectral feature of the target objects in the image to infer their spatial location. Target detection is mathematically formulated as a binary hypothesis testing problem. This approach categorizes every image pixel as either target or background/noise (any pixel other than the target). Typically, the target detectors'

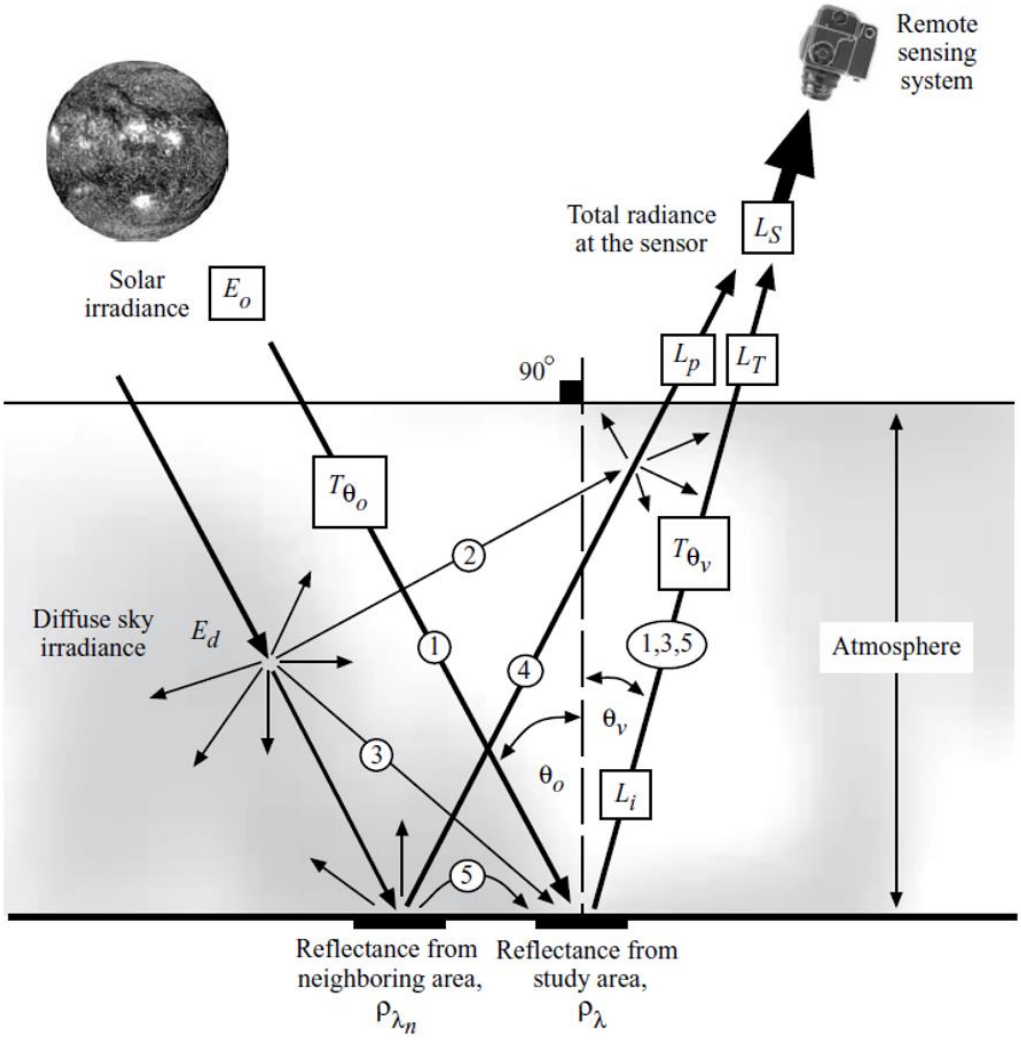

Figure 1.2: Atmospheric processes showing scattering and absorbing components affecting the radiance reaching the remote sensors. (Source: Jensen, J. R. (2009). *Remote sensing of the environment: An earth resource perspective 2/e*. Pearson Education India.)

performance relies on the spectral matching of the in-situ target reference spectrum and the corresponding image spectrum. Since the number of the target pixel in imagery is usually deficient (say 5-10 in 10^6), the pixel level spectral matching is sensitive to several factors such as atmospheric compensation, sensor noise, target-background interactions, and the nature of the target detector algorithm. The pixel occupancy (full or partial) by a target material determines the target detector's suitability for the given problem. Several target detection algorithms have been formulated addressing different aspects of the target /background state. Detectors are typically classified based on the extent of the target present in a pixel (full pixel or sub-pixel) and the assumed statistical

model (probability distribution or linear subspace) for the target and background material(Manolakis, 2005). Target detectors such as likelihood ratio (LR) detectors and matched filters (MF) are commonly used for targets occupying a full pixel. For sub-pixel targets, target detectors like constrained energy minimization (CEM), Target Constrained Interference-Minimized Filter (TCIMF), orthogonal subspace projection (OSP), and adaptive coherence/cosine Estimator (ACE) are preferred (Chang, 2003; Manolakis et al., 2016). We discuss the details of the target detectors used in this thesis in the later chapters.

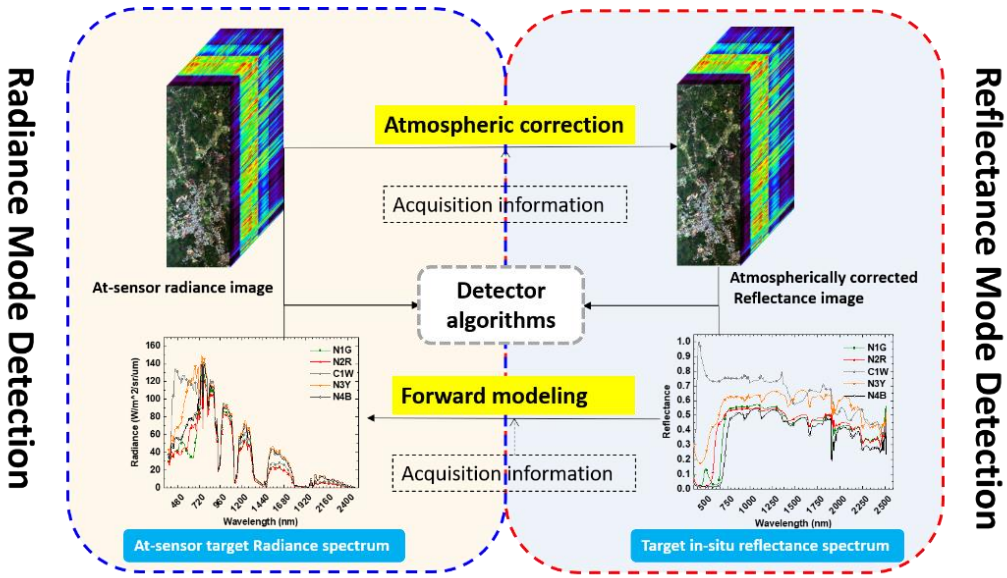

Figure 1.3: Different modes of the spectral target detection

1.4 Motivation and challenges

The growth rate of hyperspectral imaging systems is projected at 14.88% in the period 2020 - 2025 with the present global market valuation of 131.18 million dollars ("Hyperspectral Imaging Market | Growth, Trends, and Forecasts (2020-2025)" n.d.). Evolving imaging platform design coupled with the sensor design sophistications have provided the research community with an opportunity to explore various critical

applications of widely available optical remote sensing data. Platforms such as unmanned aerial vehicles (UAVs) mounted with a portable hyperspectral imager (Table 1.1) facilitate the high-resolution mapping of several features of interest.

Among several generic problems such as classification, anomaly detection, etc., under the umbrella of remote sensing, target detection is challenging due to its multi-faceted nature. Since the distribution of target pixels in the imagery is spatially sporadic and sparse, there is a high degree of uncertainty in its detectability. Besides, spectral target detection is primarily dependent on the quality of the in-situ sample target reference spectra, which is often limited in number. In addition, target detection does not involve a training phase and instead involves only a few (~1-5) sample spectra of the target to be detected in the image. This increases the risk of either failed detection or probability of detection of similar material in the imagery, also called false alarms (FA). Overall, several factors such as atmospheric processes, sensor characteristics, target-background interferences, detection algorithms, etc., may lead to contamination of target signal reaching the sensors and thus determine the target detection performance (Casey & Kerekes, 2009; Cohen et al., 2012a; Archer et al., 2013; Yadav et al., 2018a). With the limitations mentioned above and the dynamism of detection problems, it becomes imperative to investigate it in a holistic perspective comprising key factors deterrent to a successful material detection.

Of late, multispectral remote sensing data have been used for in a limited extent for target detection (Margalit et al., 1985; Wood, 1989; Hoff et al., 1992; Ashton & Schaum, 1998; Landgrebe, 2005). High-resolution multispectral sensors have facilitated detecting generic objects like building, road, vehicle, and ship using template matching, knowledge engineering, object-based, and machine learning methods (Cheng & Han, 2016; Kanjir et al., 2018). Although we find the application of multispectral sensors for detecting generic and large targets such as buildings, specific tree stands, vehicles, etc., its low spectral resolution limits its application to the detection of spatially small and pseudo-engineered targets.

Table 1.1: List of a few portable hyperspectral sensors with their spectral properties and weight

Sensor	Manufacturer	Spectral Range (nm)	Number of spectral bands	Weight (g)
MQ022HG-IM-LS150-VISNIR	XIMEA	470–900	150+	32
MV1-D2048x1088-HS05-96-G2	PhotonFocus	470–900	150	265
Nano HyperSpec	Headwall Photonics Inc.	400–1000	270/775	1200
S 185—FIREFLEYE SE	Cubert GmbH	450–950	125	490
CHAI S-640	Brandywine Photonics	825–2125	260	5000
OCI-UAV-1000	BaySpec	600–1000	100	272
vis-NIR microHSI	NovaSol	400–1000	180	<450
SPECIM FX10	SPECIM	400–1000	224	1260
VNIR-1024	HySpex	400–1000	108	4000
Pika L	Resonon	400–1000	281	600
VIS-VNIR Snapshot	SENOP	400–900	380	720

On the other hand, hyperspectral sensors provide finer spectral bandwidth and offer appropriate baseline spectral data required for typical target detection problems. We find few studies of spectral target detection using hyperspectral data in applications such as detecting military targets (Briottet et al., 2006), surveillance (Yuen & Richardson, 2010), and mineral mapping (Molan et al., 2014; Hou et al., 2016; Dos Reis Salles et al., 2017). The remote sensing-based target detection studies in most of the studies reported assume the target object as a generic class object and is labelled using classical classification algorithms. However, this approach is theoretically not fit for detecting "rare" pixels (targets) in the image and requires a different treatment.

Given a plethora of the state-of-the-art detectors, target detection using spectral data remains far from finding practical applications in real scenarios. One of the key factors causing this limitation is the lack of realistic benchmark datasets. In literature, we find limited datasets available such as C*ooke City*, USA, made available by Rochester Institute of Technology (RIT), NY, USA (Snyder et al., 2008a) for the validation of detection algorithms. While these datasets are useful to the research community, there is a need to formulate several experimental datasets with different scenarios to validate the algorithms rigorously.

In addition to the lack of benchmark datasets, understanding different propagation errors in the pre-processing stage is vital for possible operational deployment of spectral target detection workflows. In particular, atmospheric phenomena cause considerable perturbation in the radiation reaching remote sensing satellite or airborne sensors (Vermote et al., 1997; Agapiou et al., 2011) . Atmospheric correction of remote imagery is sensitive to several parameters such as aerosol models, columnar water vapor (CWV), ozone concentration, aerosol optical thickness (AOT), atmospheric state, etc. The accuracy of remote sensing-based studies is determined by the quality of estimation of these atmospheric parameters (Agapiou et al., 2011; Nia et al., 2015; Marcello et al., 2016; Sabater et al., 2017; Seong et al., 2020). There have been substantial studies on the effect of the atmospheric correction process and related variables on various bio-geophysical parameters (Rahman, 2001; Tirelli et al., 2015; Palve, 2016; Bru et al., 2017). However, a comprehensive study on the effect of atmospheric processes on target detection remains unreported to the best of our knowledge.

Simulations of different atmospheric state variables for assessing their impact on target detection require an open-ended atmospheric correction scheme. MODTRAN has been the predominant RT code for modelling gaseous scattering and absorption in most of the atmospheric correction schemes developed so far. The atmospheric correction based on MODTRAN often lacks a broad range of modeling parameters. As a result, the end-user does not have control over the regional atmospheric parameters such as different aerosol and atmospheric state variables, which may vary substantially from region to region. On the other hand, recent developments (e.g., Bue et al., 2015;

Thompson et al., 2015) indicate the potential of using the 6S RT code as a basis for developing an open-ended atmospheric correction scheme.

Summarizing our review of literature, we found that although spectral target detection is one of the most sought-after research areas across various disciplines, lack of benchmark datasets makes it difficult to test algorithms' scalability in different environments. Besides, spectral target detection by an onboard system requires understanding the dynamic atmospheric parameters, which is least understood. Hence our focus in this thesis is to design a novel benchmark dataset for target detection and develop an atmospheric correction scheme that could help us understand the impact of atmospheric processes on target detection.

1.5 Research objectives

This thesis aims to assess the role of atmospheric state variables and spatial positioning of the target materials on the hyperspectral target detectors' performance and robustness. The development of an open-ended atmospheric correction method with a new benchmark detection dataset would enhance our understanding of spectral target detection processes and intricacies of overall potential factors that impact a target detection framework's performance. The specific objectives of this thesis are as follows:

1. development of a region sensitive atmospheric correction model for hyperspectral and multispectral remote sensors,

2. development of a multi-platform (ground, airborne, and space-borne) target detection benchmark dataset and critical analysis of parameters of detection performance, and

3. simulation and modelling of hyperspectral target detection under varying atmospheric state variables.

1.6 Structure of the Thesis

The thesis has been organized into six chapters such that each chapter covers specific objectives of the proposed research work. The chapters are self-contained and contain key elements - introduction, methods, results, discussion, and conclusions. A brief overview of the contents of the chapters is presented below.

- Chapter 2 presents an overall view of the spectral target detection and theoretical background of RT codes. The chapter introduces the mathematical formulation of target detectors that are used in testing the benchmark dataset proposed.

- Chapter 3 proposes a design framework for the development of an open-end atmospheric correction method. Since most of the available atmospheric correction schemes are commercially off-the-shelf (COTS) and use patented RT codes, we have used open-source RT code for our proposed scheme. The proposed scheme, named as flexible atmospheric compensation technique (FACT) has been evaluated exhaustively using different spatio-spectral statistical error comparing the performance with widely used state-of-the-art atmospheric correction schemes. We have used datasets from hyperspectral and multispectral remote sensors to compare the FACT atmospheric correction model against other atmospheric correction schemes. The FACT atmospheric correction model supports a wide range of hyperspectral and multispectral sensors with an option for the end-user to add-on a customized sensor. Additionally, the FACT supports region specific correction of remote sensing data for various Indian geographical regions and climate zones.

- Chapter 4 describes a new multi-platform hyperspectral and multispectral remote sensing dataset acquired as part of thesis work. We positioned different artificial targets on different surface backgrounds and acquired remote sensing data by terrestrial, airborne, and space-borne remote sensors. We have applied various statistical and subspace detection algorithms on the proposed benchmark dataset to detect targets, considering the different sources of

reference target spectra, background, and the spectral continuity across the platforms. We validated the detection results using the receiver operation curve (ROC) for different cases of detection algorithms and imaging platforms. The detection performance was evaluated as a function of the sensor, platform, target–background, and the source of reference target spectra.

- Chapter 5 explores the forward modelling approach for target detection with different simulations of reference target spectra. We carried out an exhaustive analysis of the target detection performance under different atmospheric models and parameter mismatch in a multi-platform optical dataset. We modelled the atmospheric variables using the 6S RT code and simulated the at-sensor radiance spectra by running multiple 6S RT code runs on the input in-situ target surface reflectance. For this, we considered two cases of target radiance spectra simulation: (1) simulation corresponding to a grid of different AOT values for a predefined atmospheric and aerosol profile, and (2) simulation corresponding to varying combinations of atmospheric and aerosol profiles at a given AOT.

- Finally, in Chapter 6, the salient features of this thesis, conclusions, and lines of future research are presented.

CHAPTER 2

TARGET DETECTION ALGORITHMS: THEORETICAL BACKGROUND

Prelude: In this chapter we present the overview of target detection and discuss related experimental datasets for validations of various detectors. Further, we give the details on the functioning of 6S RT model followed by a description on the mathematical formulation of various target detection algorithms used in the later chapters of this thesis.

2.1 Target detection overview

A generic target detection framework is shown in Figure 2.1. Typically, a priori knowledge on the target's reflectance spectrum is collected using in-situ spectroradiometer and further processed and calibrated for usage in target in the remote sensing imagery. A collection of in-situ surface reflectance of different targets of interest forms the target library. Given the availability of target material library, target detection process begins by conversion of remotely sensed imagery from the raw form to at-sensor radiance using sensor's radiometric parameters. At this juncture, the end-user has the option to either 1) convert the radiance imagery to reflectance imagery using atmospheric correction methods (inverse RT modelling), or 2) convert the target material library to at-sensor radiance spectra using the FM approach as discussed in section 1.2. In the next step, the background statistics (excluding the target) are estimated from the imagery with assumption of model considerations such as multivariate normal (MVN) distribution, background subspace models, finite mixture models (FMM), nonparametric kernel-based models etc., (Matteoli et al., 2014). Based

on the target and background models, the respective detection algorithms (e.g.- ACE for MVN and OSP for background subspace models) are then used to apply on the imagery to detect targets of interest as supplied by the target material library. This step produces a detection score image. Based on thresholding of the score value, whether a pixel belongs to target or is a background pixel is decided.

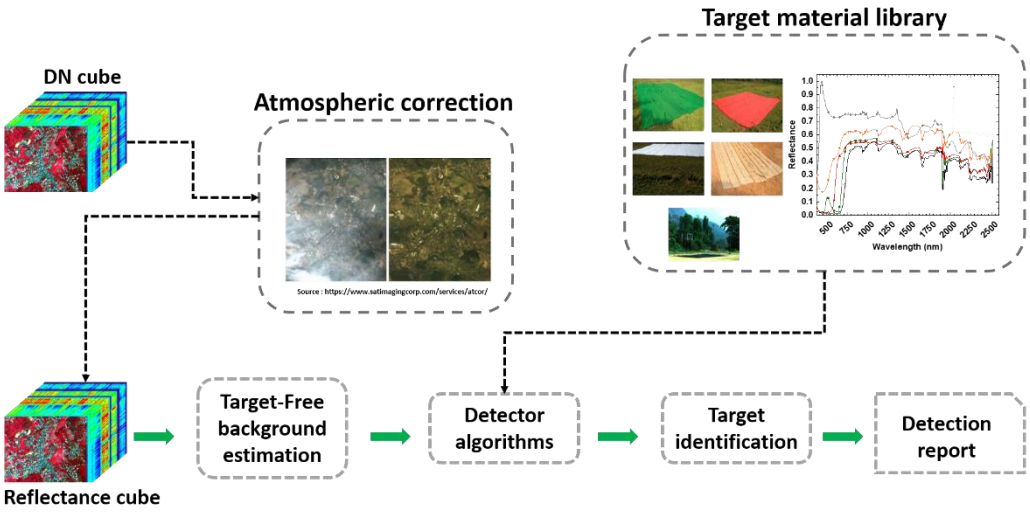

Figure 2.1 : Spectral target detection chain for engineered materials (Adapted from Manolakis, Marden, and Shaw 2003)

Looking at the overall spectral target detection framework, we identify two important factors that are crucial for a successful detection: atmospheric compensation methods and the detection algorithm's response to the target-background dynamics. Healey and Slater (1999) developed a target detection framework for automatic target detection under unknown illumination and atmospheric conditions. Their work used MODTRAN defined standard atmospheric models (such as tropical, midlatitude summer etc), aerosol profiles (rural, urban etc), atmospheric gases (such as O_3, CH_4 etc), and variable imaging geometry to model the target subspace containing 17920 usable target spectra corresponding to each of the combination. Although their work was primarily focussed on utilizing atmospheric conditions to develop an atmospherically invariant target detector, it recognized the spectral variability that is induced into the target subspace due to sensor-atmosphere path. This work was further

extended by Ientilucci and Schott (2005) to develop a hybrid target detector using physical based models to build the target subspace in the radiance space. Other notable works such as Goa et al. (2004), Trym Vegard Haavardsholm, Torbjorn Skauli, and Ingebjorg Kasen (2007), Kolodner, (2008), Matteoli et al. (2009) etc., have used physical based models to devise spectral target detection frameworks accounting for the spectral variability in the target subspace due to atmospheric parameters. Although these studies have reported different approaches for target detection in the radiance space using simulated target subspace, their implementation in real-time systems remains a challenge due to computational requirements (Theiler et al., 2019).

The other factor, target-background dynamics, plays a major role in the efficacy of a target detection algorithm. The target neighbourhood/background in many cases have been found to be one of the key factors deciding its detectability (Wang & Xue, 2017; Yadav et al., 2018a). This aspect of target detection problem requires benchmark multi-platform datasets to evaluate new algorithms so that their reliability can be established. Most of the datasets available are either belong to landcover classification problem (Hook & Rast, 1990; Baumgardner et al., 2015) or are synthetically generated (Duran & Petrou, 2007; Iordache et al., 2011; Dobigeon et al., 2014). Within the context of target detection, the classic approach of implanting targets synthetically in an existing dataset has also been attempted (Zhang et al., 2014; Yani Hou et al., 2019). Moreover, most of the target detection studies (Cohen et al., 2012; Du & Zhang, 2014; Wang & Xue, 2017) have used the same sensor data, available in public domain, (Snyder et al., 2008a; Acito et al., 2016;) with small spatial extent, which limit rigorous testing of target detection in various environments and at different spatial scales.

2.2 Radiative transfer theory

Since the electromagnetic radiations in the optical region undergo perturbation caused by atmospheric components such as aerosols, water particles, clouds, dust, etc., various physical-based radiative transfer models approximate different parameters to compensate for the net atmospheric effects. These models generally make assumptions for the at-sensor reaching radiation as sum of multiple components. A shown in Figure

1.2, the total radiance at the sensor can be written as sum of radiant energy reflected into the view of sensor from different paths (Jensen, 2009) as following: (1) spectral solar irradiance reaching the target surface as a function of atmospheric transmittance and reflected back to sensor, (2) the amount of scattered radiant energy reflected towards sensor due to the atmospheric gases and aerosol, (3) radiation received by target surface after scattering and reflected back towards sensor, (4) radiation received by the sensor from the neighbouring pixel, and (5) amount of radiation reflected from neighbouring pixel on to the target surface and then reflected back to the sensor. Ignoring path (4) and (5) for simplicity, which are often called adjacency effect, the total normalized top-of-atmosphere (TOA) reflectance ρ^*_{toa} due to TOA radiance L_{TOA} is given as (Thompson et al., 2019):

$$\rho^*_{toa}(\theta_s, \theta_v, \varphi) = \frac{\pi\, L_{TOA}}{\mu_s E_s}$$

$$= T_g(\theta_s, \theta_v)\left[\begin{array}{c} \rho_a(\theta_s, \theta_v, \varphi) \\ + e^{\frac{-\tau}{\mu_s}}\, e^{\frac{-\tau}{\mu_v}}\, \rho_{ac(\theta_s, \theta_v, \varphi)} \\ + e^{\frac{-\tau}{\mu_v}}\, t_d(\theta_s)\rho_{hd} + e^{\frac{-\tau}{\mu_s}}\, t_d(\theta_v)\rho_{dh} \\ + t_d(\theta_s)t_d(\theta_v)\rho_{hh} \\ + \dfrac{\left[e^{\frac{-\tau}{\mu_s}} + t_d(\theta_s)\right]\left[e^{\frac{-\tau}{\mu_v}} + t_d(\theta_v)\right] S_c(\rho_{hh})^2}{1 - S_a\rho_{hh}} \end{array}\right], \quad (2.1)$$

where, μ_s is the cosine of the solar zenith angle, $\mu_v$is the cosine of view zenith angle, E_s is the top-of-atmosphere solar flux, θ_s, θ_v and φ_s, φ_v are the geometrical parameters (zenith and azimuth angles for solar and view positions of sun and sensor respectively), φ is the relative azimuth angle, ρ_a is the intrinsic atmospheric reflectance also known as path reflectance, T_g is the gaseous transmittance, $e^{-\tau/\mu_s}$ and $t_d(\theta_s)$is the downward direct and diffuse transmittance from the sun to the ground, $e^{-\tau/\mu_v}$ and $t_d(\theta_v)$ is the transmittance from the ground to the sensor, S_a is the spherical albedo and ρ_{ac} is the expected atmospherically corrected reflectance (also known as surface reflectance). The terms $\rho_{hd}, \rho_{dh}, \rho_{hh}$ refer to hemispherical-directional, directional-hemispherical, and hemispherical-hemispherical reflectance of the target surface respectively. For the

case of assumed Lambertian surface it is found that $\rho_{hd} = \rho_{dh} = \rho_{hh} = \rho_{ac}$. Thus equation 2.1 simplifies to:

$$\rho^*_{toa}(\theta_s, \theta_v, \varphi_s, \varphi_v) = T_g(\theta_s, \theta_v)\left[\rho_a + T(\theta_s)T(\theta_v)\frac{\rho_{ac}}{1 - S_a \times \rho_{ac}}\right], \qquad (2.2)$$

where $T(\theta_s)$, and $T(\theta_v)$ represent the total transmittance from the sun to the ground, $T(\theta_v)$ and from the ground to the sensor respectively.

Simplifying equation (2.1) and (2.2), ρ_{ac} reduces to:

$$\rho_{ac} = \frac{y}{1 + x_c \times y}, \qquad (2.3)$$

where,

$$\begin{aligned} y &= x_a \times L_{TOA} - x_b; \\ x_a &= \frac{\pi}{T_g T(\theta_s) T(\theta_v) \mu_s E_s}\ ; \\ x_b &= \frac{\rho_a}{T(\theta_s)T(\theta_v)}\ ; \\ x_c &= s. \end{aligned} \qquad (2.4)$$

The 6S RT code yields correction coefficients $x_a, x_b,$ and x_c at the end of running the code and we store them in a look-up table for various combinations of input parameters. When atmospheric correction of an imagery is required, equation (2.3) is inverted to obtain atmospherically corrected reflectance according to equation (2.4).

2.3 Target detection methods

The taxonomy of detection algorithms depends on various factors such as target-pixel occupancy (full pixel vs sub-pixel target), considerations for spectral variability (either

for target or background), and modelling the combination of pixel and sub-pixel targets (Manolakis et al., 2016). Given an image $\chi_{(m,n)}$ having k spectral channels and m x n pixels such that each pixel $\mathbf{x}_i = \{x_1, x_2, x_3, x_4 \ldots x_k\}^t \in \mathbf{X}_{k,mn}$, target detection is formulated as a hypothesis testing problem. Mathematically, target detection can be expressed as a binary hypothesis testing problem:

$$\mathrm{H}_0 (\text{ Null Hypothesis}) \ \mathbf{x}_i : \text{ noise (Target absent)},$$

$$\mathrm{H}_1 (\text{Alternate Hypothesis}) \ \mathbf{x}_i : \text{ Target}.$$

Assuming a multivariate normal distribution for target and background, the target detection is represented as a hypothesis testing:

$$\begin{aligned} \mathrm{H}_0 &: \mathbf{x} = \mathbf{n} \\ \mathrm{H}_1 &: \mathbf{x} = \mathbf{s} + \mathbf{n}, \end{aligned} \tag{2.5}$$

where $\mathbf{s}$ is the known target spectrum and $\mathbf{n}$ is the noise/background with mean vector $'\mathbf{m}'$ and covariance matrix $\mathbf{C}$ such that $\mathbf{n} \sim N(\mathbf{m}, \mathbf{C})$. Since the target and background are assumed to follow a multivariate normal distribution, the probability density function $p(\mathbf{x}, \theta)$ for a k-dimensional Gaussian vector $\mathbf{x}$ is given by:

$$p(\mathbf{x}, \theta) = \frac{1}{(2\pi)^{\mathrm{k}/2} |\mathbf{C}|^{1/2}} \exp\left\{-\frac{1}{2}[\mathbf{x} - \mathbf{m}]^T \mathbf{C}^{-1} [\mathbf{x} - \mathbf{m}]\right\}. \tag{2.6}$$

At a given false alarm rate (Neyman-Pearson criterion), the probability of detection is maximized by using a likelihood ratio (LR) type of detectors (Kay, 1993) expressed as:

$$l(\mathbf{x}) = \frac{\mathrm{p}(\mathbf{x}|\mathrm{H}_1)}{\mathrm{p}(\mathbf{x}|\mathrm{H}_0)} \underset{\mathbf{H_0}}{\overset{\mathbf{H_1}}{\gtrless}} \eta, \tag{2.7}$$

where η is the threshold. If $l(\mathbf{x})$ is greater than η, then alternate hypothesis (target-present) is declared true. Equation (2.5) describes the basic statistical model in case of a full pixel under the ideal assumption of the same covariance estimate for both target

and background. However, at times target pixel gets mixed up due to the targets being spatially unresolved. In such cases the appropriate statistical model (also known as replacement model) is:

$$\begin{aligned} \mathrm{H}_0 &: \mathbf{x} = \mathbf{n} \\ \mathrm{H}_1 &: \mathbf{x} = \alpha\mathbf{s} + \beta\mathbf{n}\,, \end{aligned} \tag{2.8}$$

where $\mathbf{x} \sim N(\mathbf{0}, \mathbf{C})$ under H_0 and $\mathbf{x} \sim N(\alpha\mathbf{s}, \beta^2\mathbf{C})$; α refers to the fraction fill of the target or abundances if **s** represents a matrix containing endmembers.

In this thesis we have used both the types of detection algorithms (full pixel and sub-pixel) for detecting targets in the proposed experimental benchmark dataset. Several detection algorithms such as spectral angle mapper (SAM) (Kruse et al., 1993a), MF (D. Manolakis, 2003), CEM (Chang, 2003), ACE (Scharf & McWhorter, 1996), OSP (Harsanyi & Chang, 1994), and TCIMF (Ren & Chang, 2000) implemented for detection of targets in this work are briefly described in the following sub-sections.

2.3.1 Spectral Angle Mapper (SAM)

Modifying the signal model given by equation (2.5), we have the hypothesis testing:

$$\begin{aligned} \mathrm{H}_0 &: \mathbf{x} = \mathbf{n} \\ \mathrm{H}_1 &: \mathbf{x} = \alpha\mathbf{s} + \mathbf{n}\,, \end{aligned} \tag{2.9}$$

where α represents the strength of the target signal in the acquired imagery, $\mathbf{n} \sim N(0, \sigma^2\mathbf{I})$ with σ^2 being variance. We estimate α using the maximum likelihood estimate (MLE) under the modified signal model as:

$$\frac{\partial \mathrm{p}(\mathrm{x}|\mathrm{H}_1)}{\partial \alpha} = \frac{\partial}{\partial \alpha}\left\{\exp\left(\frac{-1}{2}(\mathrm{x} - \alpha\mathbf{s})^{\mathrm{T}}\,(\mathrm{x} - \alpha\mathbf{s})\right)\right\}. \tag{2.10}$$

Equating equation (2.10) to zero, we obtain the MLE estimate of α as follows:

$$\hat{\alpha} = \frac{\mathbf{s}^{\mathrm{T}}\mathbf{x}}{\mathbf{s}^{\mathrm{T}}\mathbf{s}}. \tag{2.11}$$

It is usual to estimate the variance (σ^2) from the image pixel, i.e. pixel under test given by $\hat{\sigma}^2 = \mathbf{x}^{\mathrm{T}}\mathbf{x}$. Substituting the estimated parameters in equation (2.7) and taking the log-likelihood of the distribution functions, the test statistic is given by:

$$r(\mathrm{x}) = \ln\left(\frac{\mathrm{p}(\mathrm{x}|\mathrm{H}_1)}{\mathrm{p}(\mathrm{x}|\mathrm{H}_0)}\right) = \frac{(\mathbf{s}^{\mathrm{T}}\mathrm{x})^{\mathbf{2}}}{(\mathbf{s}^{\mathrm{T}}\mathbf{s})(\mathbf{x}^{\mathrm{T}}\mathbf{x})}. \tag{2.12}$$

We reframed the equation (2.9) to represent the test statistic known as spectral angle mapper (SAM) as:

$$r_{SAM}(\mathbf{x}) = cos^{-1}\left[\frac{\mathbf{s}^{T}\mathbf{x}}{\sqrt{(\mathbf{s}^{T}\mathbf{s})(\mathbf{x}^{T}\mathbf{x})}}\right]. \tag{2.13}$$

Geometrically, SAM measures the similarity between two n-dimensional vectors based on the cosine of the angle between two vectors.

2.3.2 Matched Filter (MF)

The MF allows background representation with a normal distribution with finite mean and covariance. The signal model then becomes:

$$\begin{aligned} \mathrm{H}_0 &: \mathbf{x} = \mathbf{n} \\ \mathrm{H}_1 &: \mathbf{x} = \alpha\mathbf{s} + \mathbf{n}, \end{aligned} \tag{2.14}$$

where $\mathbf{n} \sim N(\mathbf{m}, \mathbf{C})$, and α are the unknown parameters. For the given model, we have:

$$p(\mathbf{x}|\mathrm{H}_0) = \frac{1}{(2\pi)^{\mathrm{k}/2}|\hat{\mathbf{C}}|^{1/2}} \exp\left\{-\frac{1}{2}[\mathbf{x} - \hat{\mathbf{m}}]^{T}\hat{\mathbf{C}}^{-1}[\mathbf{x} - \hat{\mathbf{m}}]\right\} \tag{2.15}$$

$$p(\mathbf{x}|\mathrm{H}_1) = \frac{1}{(2\pi)^{\mathrm{k}/2}|\hat{\mathbf{C}}|^{1/2}} \exp\left\{-\frac{1}{2}[\mathbf{x} - \hat{\alpha}\mathbf{s} - \mathbf{m}]^T \hat{\mathbf{C}}^{-1}[\mathbf{x} - \hat{\alpha}\mathbf{s} - \hat{\mathbf{m}}]\right\} \quad (2.16)$$

Applying the MLE technique similar to equation (2.10) we get:

$$\hat{\alpha} = \frac{\mathbf{s}^T\hat{\mathbf{C}}^{-1}(\mathbf{x} - \hat{\mathbf{m}})}{\mathbf{s}^T\hat{\mathbf{C}}^{-1}\mathbf{s}}, \hat{\mathbf{m}} = \frac{1}{\mathrm{N}}\sum_{i=1}^{\mathrm{N}} \mathbf{x}_i \ , \hat{\mathbf{C}} = \frac{1}{\mathrm{N}}\sum_{i=1}^{\mathrm{N}} [\mathbf{x}_i - \hat{\mathbf{m}}][\mathbf{x}_i - \hat{\mathbf{m}}]^{\mathrm{T}} \ . \quad (2.17)$$

Since the detector assumes an additive model, for $\alpha = 1$ under the null hypothesis, we have $\mathbf{x} = \mathbf{s} + \mathbf{m}$, which is incorrect. Besides, α, by definition, is not constrained to be positive and may cause negative test statistic (Eismann et al., 2009). Correcting for these two problems and using the estimates from equation (2.17), we can express MF score r as:

$$r_{MF}(\mathbf{x}) = \frac{(\mathbf{s} - \hat{\mathbf{m}})^T\hat{\mathbf{C}}^{-1}(\mathbf{x} - \hat{\mathbf{m}})}{\sqrt{(\mathbf{s} - \hat{\mathbf{m}})^T\hat{\mathbf{C}}^{-1}(\mathbf{s} - \hat{\mathbf{m}})}}. \quad (2.18)$$

2.3.3 Adaptive Cosine Estimator (ACE)

Modifying the equation (2.8) to include a scale factor β yields the following replacement model:

$$\begin{aligned} \mathrm{H}_0 &: \mathbf{x} = \beta\mathbf{n} \\ \mathrm{H}_1 &: \mathbf{x} = \ \mathbf{x} = \ \alpha\mathbf{s} + \beta\mathbf{n} \ , \end{aligned} \quad (2.19)$$

where $n \sim N(0, \mathbf{C})$ and α, β are the unknown parameters. The above model is similar to Kelly's detector (Kelly, 1986), except for the introduction of an unknown parameter β in the null hypothesis. The ACE detector was derived based on the assumption of different covariance estimates ($\hat{\mathbf{C}}_0, \hat{\mathbf{C}}_1$) under the null and alternate hypotheses. It is assumed that the data under the null hypothesis correspond to training data for noise/background estimation and pixel under test (under the alternative hypothesis) is the testing data. Maximizing the joint probability density function of the training and test data yields the following estimates:

$$\hat{\alpha} = \frac{\mathbf{s}^T \hat{\mathbf{C}}^{-1}\mathbf{x}}{\mathbf{s}^T \hat{\mathbf{C}}^{-1}\mathbf{s}},$$

$$\hat{\beta}_0^2 = \frac{\mathrm{N}-\mathrm{k}+1}{\mathrm{Nk}}\mathbf{x}^{\mathrm{T}}\hat{\mathbf{C}}^{-1}\mathbf{x},$$

$$\hat{\beta}_1^2 = \frac{\mathrm{N}-\mathrm{k}+1}{\mathrm{Nk}}(\mathbf{x}-\hat{\alpha}\mathbf{s})^{\mathrm{T}}\hat{\mathbf{C}}^{-1}(\mathbf{x}-\hat{\alpha}\mathbf{s}),$$

and

$$\hat{\mathbf{C}}_0 = \frac{1}{\mathrm{N}+1}\left[\frac{1}{\beta_0^2}\mathbf{x}\mathbf{x}^{\mathrm{T}} + \mathrm{N}\hat{\mathbf{C}}\right],$$

$$\hat{\mathbf{C}}_1 = \frac{1}{\mathrm{N}+1}\left[\frac{1}{\beta_1^2}(\mathbf{x}-\alpha\mathbf{s})(\mathbf{x}-\alpha\mathbf{s})^{\mathrm{T}} + \mathrm{N}\hat{\mathbf{C}}\right], \tag{2.20}$$

where $\hat{\beta}_0$, $\hat{\mathbf{C}}_0$,$\hat{\beta}_1$,$\hat{\mathbf{C}}_1$ are the estimates under the null and alternate hypothesis, respectively. Plugging the derived estimates in the general form of log-likelihood ratio test detector (equation 2.7), we get the ACE score r as:

$$r_{\mathrm{ACE}}(\mathbf{x}) = \frac{\left(\mathbf{s}^{\mathrm{T}}\hat{\mathbf{C}}^{-1}\mathbf{x}\right)^2}{(\mathbf{s}^{\mathrm{T}}\hat{\mathbf{C}}^{-1}\mathbf{s})(\mathbf{x}^{\mathrm{T}}\hat{\mathbf{C}}^{-1}\mathbf{x})}. \tag{2.21}$$

2.3.4 Constrained Energy Minimization (CEM)

The aforementioned spectral detectors assume the target and background subspace to follow a particular statistical distribution. Based on the assumed distribution function, we usually derive the parameters of the distribution function. The assumption of background conformity to a statistical distribution may lead to ambiguous results if the target or background is different from the assumed statistical function. In such situations, it is desirable to design a detector that does depend upon the target-background distribution function and eliminates the interferer from the target signal.

The CEM is one such detector and is functionally equivalent to a finite impulse response (FIR) filter that minimizes the detector output for the background pixels.

Given an image $\chi_{(m,n)}$ with k spectral channel and N pixels such that each pixel $\mathbf{x}_i = \{x_1, x_2, x_3, x_4 \dots x_{\mathrm{k}}\}^t \in \mathbf{X}_{\mathrm{k}\times\mathrm{N}}$, the average energy of the FIR filter output can be written as:

$$\frac{1}{(\mathrm{N})}\left\{\sum_{i=1}^{\mathrm{N}} \phi_i{}^2\right\} = \frac{1}{(\mathrm{N})}\left\{\sum_{i=1}^{\mathrm{N}} (\mathbf{x}_i{}^T\mathbf{W})^T(\mathbf{x}_i{}^T\mathbf{W})\right\},$$

$$= \mathbf{W}^T\left\{\frac{1}{\mathrm{N}}\sum_{i=1}^{\mathrm{N}} \mathbf{x}_i\mathbf{x}_i{}^T\right\}\mathbf{W} = \mathbf{W}^T\mathbf{R}\mathbf{W}, \tag{2.22}$$

where $\phi = (\mathbf{x}_i{}^T\mathbf{W})$ is the filter output for the pixel vector $\mathbf{x}_i$, $\mathbf{W} = (w_1, w_2, w_3, w_4 \dots w_k)^T$ is the weight vector for the designed filter, and $\mathbf{R}$ is the k-dimensional background correlation matrix. The CEM problem statement then becomes a constraint optimization problem, i.e. $\min_{\mathbf{w}}(\mathbf{W}^T\mathbf{R}_{\mathrm{k}\times\mathrm{k}}\mathbf{W})$ subject to $\mathbf{s}^{\mathrm{T}}\mathbf{W} = 1$. The detection problem is solved using the Lagrange's multiplier method to solve the constrained optimization problem to get the CEM score r as:

$$r_{CEM}(\mathbf{x}) = \frac{(\mathbf{s}^{\mathrm{T}}\mathbf{R}^{-1}\mathbf{s})}{(\mathbf{R}^{-1}\mathbf{s})^{\mathrm{T}}\mathbf{x}}. \tag{2.23}$$

2.3.5 Orthogonal subspace projection (OSP)

In most of the practical hyperspectral target detection problems, the target size is less than a full pixel. In such cases, spectral mixture models are useful to estimate the material abundances. The OSP assumes a linear mixture model expressed as:

$$\mathbf{x} = \mathbf{M}\boldsymbol{\alpha} + \mathbf{n}, \tag{2.24}$$

where $\mathbf{M}$ is a matrix of target / known spectral signatures, $\boldsymbol{\alpha}$ is abundance, and $\mathbf{n}$ is the noise. The OSP begins by first separating the desired target and unknown target and

then projecting desired targets orthogonally to undesired / interferer target space. Mathematically OSP is given by:

$$r_{OSP} = \mathbf{d}^{\mathrm{T}} \boldsymbol{P}_{\mathrm{U}}^{\perp} \mathbf{x}\,. \tag{2.25}$$

where $\mathbf{d}$ is the desired target, $\boldsymbol{P}_{\mathrm{U}}^{\perp}$is the projection operator which projects the image pixel to space orthogonal to $\mathbf{U}$ (undesired targets/interferer) given as $\boldsymbol{P}_{\mathrm{U}}^{\perp} = \mathbf{I}_{\mathrm{k}\times\mathrm{k}} - \mathbf{U}\mathbf{U}^{\#}$, $\mathbf{U}^{\#}$ is the pseudo inverse of $\mathbf{U}$and given as $(\mathbf{U}^{\mathrm{T}}\mathbf{U})^{-1}\mathbf{U}^{\mathrm{T}}$, and $\mathbf{I}_{\mathrm{k}\times\mathrm{k}}$ is the identity matrix.

2.3.6 Target constrained interference minimization filter (TCIMF)

In this approach, the image is assumed to be a combination of three signal components, i.e. desired (targets), undesired (unwanted/background), and interferer component. Like the CEM, the desired component is accentuated while suppressing the interference signal. The TCIMF is a theoretical superset of CEM and capable of detecting multiple targets at once, unlike CEM and OSP. Mathematically, TCIMF score is given as:

$$r_{\mathrm{TCIMF}}(\mathbf{x}) = \left\{ \frac{\mathbf{R}_{\mathrm{k}\times\mathrm{k}}^{-1}[\mathbf{DU}]}{([\mathbf{DU}]^{\mathrm{T}}\,\mathbf{R}_{\mathrm{k}\times\mathrm{k}}^{-1}[\mathbf{DU}])} \begin{bmatrix} \mathbf{1}_{\mathrm{p}\times 1} \\ \mathbf{0}_{\mathrm{q}\times 1} \end{bmatrix} \right\}^{\boldsymbol{T}} \mathbf{x}\,, \tag{2.26}$$

where $\mathbf{D} = [\mathbf{d_1}, \mathbf{d_2}, \ldots\ldots\ldots \mathbf{d_p}]$ is the set of desired/known target signals, $\mathbf{U} = [\mathbf{u_1}, \mathbf{u_2}, \ldots\ldots\ldots\ldots \mathbf{u_q}]$ is the known background/unwanted signals in the image.

2.4 Atmospheric parameters and target detection

The 6S RT code incorporates various standard atmospheric models defined by approximation of climatic conditions, such as Tropical, Midlatitude Summer, etc. The atmospheric profiles have predefined columnar profiles (0-100kms) of different variables such as atmospheric pressure (units), temperature, water vapour, and ozone concentrations as a function of height. Further, based on aerosol properties such as AOT, mean radius of aerosol particle, real/imaginary refractive indices, particle

distribution function, and angstrom coefficient, several standard aerosol models (continental, urban, maritime, desert, etc.) are defined in 6S model. Taking into account for these variables explicitly as function of wavelength λ, equation (2.2) can be modified as:

$$\begin{aligned}&\rho_{toa}^{\lambda}\left(\theta_s,\theta_v,\varphi_s,\varphi_v,P,\psi^{\lambda},U_{H_2O},U_{O_3}\right)\\&=T_{g_{OG}}^{\lambda}(m,P)T_{g_{O_3}}^{\lambda}\left(m,U_{O_3}\right)\Bigg[\rho_a^{\lambda}\left(\theta_s,\theta_v,\varphi_s,\varphi_v,P,\psi^{\lambda},U_{H_2O}\right)\\&+T_{r_a}^{\lambda}\left(\theta_s,\theta_v,\varphi_s,\varphi_v,P,\psi^{\lambda}\right)\frac{\rho_{ac}}{1-S_a^{\lambda}(P,\psi^{\lambda})\rho_{ac}}T_{g_{H_2O}}^{\lambda}\left(m,U_{H_2O}\right)\Bigg],\end{aligned}\tag{2.27}$$

where P is the atmospheric pressure (mb), U_{H_2O} is the integrated atmospheric water vapour (cm), U_{O_3} is the integrated columnar ozone concentration (cm-atm), m is the air-mass given as $\frac{1}{\cos\theta_s}+\frac{1}{\cos\theta_v}$, T_g represent the gaseous transmittance with the subscripts OG, H_2O, O_3 denoting gaseous transmittance by gases like CO_2, O_2, CH_4, water vapour (H_2O) and ozone (O_3) respectively, and ψ^{λ} represent the aerosol components described as:

$$\psi^{\lambda}=(\tau_a,\omega_0,\mathrm{P}_a),\tag{2.28}$$

where τ_a is the AOT, ω_0 is single scattering albedo and P_a is the phase function at a given wavelength λ.

Inverting equation (2.3) we have:

$$L_{TOA}=\frac{\rho_{toa}^{*}\times\mu_s E_s}{\pi},\tag{2.29}$$

where $\rho_{toa}^{*}=\rho_{toa}^{\lambda}$ and is given by equation (2.2). Since the values of ρ_{ac} for the targets are known a-priori from the in-situ measurements, we can simulate different L_{TOA} reaching the sensor owing to different atmospheric variables using equation (2.29).

2.5 Chapter Conclusions

Target detection is one of the key applications of hyperspectral remote sensing and the performance of detectors is typically determined by several factors. This chapter presented an overview of the target detection framework, detection algorithms and the key factors determining the detectability of engineered targets. Further, the important link between spectral target detection and atmospheric processes is also established. Finally, a brief mathematical description of all the target detection algorithms and RT model used are also presented.

CHAPTER 3

REGION SENSITIVE ATMOSPHERIC CORRECTION MODEL

Prelude: In this chapter, the development and evaluation of an open-end atmospheric correction scheme, named Flexible Atmospheric Compensation Technique (FACT), is described. The developed method is validated against standard atmospheric correction schemes using various hyperspectral and multispectral imagery. The methods and outcomes of this chapter are used further in the thesis to understand the role of atmospheric processes in determining the spectral target detection performance[1].

3.1 Introduction

Atmospheric phenomena, such as absorption by gaseous particles and scattering by aerosol particles, cause considerable perturbation in the radiation reaching remote sensing satellite or airborne sensors (Vermote et al., 1997). Models which account for this path induced effects in remote sensing data are known as radiative transfer (RT) models (Liang, 2005). Numerous applications of multispectral and hyperspectral remote sensing data such as estimation of biophysical parameters (Rao et al., 2008; Wu et al., 2015), leaf area index (Rao et al., 2006; Liu et al., 2016), water depth estimation (Jay and Guillaume 2014), coastal water quality (Brando & Dekker, 2003; Gholizadeh et al., 2016) land use and cover change (Joshi et al., 2016), soil organic carbon (Minu et al., 2017), etc., rely on accurate surface reflectance data.

---

[1]The major contents of this chapter are published in *Geocarto International* Vol: 36(1), 2019 Publisher: Taylor & Francis. Authors: Sudhanshu Shekhar Jha, Manohar Kumar C.V.S.S, Rama Rao Nidamanuri.

In most of these applications, quality of results depends mainly on the quality of atmospheric correction of the remote sensing data.

Atmospheric correction is generally divided into two categories: in-scene based, and physical based models (Gao et al., 2006). Physical based models use a RT code which requires information on a number of parameters describing atmospheric conditions, aerosol constituents, pressure, temperature, and CWV distribution, to be supplied by the user. Whereas, in-scene methods are less complex and no such a priori information is required to perform atmospheric correction (Eismann, 2012). Gao et al. (2009) have reviewed the performance of several physical based models such as Atmosphere Removal algorithm (ATREM), Second Simulation of the Satellite Signal in the Solar Spectrum (6S), the Fast Line-of-sight Atmospheric Analysis of Spectral Hypercubes (FLAASH), High-accuracy Atmospheric Correction for Hyperspectral Data (HATCH), Atmosphere CORrection Now (ACORN), MODerate resolution atmospheric TRANsmission (MODTRAN), Atmospheric and Topographic Correction (ATCOR) and in-scene methods such as Empirical Line Method (Conel et al., 1987), the Internal Average Reflectance (IAR) (Kruse, 1988), Flat Field Correction (Roberts et al., 1986) etc. Working behind, MODTRAN is the choice of RT code in operational implementations of atmospheric correction modules. As continuation of the open-source research initiatives such as 3S, 4S and 5S, the 6S is a generic RT code found to be a competitive alternative to the existing atmospheric correction models (Vermote et al. 2006). It has been adapted and improved by MODIS Land Surface Reflectance Science Computing Facility and is freely available (http://6s.ltdri.org/). Kotchenova et al., (2008) have discussed the performance of four prominent RT codes i.e., MODTRAN, 6S, SHARM (spherical harmonics), and an improved version of basic radiative transfer called RT3 and compared performance for different atmospheric conditions and viewing geometry. They observe that 6S is within 1% accuracy compared to the Monte Carlo code. However, their evaluation of 6S based RT code contained only a few broadband wavelengths typical to low spectral resolution multispectral sensors. The performance of the 6S across the optical spectrum including water and gaseous absorption regions at a finer spectral resolution, typical to contemporary and future extended range of multispectral (e.g., WorldView-3) and hyperspectral sensors, is not yet reported.

Remote sensor specific atmospheric correction schemes based on some selected features of 6S RT code have been developed for several multispectral sensors. Example, Pandya et al. (2015) developed a model called SACRS2 for the atmospheric correction of Resourcesat-2 AWiFS data. They have used the forward model computations of 6S for obtaining the scattering and transmittance coefficients required for using in another atmospheric correction method known as SMAC. Hu et al. (2014) developed an atmospheric correction scheme for correcting LANDSAT-5 data using information on atmospheric parameters acquired from MODIS data. Wang developed a similar atmospheric correction scheme for the LANDSAT-8 sensor.

For most of the atmospheric correction schemes that have been developed so far, developers have preferred MODTRAN as the RT code for calculating scattering and transmittance coefficients due to gaseous particles. Though MODTRAN is a sophisticated RT code, the atmospheric correction schemes based on it often lack support for fine tuning of modelling parameters. This leaves the end user with no choice of selecting regional parameters that may vary from the standard global set of observations, thus, impairing the study of local atmospheric phenomena. On the other hand, recent works indicate the 6S RT code's potential for development of open-ended atmospheric correction scheme. Together with these research gaps and recent progress in using 6S RT code as the basis for atmospheric correction, we have developed an atmospheric correction scheme which allows the user to interact with 6S RT code with an increased level of user customization and regionalization of input atmospheric parameters. Supporting a range of multispectral and hyperspectral remote sensing sensors, the model developed allows the end user to exercise a wide range of model variables supported by the native 6S RT code. We demonstrate the application of the proposed atmospheric correction scheme using remote sensors: LANDSAT-8 Optical Land Imager (OLI), WorldView-3, Hyperion, and AVIRIS-NG. The results have been validated by comparing the performance against the popular atmospheric schemes, FLAASH and ATREM, and using various statistical measures.

3.2 Methodology

The overall methodology is shown in Figure 3.1. As the 6S is originally coded in FORTRAN, it is not intuitive for its application on image based remote sensing data framework. We adapted the python interface developed by Wilson (2013) for further design and development to result in an image-based framework interacting with the 6S RT code. We began by building up the look-up-table (LUT) containing several atmospheric variables as input and store output variables required for the inversion of the RT equation. The detailed design process of the LUT is presented in the later sections. Spectral response function of a specific sensor to compute the corresponding the output values specific to the sensor.

3.2.1 6S atmospheric correction scheme

The 6S code estimates satellite signal between 0.25 and 4 μm of the solar spectrum. As discussed in section 2.2, we retrieved spherical albedo (s), total transmittance ($T(\theta_s), T(\theta_v)$) and atmospheric path reflectance (ρ_a) for different input parameter combinations and stored in the look-up table. When the atmospheric correction is required, equation (2.2) is inverted to obtain atmospherically corrected reflectance according to equation (2.3).

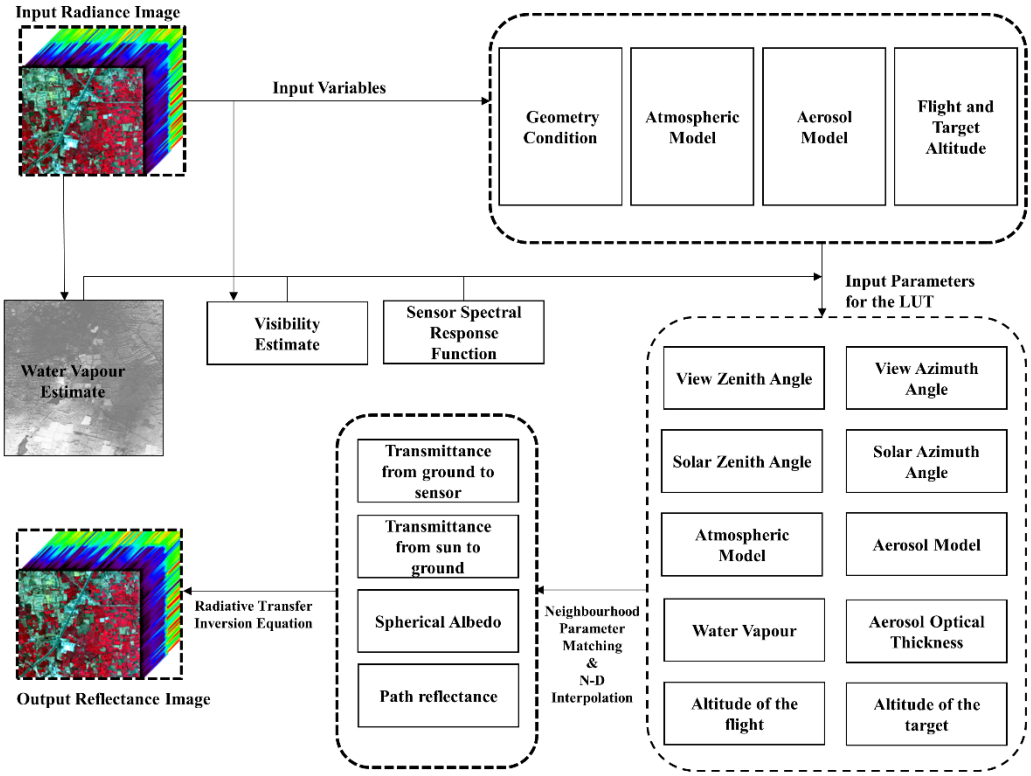

Figure 3.1: An overall architectural framework for the development of FACT atmospheric correction method.

3.2.2 Look-up table design

The 6S model requires various input parameters like viewing geometry condition, atmospheric conditions, aerosol model, visibility/optical thickness estimate, and target elevation. Since typical remote sensing imagery have a very wider areal coverage (a very large number of pixels), the direct pixel-by-pixel atmospheric correction would require a very high processing time, run into several days. In addition, correction coefficients have to be computed every time we need to correct an imagery. To solve these challenges we adapted a LUT approach (shown in the Table 3.1) as used in other works (Gao, Heidebrecht, & Goetz 1993; Griffin & Burke, 2003; Guanter, Alonso, & Moreno, 2007; Gao et al.,2009; Hu et al.,2012). The proposed scheme supports various atmospheric and aerosol models supported by the native 6S. The break points for the LUT entries (e.g., 80^0 for the azimuth angles, 15^0 for the zenith angles) have been chosen such that the proposed scheme has optimal computational and memory overhead while ensuring that the parameters' range covers the gamut of the typical acquisition

geometrical specifications of most of the satellite and airborne remote sensors. It may also be noted that the proposed scheme supports airborne platforms, hence the look-up table contain the sensor's platform elevation and water vapour as part of the input parameter set. The range of AOT and the intervals within it is chosen such that the proposed scheme supports the correction of imagery acquired when then the visibility is 5Km or more. It may be noted that a high value of AOT would produce high values of path reflectance and consequently negative values of surface reflectance (Richter & Schläpfer, 2011), thus we avoided choosing high AOT values (>0.7). The look-up table was simulated at 2.5nm interval to store the values of upward transmittance ($T(\theta_v)$), downward transmittance ($T(\theta_s)$), spherical albedo (s) and atmospheric path reflectance (ρ_a). We used a k-d tree construct (Bentley, 1975), which is a multidimensional binary search tree, for searching a tuple query corresponding to a combination of the input parameters of the look-up table (10-dimesional space). Using a k-d tree, we formulated a tree consisting of the nodes as the input parameter for the look-up table. For the interpolation of the stored values, we used the N-dimensional nearest neighbourhood interpolation technique.

3.2.3 Aerosol optical thickness (AOT) estimation

For solving any RT equation, estimation of the optical properties (optical thickness, scattering albedo, phase function), which depend on the particle size and shape, of the atmosphere is essential (Liang, 2005). Atmospheric loading is described by the AOT at 550nm and is one of the parameters required for solving the 6S RT equation. Kaufman (1993) observed that AOT has a significant effect on the path radiance and has derived the empirical relationships between optical thickness and path radiance.

Table 3.1: Design of the LUT for the development of FACT (6S based) atmospheric correction method.

Parameters	Range	Interval	Values
Aerosol Model			6S standard models
Atmospheric Model			6S standard models
View Zenith Angle	$0\text{-}60^0$	15^0	0,15…..60
Solar Zenith Angle	$0\text{-}75^0$	15^0	0,15…..75
View Azimuth Angle	$0\text{-}360^0$	80^0	0,80…360
Solar Azimuth Angle	$0\text{-}360^0$	80^0	0,80…360
AOT	0-0.7	-	0.03,0.12,0.2,0.3,0.4,0.7
Water Vapour	0-5 (g/cm^2)	-	0,0.4,0.8,1.2,1.6,2,3.5,5
Altitude of the Flight (for Airborne sensors)	0-6 Km	-	1,3,6
Altitude of Target	0-7 Km	-	0,1,2,4

He further discusses the use of vegetation, soil or water features for the derivation of AOT from the satellite image, popularly known as dense dark vegetation (DDV), which is used in the proposed FACT for AOT estimation. This approach is found to be computationally efficient and is viable for integration with the atmospheric correction module. The framework begins by reading the geometrical parameters (solar and view zenith angle) of the input image. For calculating the TOA radiance of the darkest pixel, we assume a threshold count of $\log(n^2) + \sqrt{n}$ where n is the total number of pixels in the imagery. According to Hill and Sturm (1991), the at-sensor reflectance ρ_t can be modelled as:

$$\rho_t = \frac{\pi\,(L_t - L_p)}{t(\mu) \uparrow . E_g}, \tag{3.1}$$

where L_t is the at-satellite radiance, L_p is the total atmospheric path radiance, $t(\mu)\uparrow$ is the direct atmospheric transmittance and E_g is the global irradiance reaching the ground. The variables E_g and $t(\mu)\uparrow$ were calculated using:

$$E_g = E_0 e^{\left[\left\{-\left(\frac{1}{2\tau_r}+\frac{1}{6\tau_\alpha}\right)\right\}/\mu\right]}, \quad (3.2)$$

where E_0 is the solar irradiance at the top of the atmosphere, τ_r is the Rayleigh optical thickness, μ is the cosine of the solar zenith angle and τ_α is the AOT.

$$t(\mu)\uparrow = e^{[-(\tau_r+\tau_a)/\mu]}, \quad (3.3)$$

Rayleigh optical thickness as approximated by Moller (1957) is given by:

$$\tau_r = 0.00879\ {\lambda_c}^{-4.09}, \quad (3.4)$$

where λ_c is the central wavelength of the band being used for calculating the AOT. Since atmospheric radiation scattering is primarily caused by Rayleigh and Mie scattering phenomena (Kaufman and Sendra 1988), total path radiance can be written as:

$$L_p = L_{pr} + L_{pa}, \quad (3.5)$$

where L_{pr} is the atmospheric path radiance due to Rayleigh scattering and L_{pa} is the atmospheric path radiance due to Mie scattering. Path radiance due to Rayleigh scattering phenomenon was calculated using approximation given by Gilabert, Conese, and Maselli (1994), which is as follows:

$$L_{pr} = \left\{\frac{(E_0 \cos\theta_0\ P_r)}{4\pi(\cos\theta_0 + \cos\theta_v)}\right\} * \left\{1 - e^{-\tau_r\left(\frac{1}{\cos\theta_0}+\frac{1}{\cos\theta_v}\right)}\right\} *\ t_{H_2O}\uparrow . t_{O_3}\uparrow, \quad (3.6)$$

where P_r is the Rayleigh scattering phase function, θ_0 is the solar zenith angle, θ_v is the sensor viewing angle, $t_{H_2O}\uparrow$ is the transmittance factor due to water vapour, and $t_{O_3}\uparrow$ is the transmittance factor due to ozone. Atmospheric path radiance due to Mie scattering was calculated using the equation given in the work carried out by Themistocleous et al. (2012) and is as follows:

$$L_{pa} = \omega_a * \left\{ \frac{E_0 \cos(\theta_0)\, P_a}{4\pi \cos\theta_0 + \cos\theta_v} \right\} * \left\{ 1 - e^{-\tau_\alpha \left(\frac{1}{\cos\theta_0} + \frac{1}{\cos\theta_v} \right)} \right\} * \left\{ e^{-\tau_r \left(\frac{1}{\cos\theta_0} + \frac{1}{\cos\theta_v} \right)} \right\}, \quad (3.7)$$

where, ω_a is the aerosol single scattering albedo (approximately taken as 0.80), and P_a is the aerosol scattering phase function. The value of P_a was taken from AERONET available at https://aeronet.gsfc.nasa.gov/. Solving equation (3.5) using equations (3.1), (3.2), (3.3), (3.6) and (3.7) yields the AOT estimate. After the estimation of AOT, visibility estimate was calculated by the 6S RT code based on McClatchey et al. (1972) model.

3.2.4 Water vapour estimation

The inherent capability of hyperspectral remote sensors to acquire data in contiguous and narrow spectral bands in the range 350nm to 2500nm permits image-based estimation of CWV required for solving the RT equation. CIBR, one of the popular differential absorption techniques (Schläpfer et al., 1998) used for water vapour estimation, was adapted for retrieving water vapour in this work. CIBR is a ratio of the absorption radiance (L_m) at a wavelength (λ_m) to a linearly interpolated value between two non-absorption radiances (L_{r1}, L_{r2}) on either side of the measurement radiance at a wavelengths ($\lambda_{r1}, \lambda_{r2}$). The ratio is given by:

$$R_{CIBR} = \frac{L_m}{\omega_{r1} L_{r1} + \omega_{r2} L_{r2}}, \quad (3.7)$$

where $\omega_{r1} = \frac{\lambda_{r2} - \lambda_m}{\lambda_{r2} - \lambda_{r1}}$, $\omega_{r2} = \frac{\lambda_m - \lambda_{r1}}{\lambda_{r2} - \lambda_{r1}}$ and R_{CIBR} is the CIBR ratio and ω_{r1} and ω_{r2} are weighted factors. As the differential absorption technique provides only a ratio, the outcome of CIBR was transformed to water vapour content using an exponential approach (Carrère and Conel (1993)) given as :

$$T_{wv}(PW) \approx R_{CIBR} = e^{-(\gamma + \alpha (PW)^\beta)}, \quad (3.8)$$

where $T_{wv}(PW)$ is the total water vapour content and α, β and γ are the empirical regression parameters for solving the water vapour amount using the expression:

$$PW(R_{CIBR}) = -\left(\frac{\ln(R_{CIBR}) + \gamma}{\alpha}\right)^{1/\beta}. \quad (3.9)$$

The procedure to calculate the water vapour begins by generating a LUT using 6S RT code which stores radiance and path radiance values for the various combinations of water vapour content, sensor altitude, target altitude, and visibility conditions at a fixed average reflective background reflectance (0.4) as suggested by Borel and Schlaepfer (1996). We then calculated the ratio R from the LUT generated values for all the possible combinations and fit all the values in equation (3.9) for estimating the parameters α, β and γ. Subsequently, with the parameters α, β and γ, we converted the ratio to water vapour amount for the entire imagery.

3.2.5 Experimental implementation

A robust atmospheric correction module should support correction of a range of multispectral and hyperspectral remote sensors, and, preferably, support the user-led open-end integration of future remote sensors. While the existing operational atmospheric correction modules support a range of remote sensors, they are close-end frameworks from the user perspective as the users have no possibility to self-compute and integration choice of present and future remote sensors. In an attempt to enable the user community, meet the atmospheric correction requirements of future space-borne remote sensors and conventional and unmanned airborne spectral imaging platforms, the present atmospheric correction framework has the capability to add customized sensors with minimal computational demands. The present framework supports a range of multispectral and hyperspectral sensors including Landsat-8 OLI, Sentinel – 2, WorldView – 2, WorldView – 3, ASTER, LISS III, LISS-IV, Hyperion, and AVIRIS-NG.

3.2.6 Datasets

For evaluation of the overall performance of the developed atmospheric correction scheme, we corrected imagery acquired from various multispectral and hyperspectral sensors. Details of the imagery used are presented Table 3.2. Except for the AVIRIS-NG imagery, we used the standard tropical atmospheric model with the continental aerosol model since AVIRIS-NG is an airborne sensor unlike the other space-borne sensors in this study.

Table 3.2: Datasets used for evaluation of the proposed FACT

Sensor	Image Dimension (row x col)	Study Area	Spatial Resolution (m)	Total Spectral Channels
Landsat-8 OLI	2701 x 3536	Himalayan Foothills, India, 2015	30	11
WorldView-3	1487 x 1392	Bangalore, India, 2017	multiple	29
AVIRIS-NG	327 x 359	Ahmedabad, India,2016	4	425
Hyperion	160 x 267	Rishikesh, India, 2014	30	242

3.2.7 Quantitative and comparative evaluation of the performance of FACT

The performance of the developed atmospheric correction framework was validated by computing multiple statistical error measures and also by pixel-to-pixel (P2P) level cross-comparison of the results from an operational atmosphere correction module FLAASH. For all the imagery, we computed the spatial mean absolute error (S-MAE), the spatial root mean square error (S-RMSE) and compared correction results with the FLAASH corrected imagery. We have chosen the FLAASH atmospheric correction scheme for comparison due to the fact that it is the most widely used operational atmospheric correction module in the remote sensing scientific community. Spatial error evaluation helps to provide a reliable and unbiased estimate of the error in each pixel. Consider each pixel to be a $k \times 1$ vector where k is the number of bands. Let X_i

and Y_i be the i^{th} pixel where X and Y are two images covering same geographical extent with an equal number of spatial pixels and same spatial resolution; the S-MAE is given by:

$$\mathrm{S-MAE} = \frac{\left\{\left|\left(X_{i_1} - Y_{i_1}\right)\right| + \left|\left(X_{i_2} - Y_{i_2}\right)\right| + \ . \ . \ . \ + \left|\left(X_{i_k} - Y_{i_k}\right)\right|\right\}}{\mathrm{k}}. \quad (3.10)$$

Similarly, the S-RMSE is given by:

$$\mathrm{S-RMSE} = \sqrt{\frac{\left\{\left(X_{i_1} - Y_{i_1}\right)^2 + \left(X_{i_2} - Y_{i_2}\right)^2 + \ . \ . \ . \ + \left(X_{i_k} - Y_{i_k}\right)^2\right\}}{\mathrm{k}}}. \quad (3.11)$$

A histogram of the residuals was generated to analyse the range of the residuals and their spread. In addition, various statistical measures such as minimum, maximum, mean and standard deviation of the residual terms were computed. Though it may be noted that "mean error" in itself is ambiguous, drawing inference on the spread of error is possible from the measure of "mean error". The above measures are strictly statistical in nature and thus may not reflect upon the error occurred in the underlying physical process. To understand the qualitative performance of the developed methodological framework in comparison with other atmospheric correction schemes, we compared the corrected reflectance cube (in various spectral channels of the given imaging sensor) obtained from different atmospheric correction schemes by calculating spectral-RMSE between reflectance cube obtained by the proposed FACT and reflectance cube obtained from other atmospheric correction schemes. This comparison helps to understand the exact response and extent of the atmospheric correction occurred at a given wavelength band of the electromagnetic spectrum.

3.3. Results and Analysis

As described in section 3.2.6, the proposed atmospheric correction scheme was applied on four different remote sensing datasets – two datasets from multispectral sensors and two datasets from hyperspectral sensors. Results are presented in the following sub-

sections in the order of remote sensing sensors – AVIRIS-NG, Hyperion, WorldView-3, and OLI of Landsat-8.

3.3.1 Atmospheric correction of the AVIRIS-NG

Results of the atmospheric correction of AVIRIS-NG data and its comparison with the results from FLAASH and NASA JPL's scheme are presented in Figures 3.2 and 3.3. The average water vapour content estimated by the proposed scheme is 1.417cm as against 1.3241cm and 1.723cm respectively from the FLAASH and NASA JPL's scheme. The visual quality features of the atmospherically corrected remote sensing imagery (e.g., contrast, sharpness) closely match with that of FLAASH, and NASA JPL's scheme. The quality of atmospheric correction as observed at within-image scale considering typical land surface features was also assessed. As evident from Figure 3, while vegetation features appear similar in all the three correction schemes, built-up features vary substantially from each other. Close examination reveals that a few built-up features exhibit rapid transitions in spectral reflectance. This might be due to the apparently high reflective nature of built-up constructed with cement and gravels and apparent spatial adjacency effect. Since there is no correction mechanism introduced for adjusting the spatial adjacency effect in the proposed FACT scheme, few regions of AVIRIS-NG imagery with certain built-up features exhibit moderate to higher S-RMSE. The spread of residuals is presented in Figure 3.4 and Table 3.3. For 99.936% of the pixels in the AVIRIS-NG imagery, the computed S-RMSE between the proposed FACT and the FLAASH scheme is very negligible and is within 0.0563. Similarly, 99.94% of AVIRIS-NG pixels exhibit an S-RMSE of 0.101 when the proposed FACT scheme is compared with NASA JPL's scheme. This is marginally lower or at par with the results obtained from the comparison of the FLAASH with NASA JPL's scheme, where 99.929% of the pixels are found to be within S-RMSE of 0.1064. On close analysis of the statistical figures given in the Table 3.3, we find that the maximum values for error terms for all the correction schemes appear high. However, the distribution of the error and the number of pixels reveals that the error terms are inflated by a single outlier pixel; the reason for its erratic behaviour is unclear.

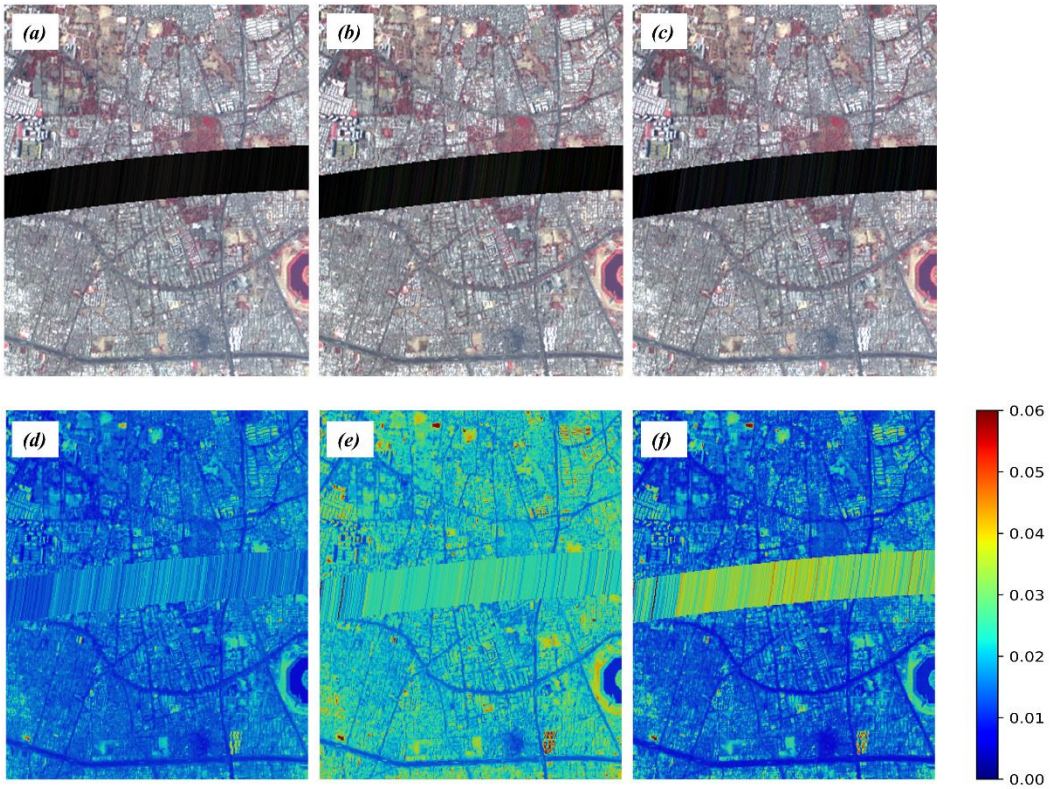

Figure 3.2: Results of atmospheric correction of AVIRIS-NG imagery: (a) – (c) False Colour Composites of the corrected imagery from the proposed FACT, FLAASH and NASA JPL's atmospheric correction scheme respectively; (d) – (f) Spatial –Mean Absolute Error (S-MAE) image between the proposed FACT-FLAASH, FLAASH-NASA JPL's and FACT-NASA JPL's scheme respectively.

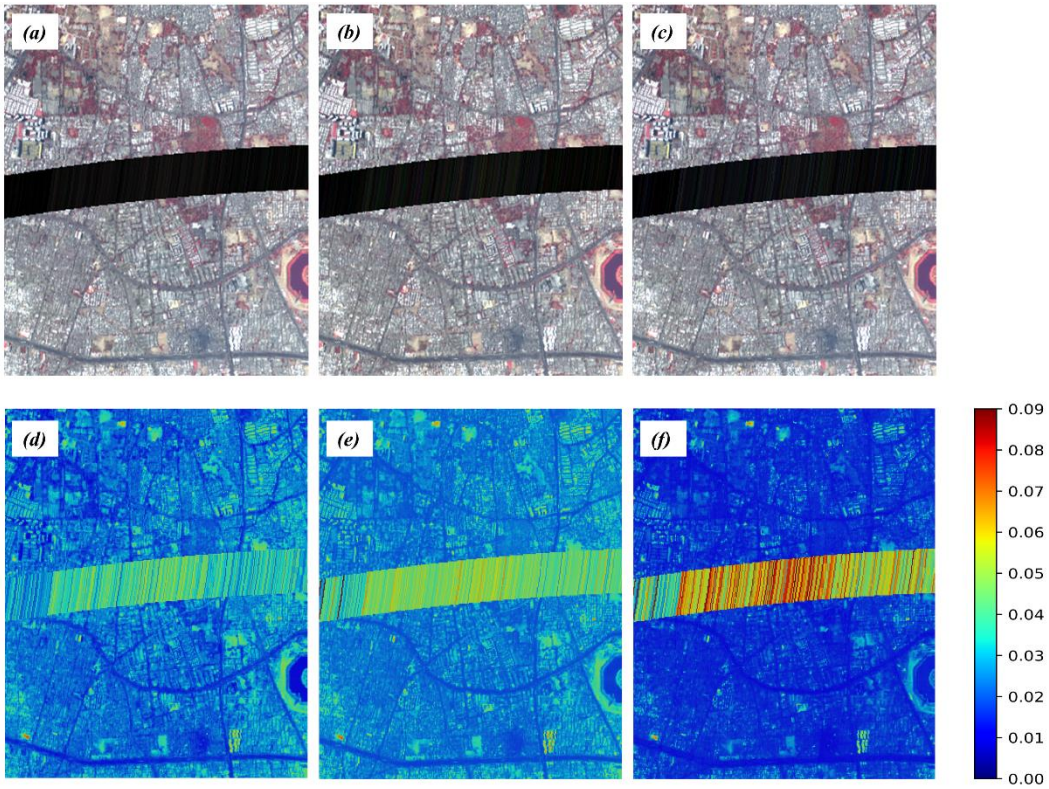

Figure 3.3: Results of atmospheric correction of AVIRIS-NG imagery: (*a*) – (*c*) False Colour Composites of the corrected imagery from the proposed FACT, FLAASH and NASA JPL's atmospheric correction scheme respectively; (*d*) – (*f*) Spatial – Root Mean Square Error (S-RMSE) image between the proposed FACT-FLAASH, FLAASH-NASA JPL's and FACT-NASA JPL's scheme respectively.

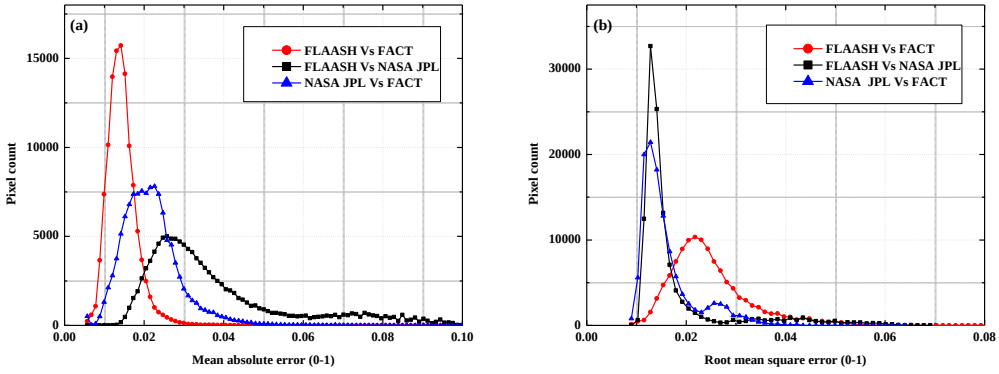

Figure 3.4: The (*a*) spatial-MAE and (*b*) spatial-RMSE histogram for the AVIRIS-NG corrected imagery by FLAASH, the proposed FACT and NASA JPL's correction method.

3.3.2 Atmospheric correction of the Hyperion imagery

Results of error evaluation from the comparison of the FLAASH corrected imagery and the proposed FACT are shown in the Figures 3.5, 3.6 and Table 3.3. As reported in the case of AVIRIS-NG (section 3.3.1), visual features such as contrast and sharpness for the Hyperion imagery corrected by the proposed FACT are retained when compared to the imagery corrected by the FLAASH (Figure not shown). Since correction was done using the standard atmospheric model, no CWV was retrieved. Analysis of feature level accuracy indicates a high correlation and corresponding lower error (both S-MAE and S-RMSE of the order 0.02) for vegetation and deep-water feature, as observed in Figure 3.5 between the imagery corrected by the FLAASH and the proposed FACT. A notable performance gain in the deep-water feature (MAE and S-RMSE within 0.01) can be easily inferred from the Figure 3.5. In addition to these performance gains, we observed a marginal higher error (in the range of 0.04 to 0.07) in some of the features such as highly reflective dried river beds mixed with sands, high mountainous landscapes and few built-up features. These errors are consistent with both the Hyperion as well AVIRIS-NG, indicating a systematic difference in modelling the signals from objects having high reflectivity. Considering all the different sources of errors, FACT achieves an accuracy of around 95% (99.9% of 42,720 pixels having S-RMSE of 0.069 and MAE of 0.054 calculated from the histogram as shown in Figure 3.6).

Table 3.3: Spatial-Error statistics for the subset of different satellite imagery

		Spatial Root Mean Square Error Statistics				Spatial Mean Absolute Error Statistics			
Imaging Sensor	**Comparison Schemes**	**Min**	**Max**	$\boldsymbol{\mu}$	$\boldsymbol{\sigma}$	**Min**	**Max**	$\boldsymbol{\mu}$	$\boldsymbol{\sigma}$
AVIRIS-NG	FACT Vs FLAASH Corrected	0.0089	0.3349	0.0252	0.0078	0.0057	0.2751	0.0150	0.0038
	FACT Vs NASA JPL's Corrected	0.0158	0.5168	0.0279	0.0135	0.0090	0.2289	0.0226	0.0061
	FLAASH Vs NASA JPL's Corrected	0.0074	0.5111	0.0219	0.0180	0.0035	0.1113	0.0167	0.0075
HYPERION EO-1	FACT Vs FLAASH Corrected	0.0069	0.0917	0.2087	0.0053	0.0038	0.0756	0.0125	0.0049
LANDSAT-8 OLI	FACT Vs FLAASH Corrected	0.0045	0.1407	0.0165	0.0026	0.0038	0.1282	0.0136	0.0025
WV-3	FACT Vs FLAASH Corrected	0.0011	0.3505	0.0071	0.0038	0.0008	0.2337	0.0060	0.0032

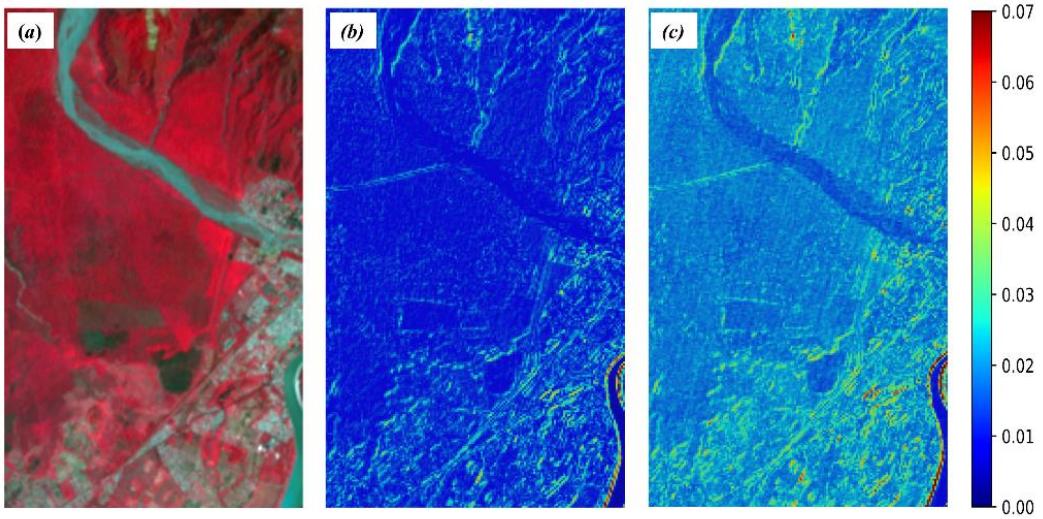

Figure 3.5: Results of atmospheric correction of Hyperion imagery: (a) False Colour Composites of the corrected imagery from the proposed FACT, (b) Mean Absolute error (c) and Root Mean Square Error image between the proposed FACT and FLAASH atmospheric correction method.

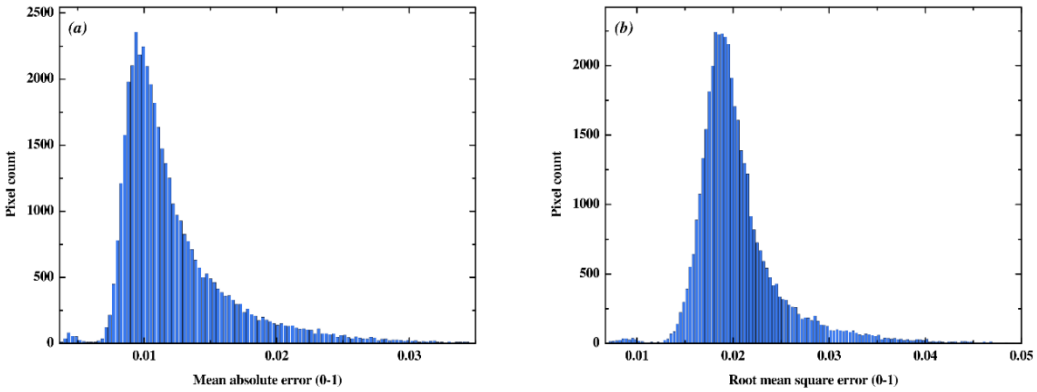

Figure 3.6: The (a) spatial-MAE and (b) spatial-RMSE histogram for the HYPERION EO-1 imagery calculated between atmospherically corrected image by FLAASH and the proposed FACT .

3.3.3 Atmospheric correction of the LANDSAT-8 OLI imagery

The comparative evaluation of the correction results from the FLAASH and the proposed FACT scheme for LANSAT-8 OLI imagery is shown in Figure 3.7, 3.8 and Table 3.3. For this imagery, we used the standard tropical atmospheric model with the continental aerosol model. Other geometrical parameters required were retrieved from the metadata file and were given as input to the FACT correction scheme. Based on the results of statistical analysis and computation of the S-MAE and S-RMSE (as shown in

Figure 3.8), we observe that 99.9% of the pixels have S-RMSE equal to or less than 0.045, while S-MAE less than or equal to 0.042 (out of total 9550736 pixels). As observed in the case of AVIRIS-NG and the Hyperion imaging sensors, we observe a substantial disagreement (S-RMSE and S-MAE) for the landscapes that include built-up features and dried river beds. In addition, a few pixels of the observable cloud patches indicate substantial disagreement. Since cloud masking is inherently not part of any RT code, we believe any error analysis should ignore such pixels for drawing qualitative inferences about the developed atmospheric correction scheme. Despite the lack of a close matching for a few pixels, we believe that, with the overall spatial accuracy close to 96%, the proposed FACT atmospheric correction scheme compares well with the FLAASH atmospheric correction scheme.

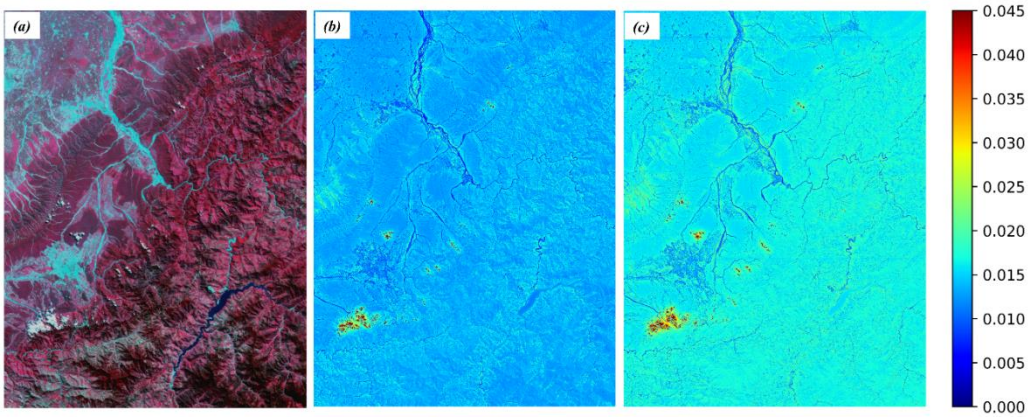

Figure 3.7: Results of atmospheric correction of LADSAT-8 OLI imagery: (a) False Colour Composites of the corrected imagery from the proposed FACT, (b) Mean Absolute error (c) and Root Mean Square Error image between the proposed FACT and FLAASH atmospheric correction method.

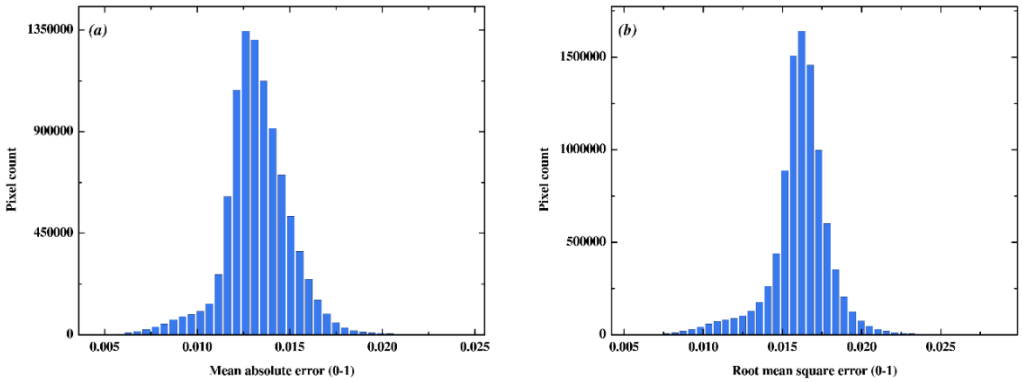

Figure 3.8: The (*a*) spatial-MAE and (*b*) spatial-RMSE histogram for the LANDSAT-8 OLI imagery calculated between atmospherically corrected image by FLAASH and the proposed FACT.

3.3.4 Atmospheric correction of the WorldView-3 imagery

Results of the comparative evaluation of the correction from the FLAASH and the proposed FACT atmospheric correction schemes for the WorldView-3 imagery are presented in Figure 3.9, 3.10 and Table 3.3. As evident from the Figure 3.9, we find an improved level of accuracy (99.9% of pixels have MAE of 0.031904, while RMSE of 0.039464 out of 2,069,904 total pixels computed from Figure 3.10) for the WorldView-3 imagery when compared to other corrected imagery using the proposed FACT atmospheric correction. The relatively better performance, apparent amongst all the imagery considered for the comparative analysis, can be attributed to a higher Signal to Noise Ratio (SNR). In addition, apparent statistical improvement in the performance of the proposed FACT scheme can also be attributed to the uniform distribution of different classes of materials in the imagery. Although we observe a substantial gain in the performance metrics, nature of reflectance spectrum obtained for the materials with high reflectivity (such as roof-top or soil mixed with sands which is observable in Figure 3.9) shows persistent error as found in all the other imagery considered. Apart from the marginal error in a few of the pixels, the proposed FACT atmospheric correction scheme achieved an overall accuracy of about 98%.

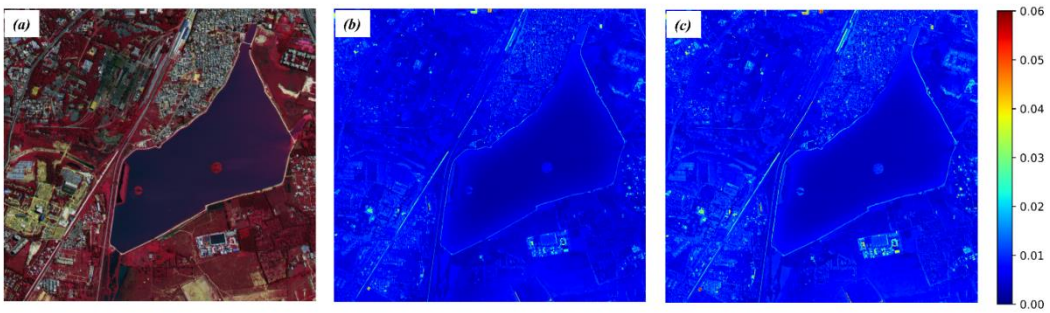

Figure 3.9: Results of atmospheric correction of WorldView-3 imagery: (a) False Colour Composites of the corrected imagery from the proposed FACT, (b) Mean Absolute error (c) and Root Mean Square Error image between the proposed FACT and FLAASH atmospheric correction method.

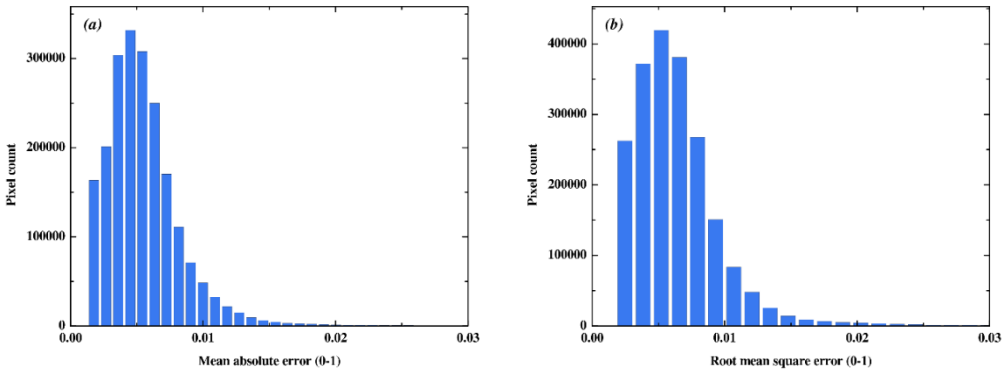

Figure 3.10: The (a) spatial-MAE and (b) spatial-RMSE histogram for the WorldView-3 imagery calculated between atmospherically corrected image by FLAASH and the proposed FACT.

3.3.5 Spectral-statistical performance of FACT

As reported in the section above, analysis of spatial residual (S-RMSE and S-MAE) errors clearly indicate a close agreement between the proposed FACT atmospheric correction scheme and the FLAASH correction scheme. However, these results are generally statistical in nature and for an exhaustive evaluation of the developed atmospheric correction scheme, it is required to analyse the performance of the proposed FACT in each spectral channel. Spectral evaluation of the corrected reflectance spectrum from various atmospheric correction scheme provides an insight into the principles of the physical process involved thereby enabling us to dissect the scientific gaps in more detail. Such analytical assessment helps to refine the estimation processes involved in obtaining the input parameters for the atmospheric correction scheme. In Figure 3.11(*b-d*), we present a comparison of the spectral (band wise) accuracy of the proposed FACT atmospheric correction scheme with the FLAASH atmospheric correction scheme for the Hyperion, LANDSAT-8 OLI and WorldView-3 imagery. For the spectral evaluation of AVIRIS-NG data (Figure 3.11(*a*)), we performed an inter-comparison of corrected imagery obtained from the proposed FACT, FLAASH and NASA JPL's scheme.

As clear from the Figure 3.11(*c*) and 3.11(*d*), consistent band-wise spectral conformity of the proposed FACT scheme is evident for the multispectral sensors, Landsat-8 (OLI), and WorldView-3. However, the band-wise comparative performance

for the hyperspectral sensors (Figure 3.11(*a*) and Figure 3.11(*b*)) indicates two distinct features across the optical wavelength regions covered by these sensors. On the one hand, the observed consistently low S-RMSE levels for both the hyperspectral imagery (see Figure 3.3(*d-f*), and Figure 3.5) across the atmospheric correction schemes compared indicates that the results from the proposed FACT scheme are precise and accurate. However, on the other hand, despite the apparent overall higher level agreement between the proposed FACT and FLAASH, and NASA JPL's schemes (with minimal values of spectral-RMSE; 0.05 for AVIRIS – NG; 0.03 for Hyperion, 0.02, in case of LANDSAT-8 OLI and close to 0.01 in case of WorldView-3), there are a few discrete spikes in the Spectral-RMSE. Apparently, these spikes of Spectral-RMSE are found positioned at the wavelengths in the electromagnetic spectrum where water vapour absorption is the dominant phenomenon. The AVIRIS-NG acquires measurements in 400 – 2500 nm range of electromagnetic spectrum and retains spectral measurements in the strong water absorption regions around 932 nm to 942 nm and 1117 nm to 1147 nm.

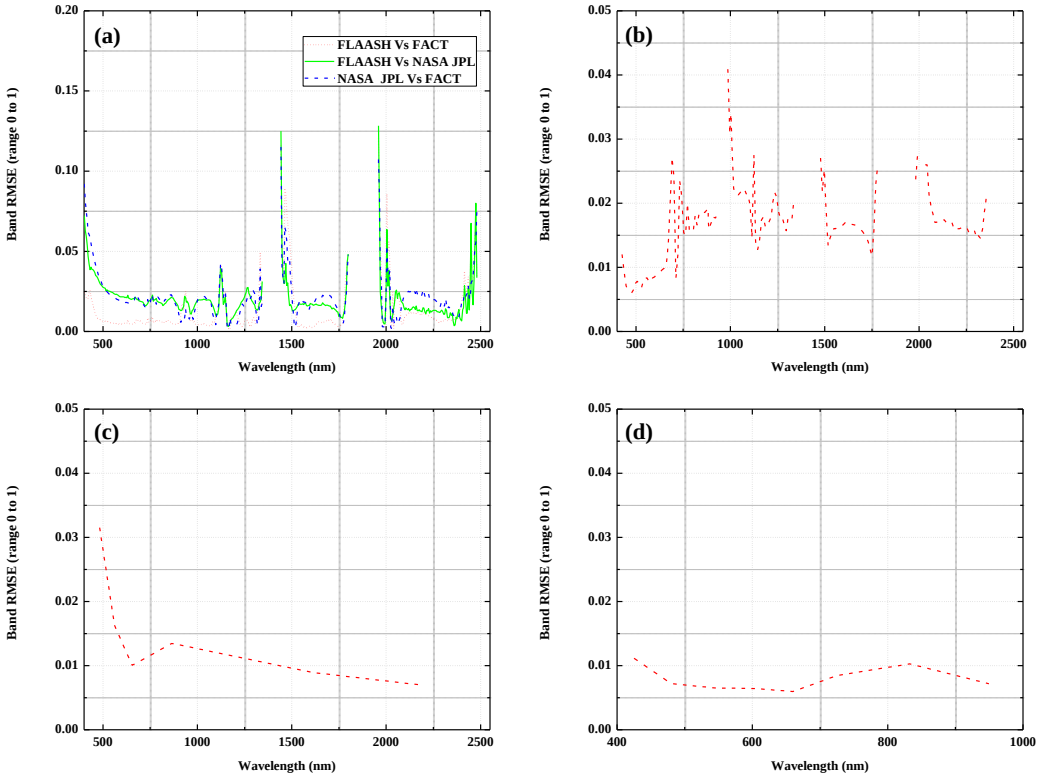

Figure 3.11: A spectral analysis (band wise RMSE calculation) for the imagery data of (a) AVIRIS-NG (b) Hyperion (c) LANDSAT-8 OLI and (d) WorldView-3 corrected by the FLAASH, the NASA JPL's and the proposed FACT correction method in case of AVIRIS-NG and by the FLAASH and the proposed FACT in other three cases.

In addition to the generally lower or lack of calibration for the spectral bands in water vapour absorbing wavelength regions, the manner in which different RT codes model the signal also determines the level of conformity of the atmospheric correction. Further, the method by which CWV is estimated, which is found to be different by all the three atmospheric correction schemes (see section 3.3.1), can contribute substantial error in the atmospheric correction. Apart from the occurrence of error at the water vapour absorbing wavelength regions, we notice the occurrence of error spikes at a few other discrete locations (approximately at 1448 nm, 1964 nm and at the end after 2380nm; please see Figure 3.11(*a*) and 3.11(*b*)). This pattern can be observed in both the hyperspectral imagery corrected by all the three atmospheric correction schemes considered. Although the reason for the occurrence of these spikes is not comprehensible, we assume the manner in which the RT code inverts the signal can be one of the causes for such behaviour. Apart from errors in the absorption region, the performance of the proposed FACT scheme in case of hyperspectral imagery is

satisfactory with an accuracy of more than 95% when compared to the other atmospheric correction schemes.

3.4. Discussion

Atmospheric correction of satellite-derived imagery is an important pre-processing in the spatio-temporal analysis of remote sensing data for various applications. However, the applicability of these methods and quality of the reflectance data obtained depend on the RT models being used for atmospheric correction and estimates of the various input parameters to these models. With the transforming imaging technology, it is also expected that the atmospheric correction technique should account for the regional atmospheric variables associated with the imagery. Thus, an atmospheric correction scheme should be flexible to account for changing long-term atmospheric conditions and open-ended at the user level to incorporate various remote sensing sensors being developed. We have assessed the possibility of developing an atmospheric correction scheme which provides a user-level customization functionality. In order to approximate for accurate reflectance data and for estimating several input parameters high computational speed, we have adapted the look-up architecture. For an exhaustive evaluation of the proposed correction scheme, several statistical analyses were carried out on the results obtained from the proposed correction scheme against the other atmospheric correction schemes.

AOT is one of the important input parameters for the atmospheric correction scheme to obtain a reliable approximation of the corrected reflectance cube. On one hand, FLAASH uses K-T method for the estimation of visibility which requires two channels to be defined (one around 660nm and the other at 2100 nm). Whereas, the proposed FACT uses radiance single channel (around 550nm) i for calculating the AOT. In the absence of specific spectral channels, FLAASH fails to estimate visibility. In such cases, the user is prompted to supply visibility estimate based on the haze level in the imagery depending on the visual appearance, which may be subjective and in turn affect the accuracy and quality of the obtained corrected imagery. Unlike the proposed FACT, FLAASH doesn’t report the AOT directly making it difficult to

validate the data (visibility to AOT estimate) against the ground truth data which might be collected from the respective AERONET center. This gives the proposed FACT a relative edge over the other schemes for atmospheric correction of multispectral imagery which lack spectral measurements around 2100 nm.

Spatial statistical analysis (S-RMSE and S-MAE) for both the hyperspectral as well as multispectral imagery reveals that a few pixels have a relatively high error when compared to the other pixels in the image. It has been found that these pixels represent material of high reflectivity (e.g., roof-tops, sands, dried river beds) and thus show consistently moderate disagreement between the corrected reflectance spectrum approximated by the proposed atmospheric correction scheme FACT and FLAASH. For the hyperspectral imaging sensors, an overall spectral conformity of about 95% is achieved when compared to the different atmospherically corrected imagery from FLAASH and NASA JPL's correction scheme. For the multispectral imaging sensors, the accuracy has increased to about 98% when compared to the FLAASH corrected imagery. In case of hyperspectral imaging sensors, we observe a systematic spectral error (see figure 3.11(*a*) and 3.11(*b*)) throughout the 400 nm to 2500 nm of the electromagnetic spectrum at the onset and closure of the transition occurring from the calibrated channel to the uncalibrated channel. Reason for these kinds of error may be the underlying difference in operating principle (6S is based on successive order of scattering while MODTRAN uses discrete ordinate) of the RT code which is being implemented in these atmospheric correction schemes (Guanter, 2006; Mandanici, 2010). Apart from these residuals, Spectral-RMSE at the absorption band is substantial for the hyperspectral imaging sensors. Though it affects the performance in the water absorption region, we have shown that the overall error from the proposed FACT atmospheric correction scheme based on 6S RT model for both AVIRIS-NG and Hyperion imaging sensor remains within 3-5% when compared to the FLAASH scheme.

We infer that within the given error window of 3-5%, the proposed FACT can be a competitive alternative to the existing FLAASH module for carrying out atmospheric correction of the imagery acquired from the hyperspectral or multispectral sensors. As a flexible correction scheme, the proposed FACT is open for integration of

any new sensor developed since it has an appropriate interface at the user level and can model the parameters based on the evolved regional atmospheric conditions. We believe that allowing this customization feature will give the FACT enough technical input and scientific merit so that it can delve into more mature and robust correction technique. This technique has been evaluated with data pertinent to the Indian subcontinent, but can be used elsewhere too, with the standard parameters defined in the proposed FACT. As a future initiative, we intend to make the proposed FACT available in a server-client based computing environment, thereby eliminating setup related infrastructural requirement.

3.5. Chapter Conclusions

In this chapter, an attempt has been made to explore the possibilities of developing a an open-ended atmospheric correction scheme. The proposed correction scheme has been compared and cross-validated with other existing atmospheric correction schemes. Results indicate that within acceptable limits, the proposed FACT can be used for atmospheric correction of a range of multispectral and hyperspectral sensors. However, it was noticed that for hyperspectral imaging sensors, especially air-borne imaging sensors, the scheme needs further improvement in parameter estimation to make the retrieved surface reflectance more accurate at the water absorption spectral region. Apart from the error observed in the absorption regions, performance of the proposed FACT in the case of the space-borne hyperspectral imaging sensor is found more accurate than the air-borne hyperspectral imaging sensors. The accuracy of the proposed FACT on water features is consistently high across all the imaging sensors, thus suitable for applications which are related to water quality assessment and various other studies related to it. At the current status of development, the proposed FACT presents a viable and reliable option for carrying out atmospheric correction of the multispectral and hyperspectral imaging sensors with the integration and optimization for regional atmospheric conditions.

CHAPTER 4

ENGINEERED MATERIAL TARGET DETECTION USING MULTI-PLATFORM REMOTE SENSING SETUP

Prelude: This chapter introduces the experimental setup of a novel multi-source and multi-platform benchmark dataset for engineered material-target detection based on reference spectral reflectance patterns. Positioning artificial targets on different surface backgrounds, we acquired remote sensing data from terrestrial, airborne, and space-borne sensors. Various statistical and subspace detection algorithms were applied on the benchmark dataset for the detection of targets, considering the different sources of reference target spectra, background, and the spectral continuity across the platforms. We validated the detection results using the ROC for different cases of detection algorithms and imaging platforms. Continuing the style of content organization followed in the previous chapter, this chapter is also self-contained in its entirety and encompasses the work related to one of the objectives of the thesis "development of a multi-platform (ground, airborne, and space-borne) target detection benchmark dataset and critical analysis of parameters of detection performance".[1]

4.1 Introduction

Based on one of the fundamental principles of remote sensing, spectral reflective signatures of different materials are distinct in the optical range of the electromagnetic spectrum (EM), remote sensing data have been used for land surface characterization

[1]The contents of this chapter are published in *Remote Sensing* Vol: 12(13), 2020 Publisher: Multidisciplinary Digital Publishing Institute. Authors: Sudhanshu Shekhar Jha, Rama Rao Nidamanuri.

from local to a global level. Building upon the broader application domain of hyperspectral remote sensing, various organizations have developed spectral libraries of reference spectral signatures for thousands of natural and human-made materials (Baldridge et al., 2009; Kokaly et al., 2017; Meerdink et al., 2019). Target detection is one of the general approaches of remote sensing which has a broader application perspective. Detecting targets - specific material objects (natural or engineered) of interest with a sparse spatial distribution in remote sensing imagery has been an active area of research. Various mapping and surveillance requirements in defense, mineralogy, and precision agriculture can be addressed quickly from a target detection perspective in remote sensing imagery. In principle, target pixels are sparse (about 10 pixels in a million), thus making their detection challenging. Target detection is influenced by choice of the detection algorithm, sensor, target - background dynamics, and atmospheric perturbance (Cohen et al., 2012b; Archer et al., 2013; Yadav et al., 2018b). From a target detection perspective, high-resolution multispectral imagery has been used for identifying common land use objects such as buildings, roads, vehicles, and ships (Cheng & Han, 2016; Kanjir et al., 2018). Hyperspectral imagery offers appropriate baseline spectral data with finer spectral resolution required for typical target detection problems.

There are some attempts on using hyperspectral data for target detection for military infrastructure (Briottet et al., 2006), surveillance (Yuen & Richardson, 2010), and mineral mapping (Molan et al., 2014; Hou et al., 2016; Dos Reis Salles et al., 2017). However, a comprehensive evaluation of the target detection in remote sensing data, particularly from the perspective of the vertical continuum of target spectral footprints in remote sensing imagery acquired from multiple platforms (ground, airborne, and space-borne) has not been explored. In addition, most of the reported works have approached the target detection problem from the general classification theory wherein a target object is one among the other multiple land use categories mapped. In addition to using a single source of remote sensing imagery, the land cover category considered as “target” to be detected has abundant spatial distribution and extent, which in theory does not qualify it to be called a target. One of the major impediments in this direction has been the lack of benchmark datasets in the public domain. Most of the recent works on target detection have used the Cooke City, USA,

made available by Rochester Institute of Technology (RIT), NY, USA (Snyder et al., 2008b) for the evaluation of existing and in-development target detection algorithms. Especially, reference remote sensing imagery on multi-platform-based target detection has not been reported so far. Further, most of the experimental data on target detection available for the research community is from a single platform, either airborne or space-borne. A multi-platform target detection experimental data that encompass remote sensing data from different sensors will enhance our understanding of the potential of target detection per se and the dynamics involved in a composite framework.

We have carried out a comprehensive experiment for the acquisition of multispectral (only from a space-borne platform), and hyperspectral imagery from ground, airborne, and space-borne platforms on several engineered/artificial target materials in a complex urban neighborhood. This portion of the research is aimed at exploring the target detection problem from various platforms of imaging and detection of targets in optical remote sensing data. The key research questions of this research are: How does the detection performance vary as a function of the imaging platform? What is the impact of local background–target interaction on detection rate? Is the detection rate reproducible for two identical targets? Multi-platform remote sensing datasets were experimentally evaluated for target detections under various scenarios, and the results were validated, computing various statistical measures, and the graphical ROC, since it is one of the most robust target detection metrics and is used ubiquitously (Manolakis, Marden & Shaw 2003; Cohen et al., 2012; Acito et al. 2016).

4.2 Materials and Methods

4.2.1 Experimental Design

The conceptual design of the experimental setup is shown in Figure 4.1. The experimental set up consisted of positioning five targets of different artificial thin-sheet materials of different colors (base material: nylon and cotton), each of the size 10 m × 10 m (Figure 4.2). For ease of referencing throughout the chapter, we designate a distinct name for each target used in Table 4.1. The third letter in the name of a target indicates the color of the target (G: green, R: red, W: white, Y: yellow, B: black).

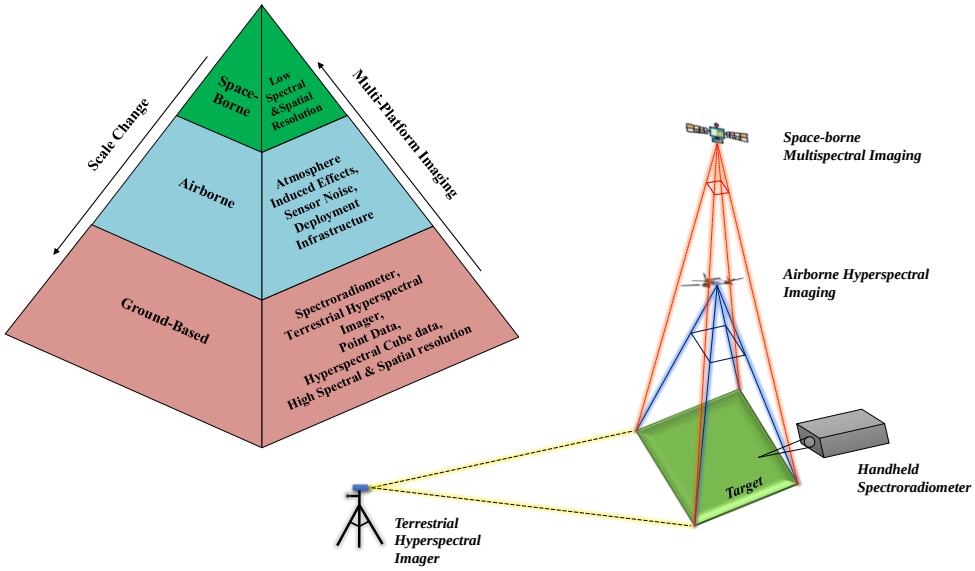

Figure 4.1: Conceptual design of the experimental set up used for the acquisition of multi-platform remote sensing data.

Table 4.1: Target materials and naming convention used in the chapter.

Target Material	Target Name
Green nylon sheet	N1G
Red nylon sheet	N2R
White cotton sheet	C1W
Yellow nylon sheet	N3Y
Black nylon sheet	N4B

Out of the five different target materials, we positioned three on natural grass and vegetation features as the background, and two on reflective soil background. To introduce a moderate degree of background resemblance to natural camouflage in the visible spectral range of the electromagnetic spectrum, we positioned two targets (N1G and N3Y) on the grass and soil background. To assess the target detection of materials with broadly similar spectral reflectance characteristics, we chose multiple targets with a single base material but in different colors. Ensuring an overlapping areal extent of the imagery from both the airborne and space-borne platforms, we extracted a subset of the data acquired. The datasets maintain SNR ratio close to one in a million for different

scene elements under the different spatial-spectral variabilities of materials in the scene. A true color composite of the airborne hyperspectral imagery marked with footprints of the targets and the corresponding ground truth imagery are shown in Figure 4.2.

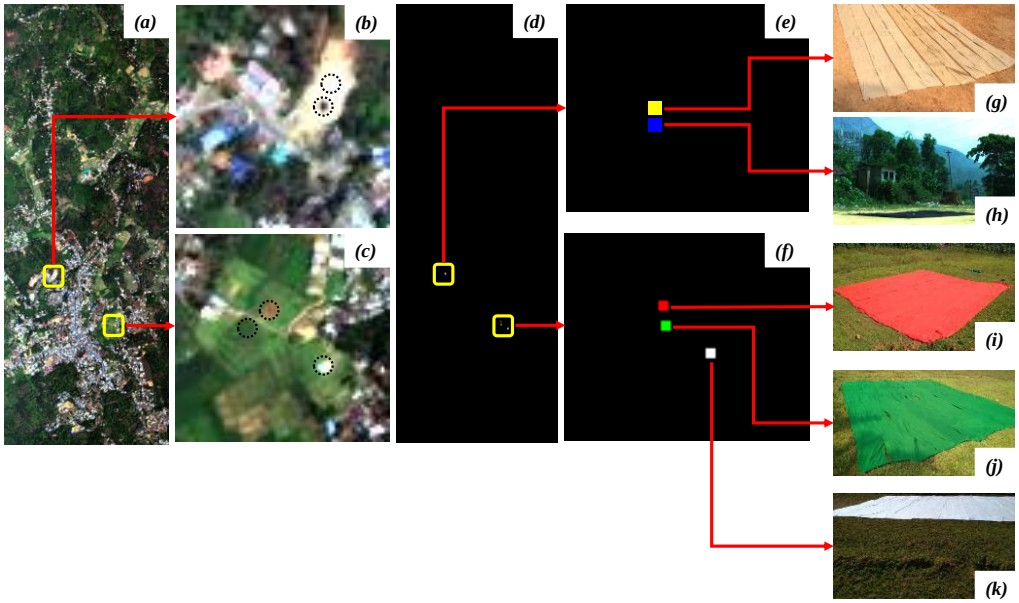

Figure 4.2: (a) True color composite of the AVIRIS-NG hyperspectral imagery with the locations of the artificial targets earmarked; (b) location of targets—N3Y and N4B; (c) location of targets—C1W, N1G, and N2R; (d) ground truth map, and (e–f) enlarged view of the ground truth map for different targets. Field photographs (g–k) showing the artificial targets placed in the study area for imagery acquisition.

4.2.2 Data pre-processing

4.2.2.1 Reference Spectral Data Sources and Pre-Processing

On March 20, 2018, we acquired multi-platform remote sensing data: ground-based terrestrial hyperspectral imager (THI), airborne hyperspectral imager (AVIRIS-NG) and the space-borne multispectral sensor (Sentinel-2). The THI is a push-broom hyperspectral imager (Headwall Photonics Inc., USA) mounted on a movable tripod-kind of the platform. The THI acquires hyperspectral imagery in the VNIR region (40–1000 nm) at about 1nm spectral resolution. In the present setup, a nominal spatial resolution of 1cm further approximated to 20 cm across the targeted area was acquired in a nadir to oblique view. The AVIRIS-NG hyperspectral sensor was operated to

acquire imagery with 4 m spatial resolution and 5nm spectral resolution in the 400–2500 nm spectral range. The airborne hyperspectral data acquisition was part of the NASA and ISRO research collaboration for the HYPSIRI hyperspectral satellite (Bhattacharya et al., 2019). The satellite imagery was acquired about one hour before the acquisition of airborne hyperspectral imagery. Apart from the spectral imagery, we collected point-based in-situ hyperspectral reflectance measurements using a field spectroradiometer (Spectra Vista Corporation, HR-1024i, USA) on the target materials as per the standard procedures (*Field Spectroscopy Guide with SVC I-Series Spectroradiometers,* 2010). The in-situ measurements are considered pure spectral signatures of the target materials, free of atmosphere, and target–surface–neighborhood interactions. Plots of in-situ reference spectral signatures of the target materials are shown in Figure 4.3. There are two sources of ground-based target reference spectra, ground-based hyperspectral imagery (THI) (reference in-situ pixels), and the point-based in-situ spectral reflectance from spectroradiometer. Since the THI collects hyperspectral imagery at a finer spatial resolution, we generated the reference target spectra by sampling target pixels corresponding to different places on the target materials. As the THI imager is sensitive to sensor noise beyond 900 nm, we used the THI data acquired in the spectral range 400 nm to 900 nm. After the initial pre-processing, which included the calibration using the concurrent measurements acquired on white reference panels, all the spectral data were convolved and resampled using the sensor response function (SRF) of the respective sensor for analysis across the datasets.

4.2.2.2 Pre-Processing of Airborne and Spaceborne Imagery

The airborne AVIRIS-NG hyperspectral imagery was corrected for atmospheric distortions using the radiative transfer based Fast Line-of-sight Atmospheric Analysis of Spectral Hypercubes (FLAASH) model (Adler-Golden et al., 1998) and removed the noisy and uncalibrated spectral bands between 1348–1443 nm, 1804–1954 nm, 2485–2500 nm thus resulting in effective imagery with 370 spectral bands. The Sentinel-2 satellite acquires multispectral imagery at different spatial resolutions, 10 m, 20 m, and 60 m. We used the imagery acquired at 10 m and 20 m resolution corresponding to blue (490 nm), green (560 nm), red (665 nm), NIR (842 nm), and vegetation red edge (705

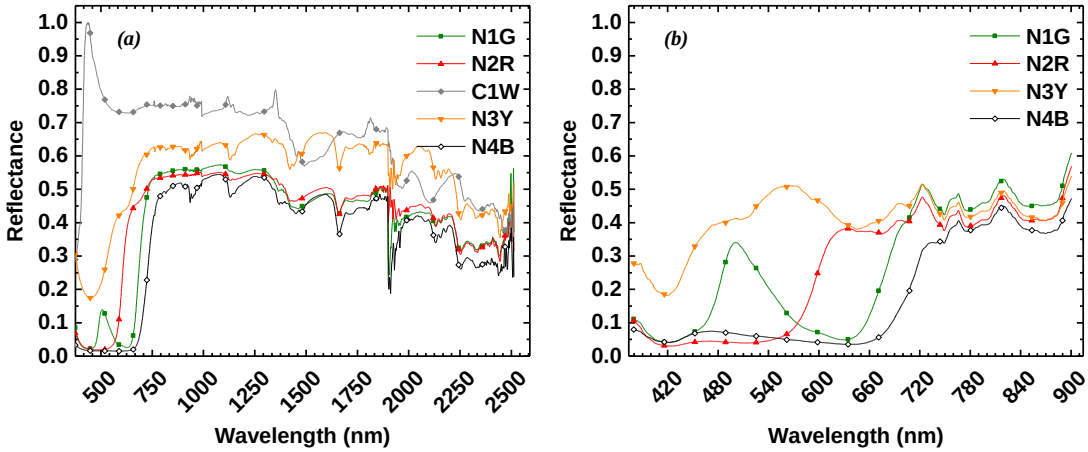

Figure 4.3: Reference spectral signatures of the artificial target materials acquired from (a) in-situ point, and (b) in-situ pixel reflectance measurements.

nm, 740 nm, 783 nm, 865 nm), SWIR (1610 nm, 2190 nm) bands of the Sentinel-2 product respectively centered at the given wavelengths. Generating a vertically conforming surface reflectance data, we corrected the Sentinel-2 imagery for atmospheric distortions using the same model and sensor-surface hyper-parameters used for airborne imagery. The imagery acquired at 20 m spatial resolution was resampled to 10m resolution to conform to other imagery datasets.

4.2.3 Experimental Implementation of Target Detection

An outline of the methodological process flow adopted for the study is shown in Figure 4.4. The ground position of the targets was recorded using a GPS device. Since the targets used in the experiments were considerably large, we designated the target footprint for the airborne imagery as a 16-pixel region of interest (ROI) and a 4-pixel ROI for space-borne imagery as suggested in Manolakis et al. (2003). It must be noted that, due to different sensor resolutions (4 m and 10 m for airborne and space-borne sensor respectively) and imaging geometry, target ROI for airborne imagery contains both full pixel as well as sub-pixel targets, while, target ROI for space-borne imagery contains predominantly sub-pixel targets. Since part of our aim was to evaluate the target detection possibility from multiple platforms, the input signal sources for the detector algorithms were collected from various sensors, as shown in Figure 4.4. We visualize three different scenarios: (i) the use of ground-based target spectra for

detection from airborne and space-borne imagery, (ii) the use of ground-based hyperspectral imager target spectra for detection from airborne and space-borne imagery, and (iii) the use of airborne based target spectra for detection from space-borne imagery which can represent the essence of target detection problem from multiple civil and defense application perspectives.

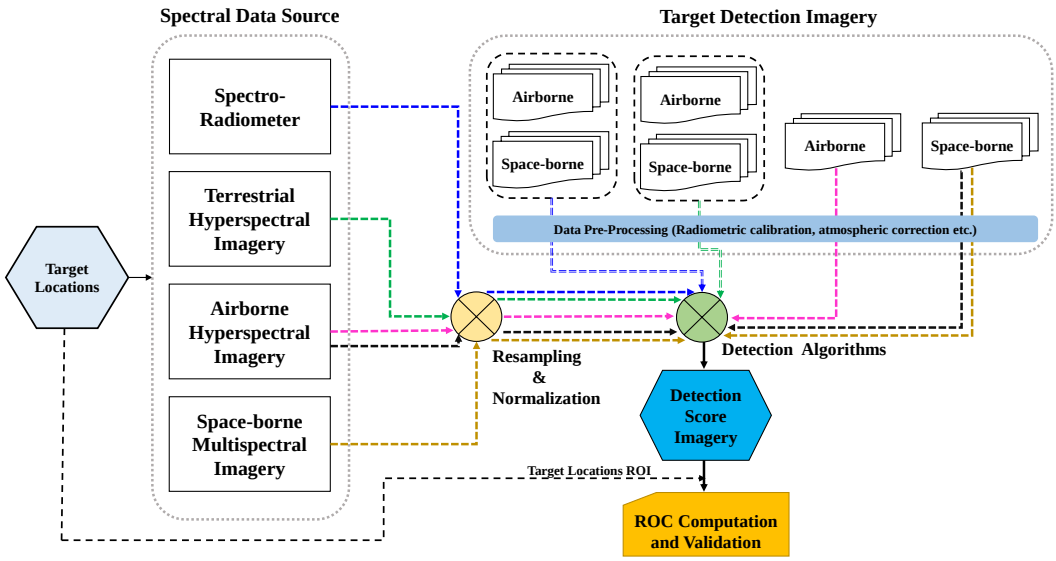

Figure 4.4: Methodological framework adopted for the target detection in multi-platform remote sensing imagery.

4.2.3.1 Target Detection Algorithms

Apart from the target's optical-spectral features and environmental settings, the target detection problem has two other primary perspectives—appropriate spectral imagery and detection algorithms. Given the applicable nature of spectral imagery, target recognition and identification are substantially controlled by the nature of algorithms used for target detection. While the development of advanced target detection algorithms is not within the purview of this research work, it would be valuable to analyze the variations of target detections as a function of the detection algorithm. We, therefore, studied the target detection in the datasets with popular detection algorithms available in the literature, evaluating the quality and sensitivity of the target detections based on the algorithms used.

The taxonomy of detection algorithms depends on various factors such as target-pixel occupancy (full pixel vs. sub-pixel target), considerations for spectral variability (either for target or background), and modeling the combination of pixel and sub-pixel targets (Manolakis et al., 2016). Several full and sub-pixel target detection algorithms such as SAM, MF, CEM, ACE, OSP, and TCIMF were implemented for the detection of targets in this experiment. The SAM, MF, ACE, and CEM are spectral detectors and hence do not require any prior knowledge of the background. However, OSP and TCIMF require prior scene background characterization. Typically, this is approached heuristically estimating the number of distinct background materials or endmembers. The number of distinct background materials represents the complexity of the scene and hence is a scene dependent parameter. We used the SMACC algorithm (Gruninger et al., 2004) for the background endmembers estimation. The detection performance of the OSP and TCIMF was evaluated for three different numbers (5, 10, and 15 endmembers) of background endmembers. Detailed discussion on the mathematical formulation of the target detectors is provided in the Section 2.2.

4.2.4 Validation, and Quantitative Spectral Analysis

The detection results from the different detection algorithms were compared against the ground truth map prepared for each case. Graph-based measures have been increasingly used for quantifying accuracy in various pattern recognition applications, especially in the cases of skewed class distributions (Fawcett, 2006). By the rarity of occurrence, target detection is an approximation of skewed class distribution (Krawczyk, 2016). We adopted the used ROC graphical measure for accuracy assessment. Based on the verified labels of the detections, ROC curves were drawn between the probability of false alarm (P_{FA}) and the probability of detection (P_D) expressed as:

$$\begin{aligned} P_D &= \frac{\text{Number of correctly identified target pixels}}{\text{Total number of actual target pixels}} \\ P_{FA} &= \frac{\text{Number of pixels identified as false targets}}{\text{Total number of non} - \text{target pixels}}. \end{aligned} \tag{4.1}$$

The possibility and quality of target detections from multi-platform remote sensing imagery depend upon the existence and quantification of inherent spectral matching between target spectra from different platforms. Quantitative analysis of the spectral matching between the various combinations of reference target spectra and imaging platform deciphers the basis of target detections by detection algorithms. For each of the possible scenarios considered, we applied multiple spectral matching metrics: spectral angle (SA) (Kruse et al., 1993a), spectral information divergence (SID) (Chang, 2000a), and spectral gradient angle (SGA) (Robila & Gershman, 2005) on the spectral data extracted from the ground reference (ground hyperspectral imagery, and point-based spectral measurements) and the airborne and space-borne imagery. We present a brief description of the spectral matching metrics considered.

Consider any two n-dimensional vectors $\mathrm{P} = \{p_1, p_2, p_3, p_4 \dots p_\mathrm{n}\}^t$, and $\mathrm{Q} = \{q_1, q_2, q_3, q_4 \dots q_\mathrm{n}\}^t$.

The spectral matching metrics SA, SID, and SGA are defined as:

$$\mathrm{SA\ (P, Q)} = \cos^{-1}\left(\frac{\langle \mathbf{P}, \mathbf{Q} \rangle}{\|\mathbf{P}\|_2 \|\mathbf{Q}\|_2}\right), \tag{4.2}$$

where, $\langle\ \rangle$ denotes the dot product of two vectors and $\|.\|_2$ denotes the Euclidean norm of a vector.

$$\mathrm{SID\ (P, Q)} = D(P\ ||\ Q) + D(Q\ ||\ P)$$
$$= \sum_{i=1}^{n} \left(\frac{p_i}{\sum_{j=1}^{n} p_j} - \frac{q_i}{\sum_{j=1}^{n} q_j}\right)\left(\log\left(\frac{p_i}{\sum_{j=1}^{n} p_j}\right) - \log\left(\frac{q_i}{\sum_{j=1}^{n} q_j}\right)\right) \tag{4.3}$$

where $D\ (P \parallel Q)$ and $D(Q \parallel P)$are called the relative entropy of Q with respect to P and relative entropy of P with respect to Q, respectively.

SID is a probabilistic approach to measure the spectral similarity between two spectra. Each pixel is represented in the probabilistic space defined by their spectral histogram. Thus, the SID score is an indication of the behavioral difference in the probability distribution function of any two pixels. A score close to zero from the SA and SID indicates that the spectra are similar (Chang, 2003; Van der Meer, 2006). The spectral gradient angle can be expressed as:

$$\begin{aligned} \mathrm{SGA}\,(\mathrm{P},\mathrm{Q}) &= \mathrm{SA}\left(abs\big(\mathrm{SG}(\mathrm{P})\big), abs\big(\mathrm{SG}(\mathrm{Q})\big)\right) \text{ and} \\ \mathrm{SG}\,(\mathrm{P}) &= (p_2 - p_1, p_3 - p_2, \ldots, p_n - p_{n-1}), \end{aligned} \tag{4.4}$$

where $\mathrm{SG}(\,.\,)$ is the spectral gradient of a given vector. The SGA computes the change of slope of the pixel vectors and is thus invariant to illumination condition similar to SA; a lower value of SGA suggests closer matching of the spectra compared.

4.3 Results

Our experimental research set up was aimed at examining three critical perspectives in remote sensing-based target detection: (i) platform—the probability and consistency of target detection vis-à-vis platforms, (ii) reference target spectra—the relevance and level of acquiescence of cross-platform target reference spectra, and (iii) detection algorithm—the variation of detection due to detection algorithms. The first component was approached by quantifying the magnitude and patterns of variation of P_D with the three levels of platforms considered. The second component was addressed by comparing the levels of target detection rates between two sets of reference target spectra generated: from the same dataset and the cross-platform dataset. The third perspective, the influence of algorithms on the detection results, was assessed by measuring the change in patterns and detection rates from the different detection algorithms considered. As different detection algorithms characterize scene background at varying levels of land cover composition, the sensitivity of detection rates relative to the scene complexity (characterized by the number of endmembers) and the contrast between the target and its neighborhood was also carried out. The spectral analysis assessing the matching or lack of it in the multi-platform target spectra, quantitative comparison of the ground-based target reference spectra with the image-based target spectra, was also performed using three different spectral matching metrics. We present the results organized based on the source of the target reference spectra. We considered target detection successful at detection probabilities of (P_D) of 100%, and 75%, recognizing the fact that the datasets encompass a wider range of

spectral variability. The detection and false alarm rates from different combinations of the platforms and algorithms are described in detail.

4.3.1 In-Situ Measurements as Reference Target Spectra

In this section, we present the results of target detection experiments when the in-situ reflectance measurements were used as the reference target spectra for target detection in airborne and space-borne imagery.

4.3.1.1 Target Detection in Airborne Hyperspectral Imagery

Results of the target detection in airborne hyperspectral imagery are summarized in Figure 4.5 and the corresponding representative detection score image in Figure 4.6. The detection score image is a raster image which contains a scalar value also known as score, corresponding to each pixel. The value represents the likelihood of the pixel for being flagged as target/non-target. Results indicate successful target detections for the different types of target materials, meeting the threshold detection rate at 100% threshold of P_D for some materials. Overall, the detection rate is consistent across the types of materials. Except for SAM, all the detectors produced an average detection rate of 75% at nearly zero false alarm rate.

Detection rate vs. scene complexity: In contrast to the generally acceptable levels of detection rates for a broader approximation of scene-background, detection rates are substantially variable by the scene complexity, and target–neighborhood contrast. The detection rates are consistent and satisfy the lower threshold when the scene complexity was represented by five endmembers. When the scene complexity increased to represent 15 endmembers, the false alarm rate increased steeply, indicating substantial performance degradation in some detection algorithms. The rise in the false alarm rate was not uniform and varied by different classes of detection algorithms.

Identical materials vs. background contrast: It is expected that targets of identical material, even if of a different color or background, are recognizable in a hyperspectral imagery. Results indicate that the possibility of an identical base material

target in a different color or on different background introduces substantial ambiguity in the quality of target detection. For example, at P_D of 75%, the P_{FA} from the CEM method is 0.0685, and $1.02\ \text{X}10^{-4}$ respectively for the targets N2R and N1G placed on the same background. Similarly, the P_{FA} for the ACE method is 0.017, and $2\ \times 10^{-6}$ respectively for the N4B and N1G targets placed on different backgrounds. During the detection of the N2R, the N1G was also flagged as a potential target and vice-versa (see Figure 4.6(d, e)). The failure of the suppression of targets of identical color but of physically different materials is one of the challenging problems encountered for spectrally close materials. Apparently, by the absolute value, P_{FA} is relatively low for considering the relevant target detections as ambiguous. However, when the corresponding P_{FA} estimates are converted into actual pixel count, the certainty of detection seems to be far from the ideal case. For instance, for the N1G target, the CEM flags a false alarm of ~70 pixels distributed across the imagery. If the confidence of the detection rate is increased to 100% (i.e., P_D = 100%), almost all the detectors show substantially lower detection results in terms of completeness of the targets. Overall, results suggest that, apart from the target–background interaction, the spectral contrast of targets play a substantial role in the detectability.

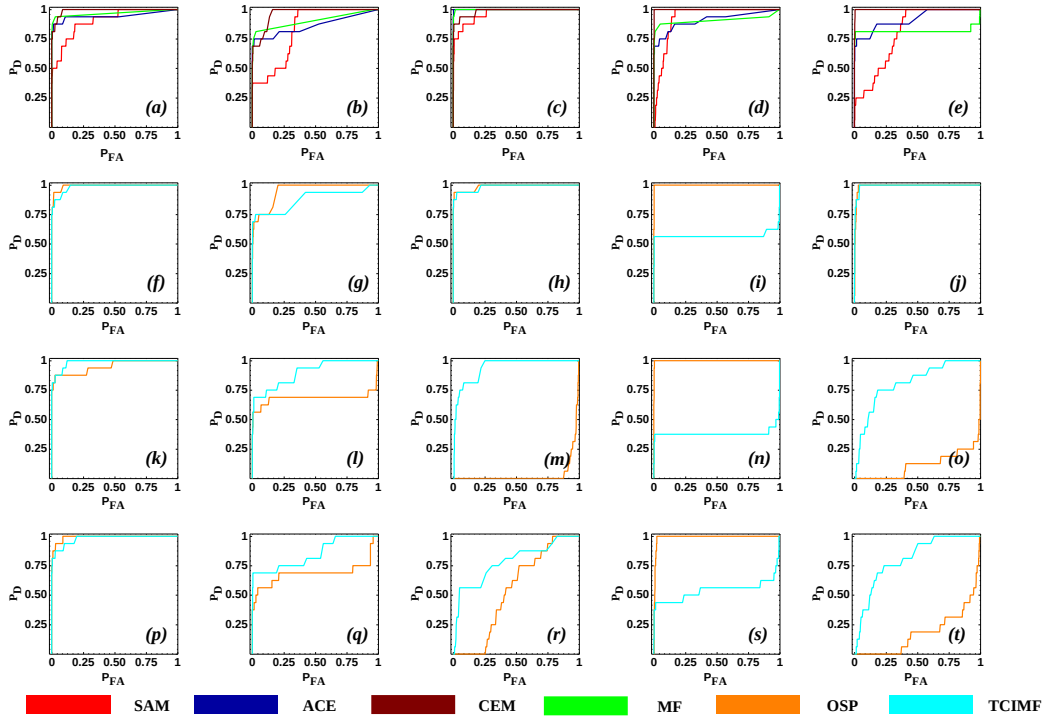

Figure 4.5: Target detection performance comparison in airborne imagery for the in-situ target reference spectra. ROC for the detection from spectral angle SAM, ACE, CEM, and MF for the (a) N1G, (b) N2R, (c) C1W, (d) N3Y, and (e) N4B targets. ROC curves for the detection from OSP and TCIMF for the N1G, N2R, C1W, N3Y, and N4B targets for (f–j) 5, (k–o) 10, and (p–t) 15 background materials.

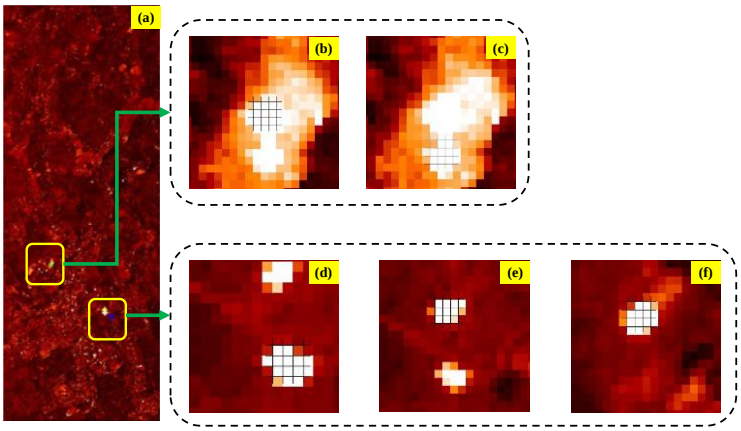

Figure 4.6: Target detection score image from (a) airborne imagery using in-situ reference target spectra, and the enlarged detection score footprint for (b) N3Y, (c) N4B, (d) N1G, (e) N2R, and (f) C1W target (In all the target detection score images, a brighter pixel indicates a higher target detection score and thus a higher probability for it to be declared as a target).

4.3.1.2 Target Detection in Spaceborne Remote Sensing Imagery

Results of the target detection in airborne hyperspectral imagery are summarized in Figure 4.7 and the corresponding representative detection score image in Figure 4.8. Due to coarse spectral and spatial resolutions and the substantially higher level of atmospheric influences, target detection in space-borne multispectral imagery is challenging compared to airborne hyperspectral imagery. Use of the in-situ reflectance measurements, considered a pure form of reference spectra, as target reference spectra, elicited no quantifiable spectral discrimination of target pixels in the satellite imagery. As evident from Figure 4.8, the detection scores and surrounding pixels are similar for targets N1G, N2R resulting in higher false alarm rates across all the algorithms (Figure 4.7). While the detection results included the pixels of targets, the apparent gross overestimation indicates the detection results to be unreliable. The detection algorithms either fail to detect or the respective false alarm rates are higher due to the relatively lesser number of estimated background endmembers. However, when the probability of detection was set at 75% and the scene complexity increased by representing with a large number of endmembers (10 or more), the sub-pixel target detection algorithms (e.g., CEM, TCIMF, Figure 4.7(p)) produced stable detection results. It is interesting to note that unlike target detection in airborne imagery, there was no change in the false alarm rate when the probability of detection was increased from 75% to 100%.

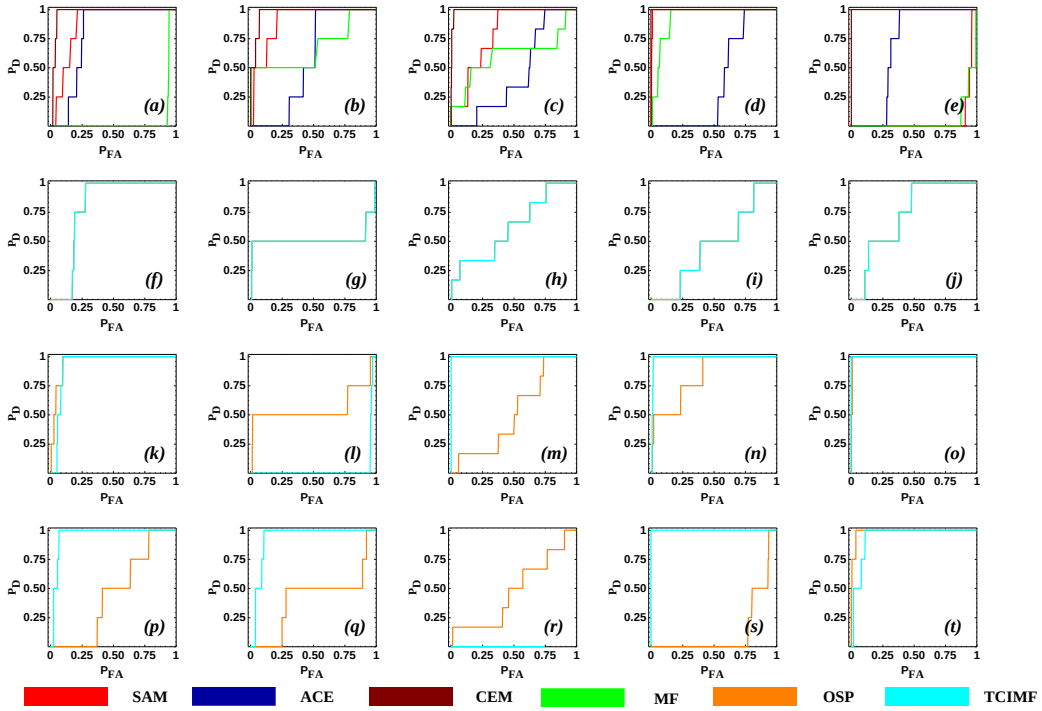

Figure 4.7: Target detection performance comparison from space-borne imagery for the in-situ target reference spectra. ROC curves for the detection from SAM, ACE, CEM, and MF for the (a) N1G, (b) N2R, (c) N3Y, (d) C1W, and (e) N4B targets. ROC curves for the subspace-based detector OSP and TCIMF for the N1G, N2R, N3Y, C1W, and N4B targets for (f–j) 5, (k–o) 10, and (p–t) 15 endmember/background materials.

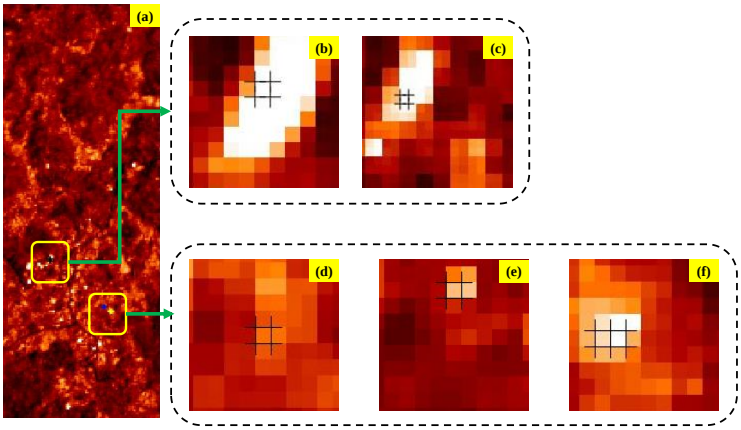

Figure 4.8: Target detection score image (a) from space-borne imagery using in-situ target reference spectrum and the enlarged detection score footprint for (b) N3Y, (c) N4B, (d) N1G, (e) N2R, and (f) C1W targets.

4.3.2 Ground-Based Hyperspectral Imagery (THI) as Reference Target Spectra

In-situ or laboratory-based spectral reflectance measurements of materials are considered to be the pure forms of the spectral signatures. While the relevance of the purity of spectral signature seems standing, theoretically, on a sound basis, the results presented in this section indicate that a pixel-based reference spectrum is a viable substitute to the in-situ spectra.

4.3.2.1 Target Detection in Airborne Hyperspectral Imagery

The results of target detection in airborne hyperspectral imagery and a representative detection score images are shown in Figures 4.9 and 4.10. Results indicate the possibility of target detection, suggesting the existence of a spatially distinct spectral matching between the ground hyperspectral imagery and the airborne hyperspectral imagery. As shown in Figure 4.10(e), in the case of the THI reference spectrum, suppression of similar but different targets (NIG suppressed when N2R was detected and vice-versa) is superior compared to the results from in-situ reference spectra (see Figure 4.6). However, the false alarm rate is higher compared to the extent and spatial distribution of the target pixels in the airborne hyperspectral imagery. This may be due to the limited in the spectral coverage (400–1000 nm), compared to the full optical spectrum of the airborne hyperspectral imagery (400–2500 nm). As the targets considered are inorganic artificial materials, spectral reflectance in the shortwave infrared region (1000–2500 nm) may provide characteristic spectral discrimination. Compared to the case of using in-situ reference target spectra, spectral matching based detection algorithms showed relatively better detection rate, consistent across the targets. In addition, contextually camouflaged targets were also detected, as indicated by the relatively higher scores of P_D and negligible scores of P_{FA}.

The detection rate of the targets by background-characterization based algorithms is ambiguous. In-scene estimation of background material spectra was poor. For e.g., for the N3Y target, detection by TCIMF improved when the estimated number of background material increased from 5 to 15 but degraded at the same time for the

N2R target. As observed, if the P_D rate is required to be high (P_D = 100%), detection rate from all the detectors is unacceptable for any practical system.

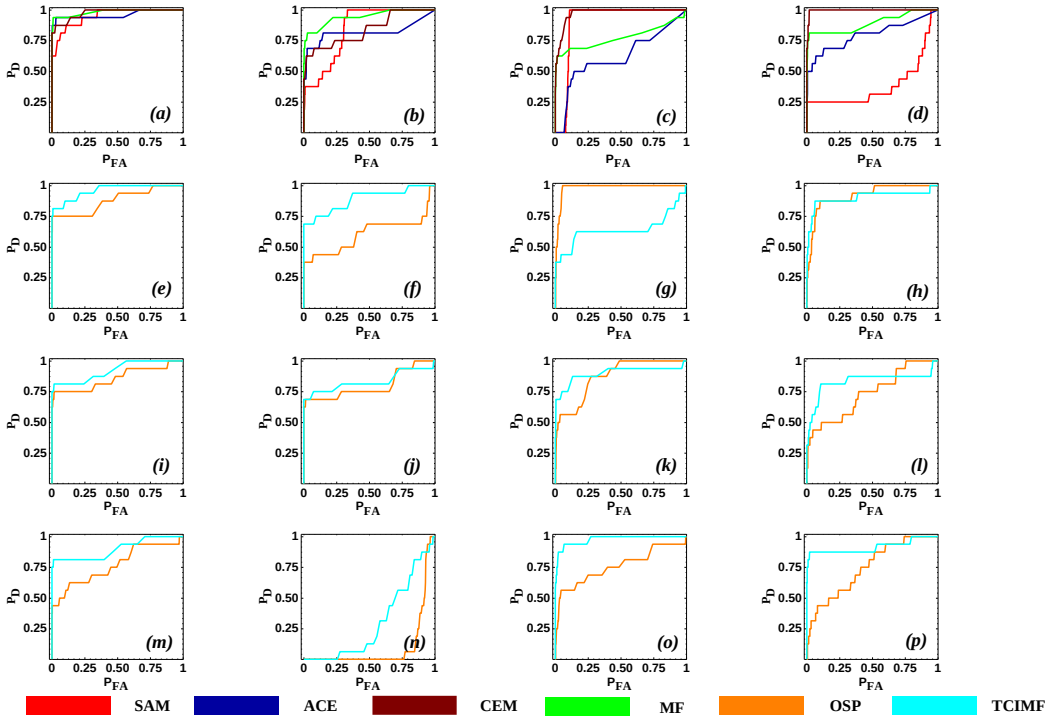

Figure 4.9. Target detection performance comparison in airborne imagery for the terrestrial hyperspectral imager (THI) target reference spectra. ROC curves for the detection from SAM, ACE, CEM, and MF for the (a) N1G, (b) N2R, (c) N3Y, and (d) N4B targets. ROC curves for the subspace-based detector OSP and TCIMF for the N1G, N2R, N3Y, and N4B targets for (e–h) 5, (i-l) 10, and (m–p) 15 endmember/background materials

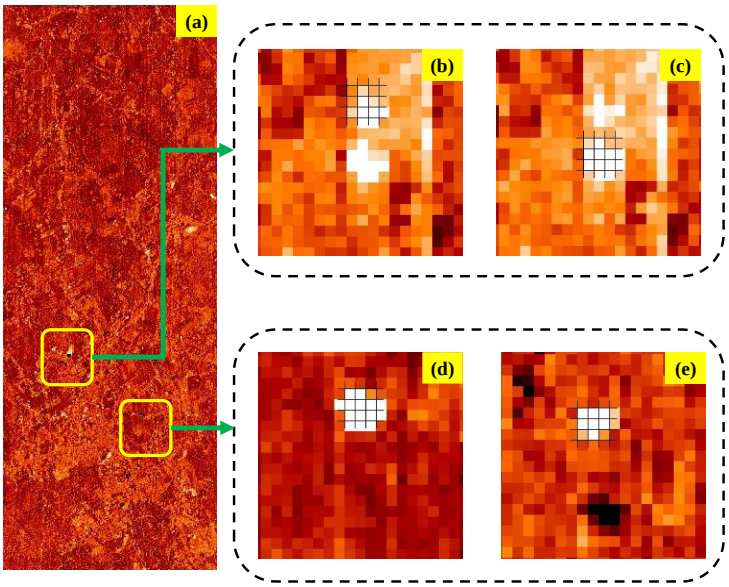

Figure 4.10: Target detection score image from (a) airborne imagery using THI target reference spectrum and the enlarged detection score footprint for (b) N3Y, (c) N4B, (d) N1G, and (e) N2Rtarget.

4.3.2.2 Target Detection in Spaceborne Remote Sensing Imagery

With the consideration of THI pixel spectra as target reference spectra, the results of target detection in space-borne multispectral imagery and a representative detection score image in Figures 4.11 and 4.12, respectively. Similar to the results obtained with the point-based in-situ target reference spectra, the target detection in space-borne multispectral imagery is ambiguous across the types of targets. A couple of detection algorithms (e.g., CEM, OSP) produced detection scores meeting the threshold limit. However, the corresponding disproportionately high false alarm rate indicates that the detection is by chance.

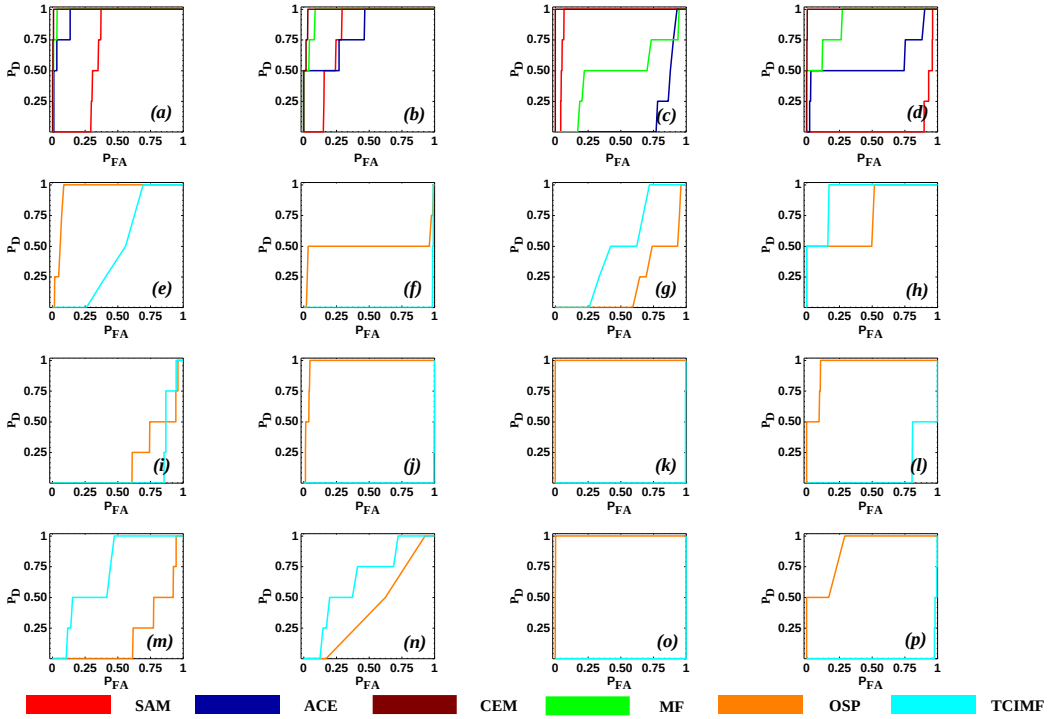

Figure 4.11: Target detection performance comparison in space-borne imagery for the THI target reference spectra. ROC curves for the detection from SAM, ACE, CEM, and MF for the (a) N1G, (b) N2R, (c) N3Y, and (d) N4B targets. ROC curves for the subspace-based detector OSP and TCIMF for the N1G, N2R, N3Y, C1W, and N4B targets for (e–h) 5, (i–l) 10, and (m–p) 15 endmember/background materials.

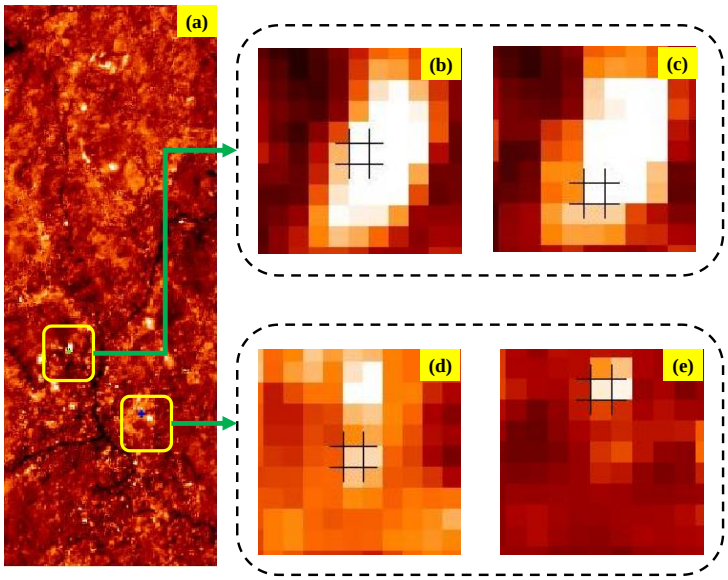

Figure 4.12: Target detection score image from (a) space-borne imagery using THI target reference spectra and the enlarged detection score footprint for (b) N3Y, (c) N4B, (d) N1G, and (e) N2R target.

4.3.3 Target Reference Spectra from the Airborne Hyperspectral Imagery

4.3.3.1 Target Detection in Airborne Hyperspectral Imagery

Target detection experiments were carried out on the airborne hyperspectral imagery and space-borne multispectral imagery using considering pixel-based spectra extracted from the airborne hyperspectral imagery as target reference spectra. Figure 4.13 shows the target detection scores for the different types of targets in the airborne hyperspectral imagery. Targets were detected with detection scores exceeding 90% with negligible false alarm rates. The accurate detection of the lowest false alarm rates across the target types and detection algorithms indicates the possibility of consistent target detections in airborne hyperspectral imagery. However, the relatively higher rate of false positives for the contextually camouflaged targets suggests the dominance of local background–target interactions (as evident in Figure 4.14) on the radiance measurements. The limitations of the present suite of detection algorithms in discerning complex background–target interactions might also be a reason higher false alarm rate for detecting contextually camouflaged targets.

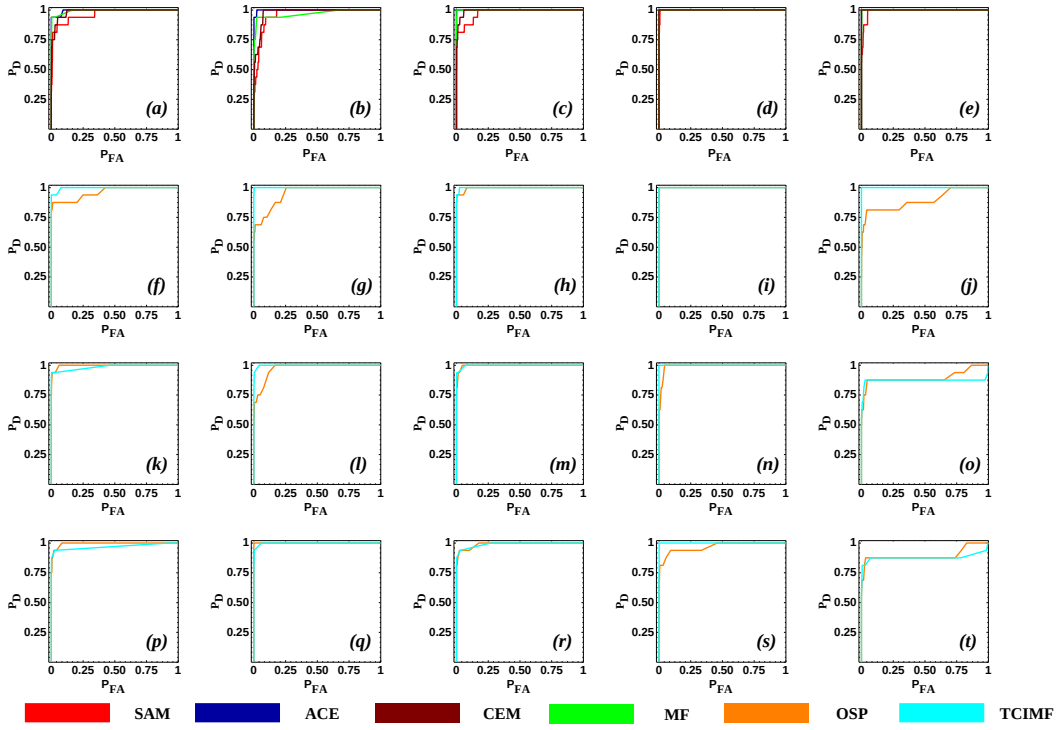

Figure 4.13: Target detection performance comparison in airborne imagery for the airborne target reference spectra. ROC curves for the detection from SAM, ACE, CEM, and MF for the (a) N1G, (b) N2R, (c) N3Y, (d) C1W, and (e) N4B targets. ROC curves for the subspace-based detector OSP and TCIMF for the N1G, N2R, N3Y, C1W, and N4B targets for (f-j) 5, (k-o) 10, and (p-t) 15 endmember/background materials.

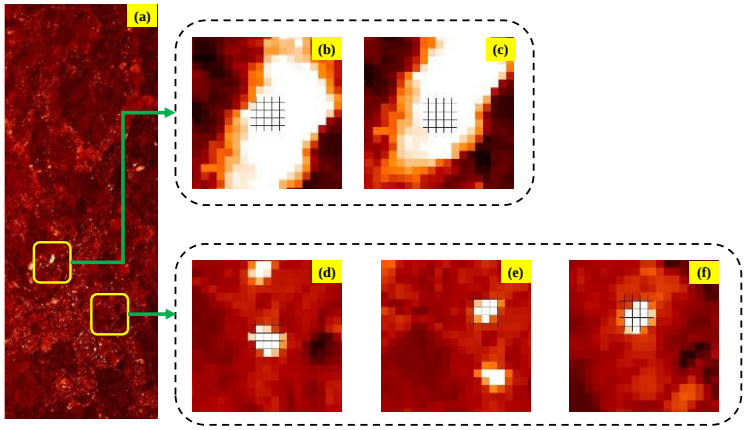

Figure 4.14: Target detection score image from (a) airborne imagery using airborne target reference spectrum and the enlarged detection score footprint for (b) N3Y, (c) N4B, (d) N1G, (e) N2R, and (f) C1W target.

4.3.3.2 Target Detection in Spaceborne Multispectral Imagery

The target reference spectra extracted from the airborne hyperspectral imagery were transferred and convolved to space-borne level for target detection in the space-borne multispectral imagery. The detection results are summarized in Figure 4.15 and a representative detection score image in Figure 4.16. Most of the detection results are ambiguous with a higher rate of false alarms. However, when compared to the detection results from using in-situ target reference spectra, detection in satellite imagery increased substantially across the targets and algorithms. For instance, in the case of MF and ACE, the rate of false positives at P_D of 75% is very low (10^{-2} to 10^{-5}). Further, contrary to the influence of background types observed in the airborne imagery, target detection in space-borne imagery seems not sensitive to the local background. For example, for the two different targets (e.g., N1G and N2R) placed against the same background, the difference in false alarm rate is relatively low. However, this sensitivity is not stable across the detection algorithms. The subspace detectors continued to yield ambiguous detection results for most of the targets. The differences in the spatial and spectral resolutions, coupled with acquisition geometry and enhanced atmospheric effects may have led to the relatively weaker target localization in the space-borne imagery.

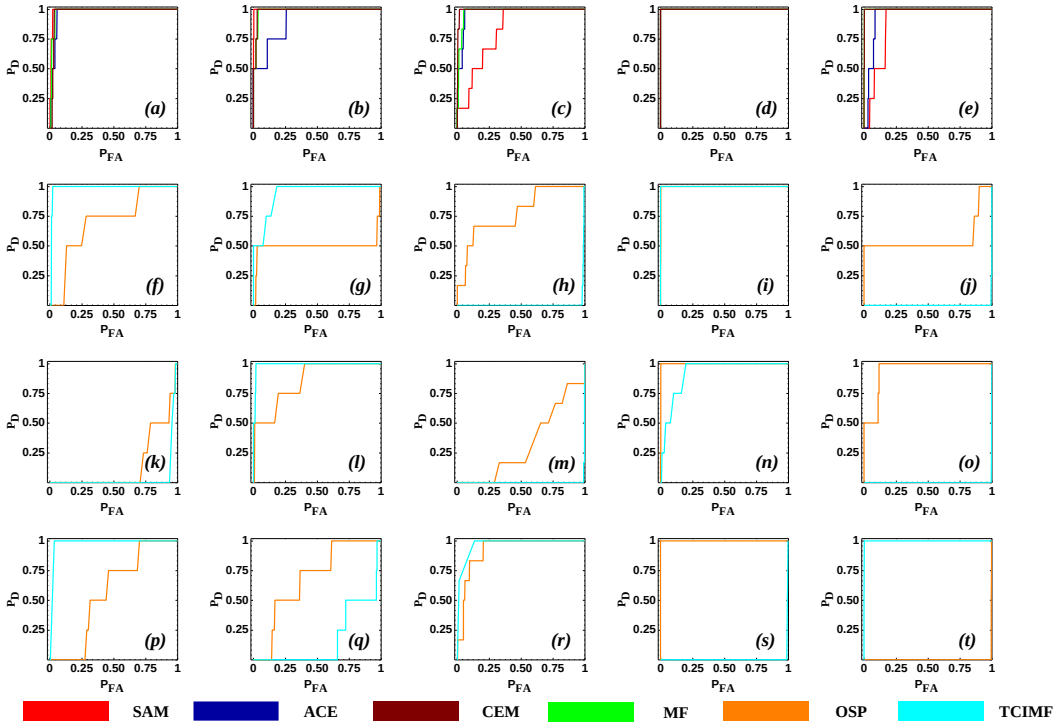

Figure 4.15: Target detection performance comparison in space-borne imagery for the airborne target reference spectra. ROC curves for the detection from SAM, ACE, CEM, and MF for the (a) N1G, (b) N2R, (c) N3Y, (d) C1W, and (e) N4B targets. ROC curves for the subspace-based detector OSP and TCIMF for the N1G, N2R, N3Y, C1W, and N4B targets for (f–j) 5, (k–o) 10, and (p–t) 15 endmember/background materials.

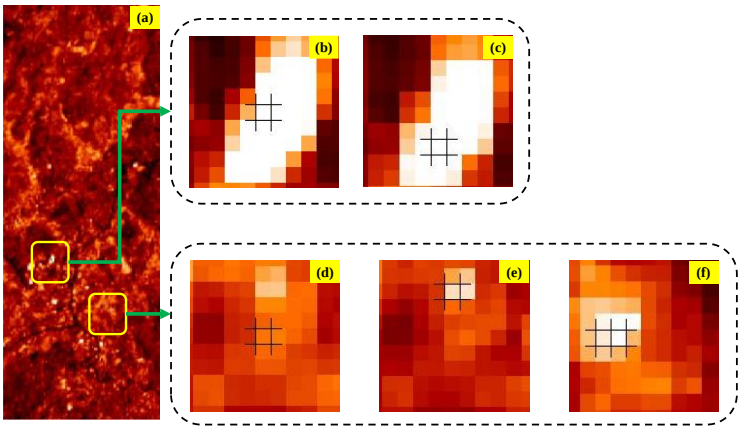

Figure 4.16: Target detection score image from (a) space-borne imagery using airborne target reference spectrum and the enlarged detection score footprint for (b) N3Y, (c) N4B, (d) N1G, (e) N2R, and (f) C1W target.

4.3.4 Target Reference Spectra from the Spaceborne Multispectral Imagery

The results of target detection in space-borne imagery obtained from using in-scene target reference spectra are shown in Figure 4.17 and a detection score image for the best case detection in Figure 4.18. Results indicate improved detection scores and low false alarms compared to the detection performance obtained from using the target reference spectra from in-situ spectral measurements or airborne hyperspectral pixel spectra. The performance of all the statistical detectors is similar, and detection rates meet the 75% level of probability. However, detection performance from the subspace target detectors is random and unreliable. The overall detection results show substantial viability in the detection of the engineered targets using the in-scene multispectral target spectra from the space-borne imagery.

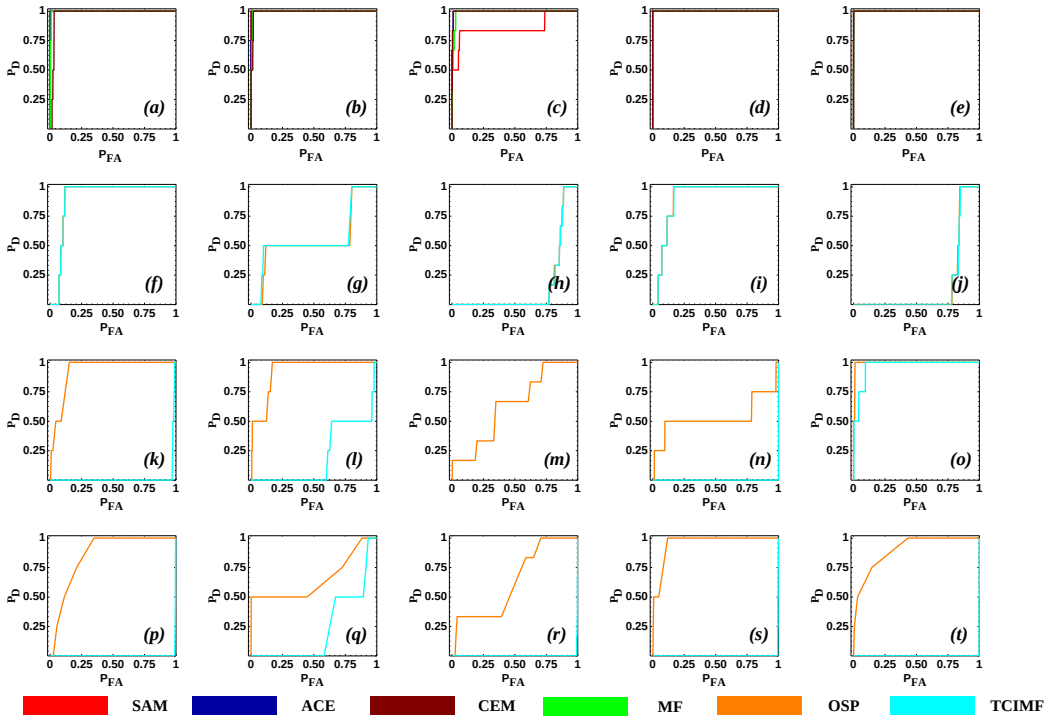

Figure 4.17: Target detection performance comparison in space-borne imagery for the airborne target reference spectra. ROC curves for the detection from SAM, ACE, CEM, and MF for the (a) N1G, (b) N2R, (c) N3Y, (d) C1W, and (e) N4B targets. ROC curves for the subspace-based detector OSP and TCIMF for the N1G, N2R, N3Y, C1W, and N4B targets for (f–j) 5, (k–o) 10, and (p–t) 15 endmember/background materials.

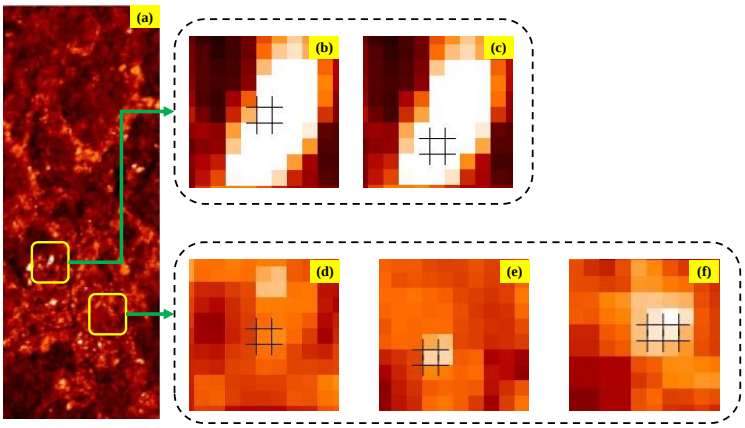

Figure 4.18: Target detection score image from (a) space-borne imagery using space-borne target reference spectrum and the enlarged detection score footprint for (b) N3Y, (c) N4B, (d) N1G, (e) N2R, and (f) C1W target.

4.3.5 Quantitative Spectral Similarity Analysis

Results of the spectral similarity assessment between the possible pairs of ground, airborne, and space-borne target reference spectra are presented in Tables 4.2 through 4.4. For visual comparison, spectral signatures of the targets from imagery and reference sources are shown in Figure 4.19. We found considerable spectral variability in the in-scene target spectra, particularly the case of in-situ reference spectra compared to the airborne image spectra (Figure 4.19 (a–e) (I)). The relatively higher accuracy of target detections observed in the airborne imagery (Section 4.3.1.1) while using the in-situ spectral measurement as reference target spectra can be attributed to the inherent spectral similarity between in situ reference spectra and airborne image spectra (Table 4.2; lower SID and SGA value across all target materials). Further, the score for the in-situ target reference spectra and space-borne target image spectra shows stark dissimilarities across the targets explaining the apparent unsatisfactory detection performance across the algorithms (Section 4.3.1.2). Similarly, the detection performance observed in Section 3.2 conforms to the similarity measure seen in Table 4.3. Comparing the similarity scores from Tables 4.2 and 4.4, we found a close similarity between the airborne reference spectra and space-borne image spectra compared to that of the in-situ to the space-borne image spectra. This matching reflected aptly in the detection performance observed in Section 4.3.3. It may be noted that the similarity measures employed for quantifying spectral matching are designed

mainly for hyperspectral resolution data. Use of these measures for the quantitative spectral matching in multispectral data may not be optimal.

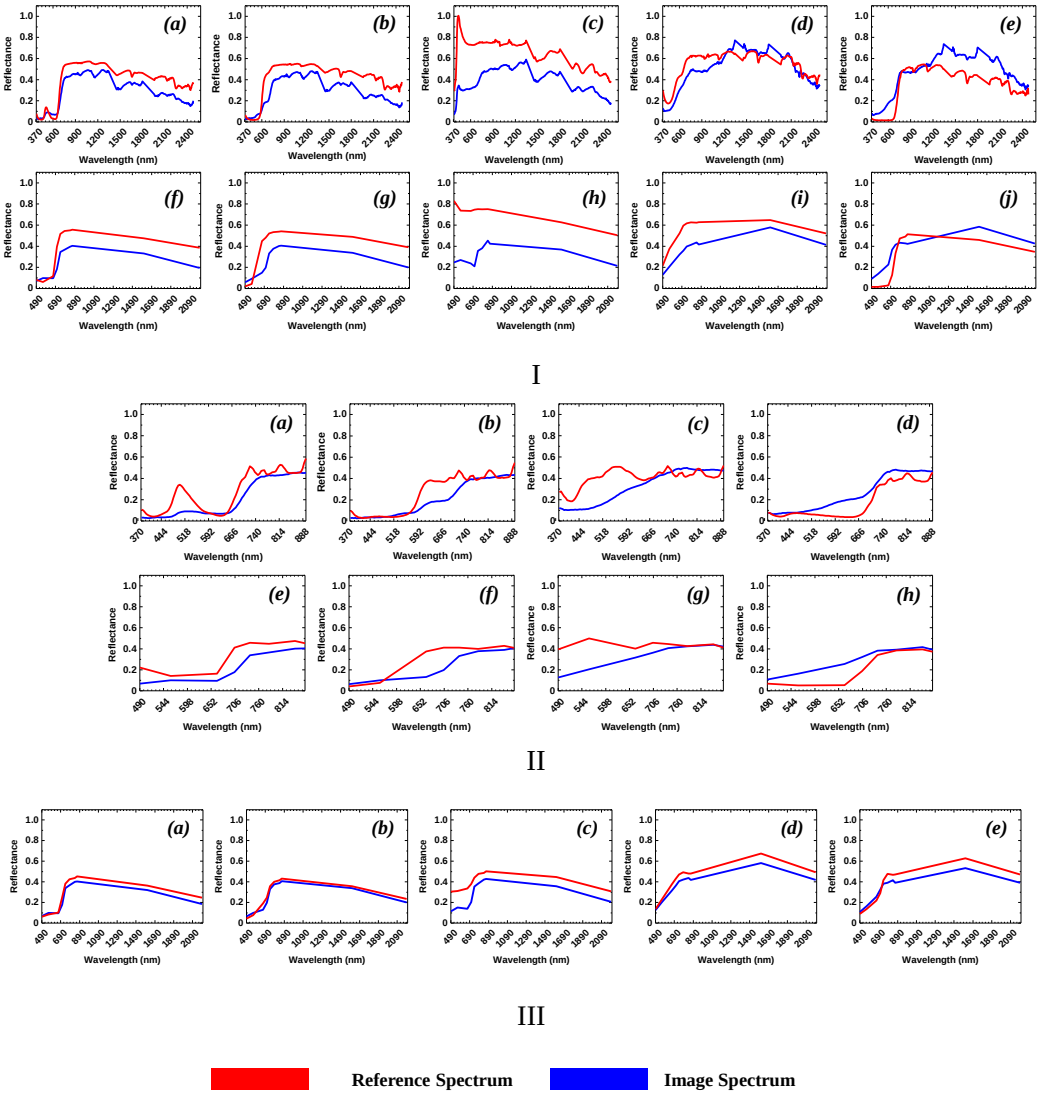

Figure 4.19. Spectral comparison of the reference target spectra with the corresponding image target spectra for: (I) in-situ measurements of (a,f) N1G, (b,g) N2R, (c,h) C1W, (d,i) N3Y, and (e,j) N4B compared to airborne and space-borne image spectra respectively; (II) THI measurements of (a,e) N1G, (b,f) N2R,(c,g) N3Y, and (d,h) N4B compared to airborne and space-borne image spectra respectively; and (III) airborne measurements of (a) N1G, (b) N2R, (c) C1W, (d) N3Y, and (e) N4B compared to space-borne image spectra.

Table 4.2: Spectral similarity measures between the point-based in-situ target reference spectra and the corresponding airborne, and space-borne target image spectra (spectral angle (SA) is measured in degrees and spectral gradient angle (SGA) in radians) Values in bold are statistically significant.

	In-Situ Reference Spectra vs. Airborne Image Spectra					In-Situ Reference Spectra vs. Satellite Imagery Spectra				
Metric	N1G	N2R	C1W	N3Y	N4B	N1G	N2R	C1W	N3Y	N4B
SA	7.623	10.386	12.273	8.503	11.617	8.338	14.111	15.246	8.008	19.219
SID	0.031	0.050	0.050	0.028	0.105	0.045	0.126	0.074	0.019	0.306
SGA	0.650	0.839	0.523	0.678	0.744	0.688	1.040	0.904	0.667	0.887

Table 4.3: Spectral similarity between the THI target reference spectra and the corresponding airborne, and space-borne target image spectra (SA is measured in degrees and SGA in radians). Values in bold are statistically significant.

	THI Reference Spectra vs. Airborne Image Spectra				THI Reference Spectra vs. Satellite Imagery Spectra			
Metric	N1G	N2R	N3Y	N4B	N1G	N2R	N3Y	N4B
SA	15.444	15.762	20.916	14.268	13.459	17.567	18.181	16.290
SID	0.143	0.101	0.179	0.172	0.087	0.136	0.134	0.176
SGA	0.775	0.821	0.943	0.754	0.898	1.282	0.288	0.836

Table 4.4: Spectral similarity between the airborne target reference spectra and the space-borne target image spectra (SA is measured in degrees and SGA in radians). Values in bold are statistically significant.

Airborne Reference Spectra vs. Satellite Imagery Spectra					
Metric	N1G	N2R	C1W	N3Y	N4B
SA	4.169	4.431	13.008	1.406	6.045
SID	0.011	0.016	0.073	0.001	0.018
SGA	0.336	0.391	0.378	0.096	0.309

4.4 Discussion

Having the spectral profiling a priori, targeted detection of artificial/engineering materials using remote sensing is emerging as a data paradigm for a host of civil and strategic applications. Among the recent developments in hyperspectral remote sensing, target detection has the potential to deploy on a broader application base. There have been a few seminal efforts on acquiring and making them freely available benchmark airborne hyperspectral datasets which have attempted detecting specific information class/materials of interest. There have also been a few studies on target detection in synthetic or simulated hyperspectral imagery (Goodenough & Brown, 2012).

While these datasets and experiments provide a solid base for classification-oriented exploration, targets and their landscape-neighborhoods in these datasets are set in a relatively controlled environment. They may not represent typical landscapes and target conditions. Apart from that, the criteria used for labeling a pixel detection as 'true' or 'false' has a substantial bearing on the magnitude of detection accuracy. For example, the best accuracy estimates for the case of airborne imagery in this study are equal or slightly lesser compared to the accuracy reported in the state-of-the-art literature (Snyder et al., 2008b; Wang & Xue, 2017). The potential target detection performance in our experiments, considering only from the pixel labelling perspective would be substantially higher than the values presented in this chapter, and the values reported in the literature. From the state-of-the-art in accuracy estimates in target detection, the difference between our potential accuracy and reported accuracy is due to the relatively liberal criterion used for accuracy estimation in the literature. The past studies define a target guard window - representing a neighborhood region at three different levels and proximity to the core 'target pixel' for labeling a detection true or false. The detection of even a single pixel within any of these three levels is considered 100% correct detection of the whole target, which may lead to overestimation of detection performance. Avoiding the possibility of this uncertainty, we used the stringent pixel-for-pixel matching based count of target pixels for computing the performance metrics P_D andP_{FA}.

Furthering the experimental landscapes and the benchmark reference datasets for target detection, the goal of our research is the acquisition and exploration of a multi-platform—ground, airborne, and space-borne remote sensing dataset for target detection of artificial/engineered materials. Our experiments were aimed at assessing the dynamics of target detection in terms of (i) spectral attribute conformity of reference target spectra from the ground to space-borne, (ii) target–background interaction: identical target material on similar, and different backgrounds, and (iii) the relevance of detection algorithms and their functional categorization. We present in the following sub-sections the relevance and importance of the results organized according to the three perspectives mentioned above.

4.4.1 Spectral Conformity of the Reference Target Spectra from Ground to Spaceborne Platform

The continued detections of the engineered material targets in the ground to space-borne imagery, though at different levels of confidence, preserving the location adherence and material-specific identifications indicates the presence of material-specific spectral features. Results from the airborne hyperspectral imagery exhibit successful target detections from both the point-based in-situ and pixel-based THI reference target spectra. However, target detections using the in-situ target reference spectra are valid only for ground and airborne imagery. As evident from Figure 4.7, the target detections in the space-borne imagery drop to that of a random process. Contrasting to this trend, detection results from the pixel-based reference target spectra indicate patterns in the target detection in both the airborne and space-borne imagery. However, point-based in-situ, and the pixel-based THI reference target spectra yield comparable levels of target detections in the airborne hyperspectral imagery. Target detection and the quantitative spectral assessment of the pixel-based THI reference target spectra with the airborne (AVIRIS-NG imagery) and the space-borne (Sentinel-2 imagery) spectra suggests stable spectral conformity of material spectra at the ground, airborne, and space-borne platforms. The pixel-based THI spectral conformity leads to two practical implications: (i) a new source of in-situ reference spectra, and (ii) potential syllogism that impure contextual spectrum is better than the laboratory-grade pure spectrum. Ground-based hyperspectral image acquisitions can replace the

spectroradiometer based in-situ or laboratory spectral measurements. Image-based reference spectra acquisition is particularly advantageous in surveying inaccessible terrain or to acquire rapid reference measurements for the dynamic image-based target detection systems. The concept of spectral purity, considered to be inherent in the spectral endmembers of reference spectral library-based databases need to be revisited to consider for infusing some degree of spectral-contextual-impurity for further usage in the image-based detection systems. Compared to point measurement, a pixel has the inherent structure to infuse geometrical, illumination and micro-environmental settings of material-energy interactions in the reflectance spectra. The pixel spectra may help represent the dynamics of material target spectra acquired at different platforms.

Target detection in space-borne imagery using the reference target spectra from airborne imagery helps evaluate detection possibilities over a wider geographical region. Successful target detections for targets in the space-borne imagery using the reference target spectra from airborne imagery suggests the existence of a spectral continuum between airborne and space-borne imagery. Compared to the results from in-situ or pixel-based THI spectra, the airborne image-based reference spectra produced relatively lesser false alarms in space-borne imagery. For example, in the case of the lowest target detection scenario (N2R; algorithm: CEM), the false alarms reduced from 5624 to 1712 when the confidence of the detection rate is set at 75%. Target detections in the airborne imagery using the reference target spectra from the airborne imagery itself are accurate and unambiguous across all the detection algorithms at the 100% probability of detection rate. However, the target detections in space-borne imagery using the reference target spectra from the space-borne imagery itself are comparable with the results obtained from using the pixel-based THI reference target spectra. At the 75% probability of detection rate, the target detections are erroneous mainly by overestimation—most of the targets are detected albeit with substantial proportions of false alarm. Overall, the results confirm that the strength of spectral conformity of the input reference target spectra determines the quality of the target detection in imagery acquired from different platforms.

4.4.2 Target - Background Interaction: Role of Context

To test the impact of contextual background–target spectral interactions on the repeatability of the target detections, we placed targets of identical material in different colors on different backgrounds. Considering the background–target spectral interactions, the detection of identical materials on identical background vary from being systematic and successful to random and fail. With marginal to moderate variations in the false alarm rate (PFA), our results suggest unambiguous target detection of identical materials on an identical background in both the airborne and space-borne imagery (see Figure 4.20). Compared to the case of identical materials on identical background, detection rates of identical material targets positioned on different backgrounds vary mainly on the local contrast between target material and background. Accordingly, the detection rates vary from being chance matching to consistent detection. A similar observation has been reported by (Yadav et al., 2018b), confirming the substantial effect of scene parameters on the target detection accuracy. In addition, we find that the potential of background interference for altering the detection scores depends substantially on the source of reference target spectra and the detection algorithm.

The variability in the detection rate of identical materials poses a plausible question: How do we standardize the detection rate and ensure detection reproducibility under different environmental, background, and other geometrical factors? The inconsistency in the detection performance needs to be addressed from an algorithmic design perspective, modeling and incorporating the source of uncertainties in the reference target reflectance spectra as observed by different sensors. One of the primary causes for the different detection rates is the non-linearity in the contextual background reflectance recorded by sensors at different platforms, as shown in Figure 4.21(a). Modeling the reference target spectra with possible background mixtures and developing contextual-background sensitive algorithms may enhance target detections across platforms and sensors. Overall, we observe that targets placed on a comparatively reflective local background are detected with lower false alarms ($P_{FA} \sim 10^{-4}$) by all the algorithms. Although a detailed analysis of the role of background is not in the purview of this chapter, our results support the theoretical

perspectives of different target-background outlined by (Matteoli et al., 2014), and we suggest maintaining a balance between model sophistication and its real-time applicability.

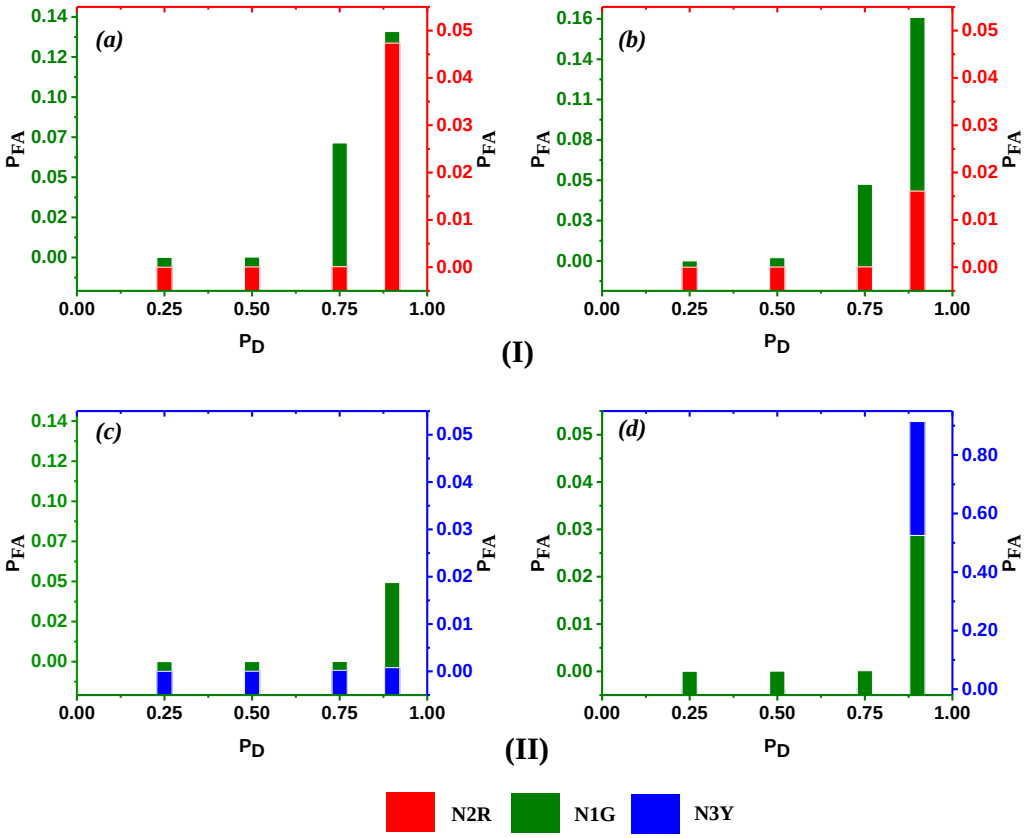

Figure 4.20: False alarms at different levels of P_D for (I) identical target material (N1G and N2R) in the same context (vegetative) for the (a) best case, and (b) worst-case detection performance; (II) identical target material (N1G and N3Y) in a different context (vegetation and soil respectively) for (c) best case, and (d) worst-case detection performance.

4.4.3 Detection Algorithms and their Functional Categorization

Apart from the spectral-geometrical-imaging platform dynamics of the target materials, detection algorithms play a key role in recognizing and identifying material targets. Given the acquisition of appropriate spectral imagery and meeting the minimum dimension of the target material, the detection algorithm employed determines the possibility and quality of target detections. For the given target reference spectra, the functional characterization expected from a potential detection algorithm is the ability

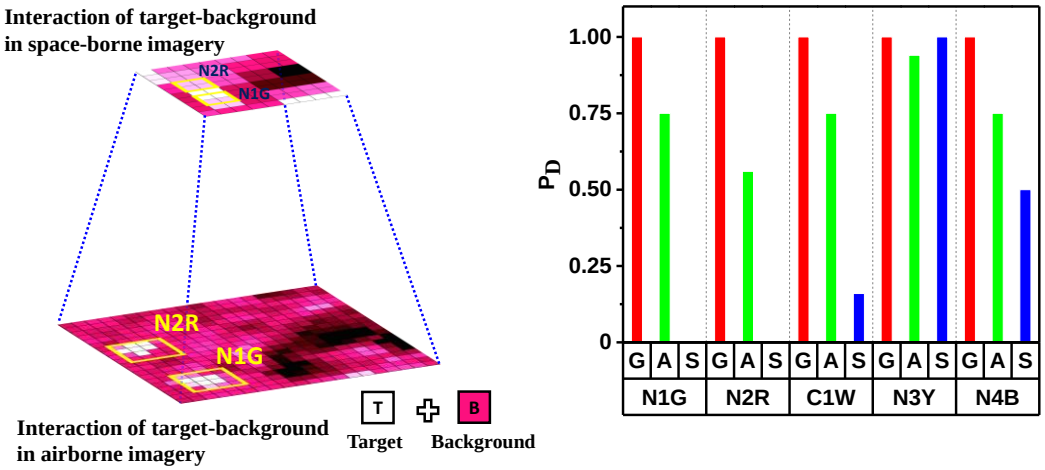

Figure 4.21: (a) Visualization of the non-linear interaction of background signal with the target spectrum for the N2R and N1G targets, and (b) best case target detection continuum results of detection performance across imagery from all the platforms (G-ground, A-airborne, S-space-borne) for all the targets used in at a false alarm rate of 10^{-3} for the in-situ target reference spectra.

to deal with target–background interactions and spectral pattern discrimination in imagery. Based on the functional characteristics, we used three types of detection algorithms, belonging to categories of geometric approach, spectral matching, and background characterization. Target detection of materials in the airborne imagery, with target reference spectra extracted from the same imagery, is accurate and complete (at P_D=75%) by most of the detection algorithms and the material targets. However, major performance limitation of the detection algorithms can be attributed to the sensitivity to backgrounds. The detection rate of an identical material target positioned on two different backgrounds varied substantially by the detection algorithm. Among the spectral matching based detectors, CEM consistently detected material targets across the source of reference target spectra and imagery platform. Yet, the average number of false alarms is ~50, predominantly in the urban areas (see Figure 4.5), which may not meet the practical target detection purposes. The performance of subspace-based detectors is determined by the quality of extracted endmembers, which in turn depends upon the endmember extraction algorithm used. For example, OSP and TCIMF yielded the lowest false alarms for some materials (P_{FA} ~10^{-5} for N1G and

C1W), but high false alarms for other materials (N4B, N3Y with $P_{FA} \sim 10^{-2}\ to\ 10^{-4}$) (see results in Section 3.1.1). However, for the two similar materials placed on a different contextual background, the detection rate varied drastically between the spectral and subspace-based detectors. For example, for the MF the difference in the detection rate between N4B and N1G is ~20 times; whereas, for ACE, it is about 10,000 times.

The adaptability of the sub-pixel detection algorithms, such as CEM, TCIMF, ACE, and OSP, for the detection of engineered materials from space-borne imagery is fraught with a large number of false alarms. While the pixels of target materials are detected, the number of false alarms outweighs the detection rate P_D at 75%. For instance, when the P_D is 75, CEM yielded 3260 false alarms for the detection of the N1G from the space-borne imagery. In addition, the effect of target–background interaction (due to mixed pixels) on algorithms' performance seems pronounced in space-borne imagery (Figure 4.7). However, when the confidence of the detection rate P_D is reduced to 50%, the results from the space-borne imagery (Sentinel-2 at 10 m resolution) are consistent, indicating the potential utility of space-borne imagery for target reconnaissance. We find that the state-of-the-art target detectors needs substantial refinements for target detection problems. A couple of studies suggest the use of local mean and covariance estimation, and quantification of interaction effects for improved detection (Cohen et al., 2012; Wang & Xue, 2017). Algorithms with adaptive target–background signal modeling with incorporations of non-linear signal mixing models for sub-pixel/mixed pixel targets can provide better results compared to the traditional statistical detectors.

4.4.4 Key Elements of Influence in Target Detection

Based on our analyses of the extensive target detections observed under different combinations of background, material, and detection algorithms, we present an empirical estimation of the relative contributions of the three key elements of a remote sensing-based target detection system - ground (including local background), sensor (spectral properties), and target (types and positioning) as vertices of an isosceles triangle. As illustrated in Figure 4.22, the target detection space represents the

possibility of detecting material targets under the full detection possibility (area of the triangle) considering the possible levels of the three key elements. The quality of detections depends upon finding the optimal range in each of the key elements and modeling the appropriate weights. Background contrast (as defined from the target spectral attributes), and sophistication of detection algorithm (ability to localize the target–background spectral attributes) have major contribution compared to the spectral dimensionality of imagery. The spectral features and detection algorithms have equal participation (about 35% each) in the detection as represented by sides of the triangle (Figure 4.22). The base of the triangle, the target-background, has about 30% contribution in the detection and is a landscape driven parameter, not amenable for prior human intervention. Improvement in the precision and detection scores, representing the height of the triangle, is the sophistication of detection algorithms with reference to optimal spectral dimensionality. A stable target detection system will be the weighted combination of the three key elements and will have its detection scores in the triangle represented by 'realistic detection space'. Reaching the most optimized combination of the key elements (indicated by the green circular dot) is the theoretical upper limit of the target detection system.

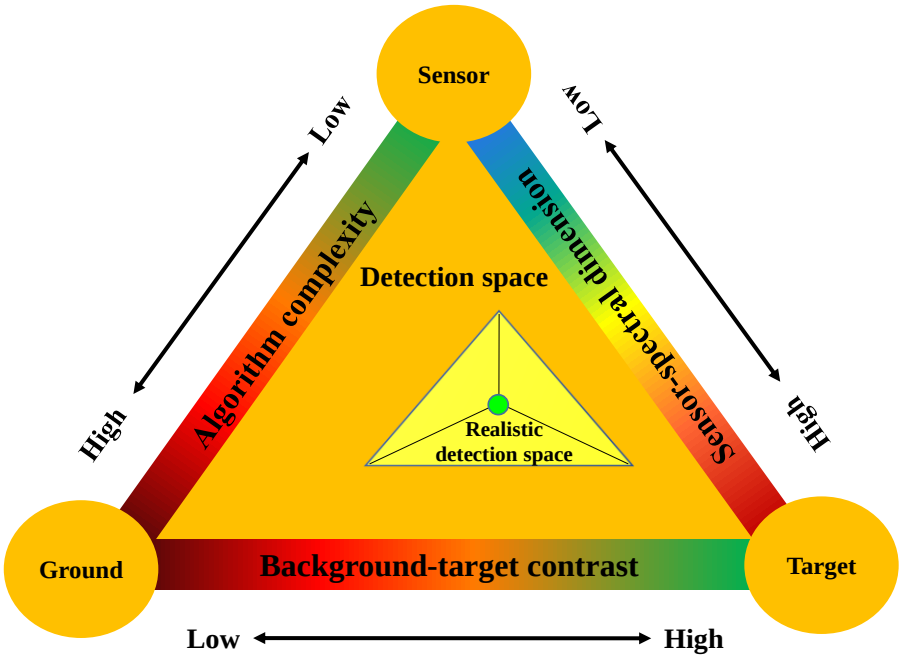

Figure 4.22: Various elements of a target detection system and their mutual correlation in the detection space.

4.4.5 Experimental Dataset

The multi-source multi-platform dataset for target detection will be a valuable resource for the ongoing efforts on target detection using hyperspectral and multispectral remote sensing data. The high-quality in-situ reference spectral data, acquired both in point and pixel mode, will be helpful to test the nuances of detection related problems and assessment of detection algorithms. Since the present dataset was acquired from an urban neighborhood, the complexity of the imagery would provide a rigorous test to the existing theories about the detection problems. The detection of engineered material at pixel level from satellite data is vital for strategic purposes, and the dataset acquired in this research can be used for validating such endeavor. For all the practical purposes, we propose that the detection metric (P_D) of target detectors should be relaxed and re-evaluated according to the imaging complexity of the scene. Target detection can be undertaken in both the reflectance and radiance modes. However, for the present work, we have only tested the detection performance in the reflectance domain. Radiance domain target detection will be pursued as future work. The experimental dataset used in this study will be made available on an appropriate freely accessible public platform.

4.5 Chapter Conclusions

In this chapter the experimental setup for a multi-platform benchmark remote sensing dataset and various aspects of target detection, algorithm development and their evaluation are presented. We have carried out experiments on target detections as a function of sensor, platform, target–background, and the source of reference target spectra. We observe unambiguous detection of targets in the airborne imagery. The false alarm rate is substantially low if the probability of detection (P_D) is reduced to 75%. The continuity and the quality of target detections are found to be influenced by the source of reference target spectra. While the target–background interaction is one of the key components determining the quality of detection, it is not a decisive constraint on the overall detection of targets. Target detection results from the ground-level hyperspectral imagery-based target reference spectra are at par with point-based in-situ target reference spectra. The ground-based hyperspectral imaging sensor is a

viable source for rapid acquisition of target reference spectra. A non-imaging spectroradiometer generated in situ reference spectrum may not conform to the landscape area element-based target pixel spectrum in spectral imagery. The continuity of target detections from the ground to space, though with different proportions of false positives, suggests the viability of satellite imagery-based target detection. However, further experiments are required to generalize this observation. Notwithstanding the quality spectral data sources, detection algorithm determines the quality of target detections. The false positives rate is substantial in most of the detection algorithms evaluated, calling for the development of multi-resolution spectral dimensionality invariant target detection algorithms.

CHAPTER 5

INFLUENCE OF ATMOSPHERIC MODELLING ON SPECTRAL TARGET DETECTION IN MULTI-PLATFORM REMOTE SENSING DATA

Prelude: This chapter presents quantitative assessment of the impact of atmospheric parameters on the detectability of engineered targets. Specifically, the influence of critical atmospheric parameters such as AOT, atmospheric profiles, and aerosol models are on the sensor reaching radiance from the target detection perspective is assessed. The multi-platform dataset described in the Chapter 4 is used for the analysis. We formulated the radiance spectral library by simulating top-of-atmosphere (TOA) radiance spectra using the 6S RTM. We have considered two cases of target radiance spectra simulations, i.e., (i) corresponding to a grid of different AOT values for a predefined atmospheric and aerosol profile, and (ii) corresponding to varying combinations of atmospheric and aerosol profiles at a given AOT. It is observed that change in the magnitude of AOT across atmospheric models and selection of wrong atmospheric models resulted in decision-changing implications in the target detection modelling.

5.1 Introduction

The sparse nature of targets combined with the propagations of uncertainties in the target imaging process, such as sensor noise, atmospheric scattering, absorption, target surface characteristics, etc., deter or hinders a reliable detection rate.

---

[1]The contents of this chapter have been submitted for publication in *ISPRS Journal of Photogrammetry and Remote Sensing* and is under review. Authors: Sudhanshu Shekhar Jha, Rama Rao Nidamanuri, Ientilucci Emmett J.

Target detection from remote sensing platforms such as UAV, airborne flights, etc., requires a multi-dimensional approach to improve detection accuracy, including mitigation of uncertainties caused by inefficient atmospheric parameter modelling. There have been few studies on the effect of various factors such as the size of the target, target-background interaction, sensor characteristics, algorithms (Wang & Xue, 2017; Yadav et al., 2018a) on target detection performance. Still, the impact of the RTM-based estimates, with associated assumptions, of the atmospheric variables such as standard atmospheric profiles, aerosol models, etc., and associated uncertainties related to target detection performance has been overlooked and, in general, reported less in the literature (Yarbrough et al., 2010; Sundberg, 2018; Kim et al., 2019).

Usually, a target detection chain involves RTM (Figure 1.3) in the imagery pre-processing stages to compensate for the atmospheric effects (scattering and absorption of the signal) from the measured at-sensor radiance. Such a process is termed atmospheric correction or compensation (AC) or inverse modelling (IM) and is generally carried out using physics-based models such as MODTRAN, 6S, for example(Ientilucci & Bajorski, 2006; Ientilucci & Adler-Golden, 2019). It is common to use the AC mode of data pre-processing for numerous remote sensing applications (Agapiou et al., 2011b; Martins et al., 2017). AC approach for quantifying remote sensing products involves intensive computing resource and are often time-consuming (pixel-by-pixel inversion), which can prove to be a bottleneck for time-critical applications. An alternative approach, termed forward-modelling (FM), uses in-situ reflectance data of the objects at the ground so as to approximate their at-sensor spectral radiance (Matteoli et al., 2009; Ientilucci, 2017). The FM approach requires less computational resources as the modelling process is limited to generating a few spectral vectors corresponding to a gamut of atmospheric parameters, unlike the AC approach, which would require the generation of several data cubes for the same (Matteoli et al., 2010).

Physics-based models typically require multiple parameters to approximate the atmosphere, such as columnar temperature, pressure, water vapor, ozone, gaseous transmittance, scattering model, aerosol optical thickness, etc. The reliability of remote sensing-based studies is often directly dependent on the quality of estimation of these

atmospheric parameters (Nia et al., 2015; Marcello et al., 2016; Sabater et al., 2017; Seong et al., 2020). In terms of data models and hardware capability, substantial developments in computing infrastructure have encouraged research in exploring efficient methods to expedite on-board methods of the various recurrent problems in remote sensing (Bue et al., 2015). Although some studies have been reported on onboard AC, their scope remains limited due to the exhaustive resource required for such implementations. On the other hand, accelerated hardware components such as Field Programmable Gate Arrays (FPGA) have shown that real-time applications, such as object detection and classification, can be carried out given computational overheads are optimized (Gyaneshwar & Nidamanuri, 2020; Nascimento et al., 2020). One of the limiting factors for carrying out such operations is uncertainties in modelling the atmospheric parameters. Although few studies have been carried out to analyse the impact of modelling the atmospheric parameters on remote sensing derived products, exhaustive studies have been less reported in the literature.

In this chapter, fulfilling the final objective of the thesis, results and critical analyses on the performance of target detection in multi-platform hyperspectral and multispectral imagery under different atmospheric models and parameter scenarios have been presented. A hypothetical situation, illustrated in Figure 5.1, in which the target cognition-recognition cycle becomes an integral part of such a framework's overall applicability, arises in an onboard target detection framework. This chapter aims to 1) analyse the impact the atmospheric model has on target detection, and 2) assess the applicability of the FM approach for target detection in a multi-platform target detection dataset. We have modelled the atmospheric variables using the 6S RT model and transformed the in-situ target reflectance target spectra to at-sensor radiance spectra using standard atmospheric models containing precomputed estimates of the atmospheric parameters. Finally, we carried out target detection using various state of the art target detectors (ACE, CEM and MF) and compared the results for all the combinations of atmospheric state variables and algorithms.

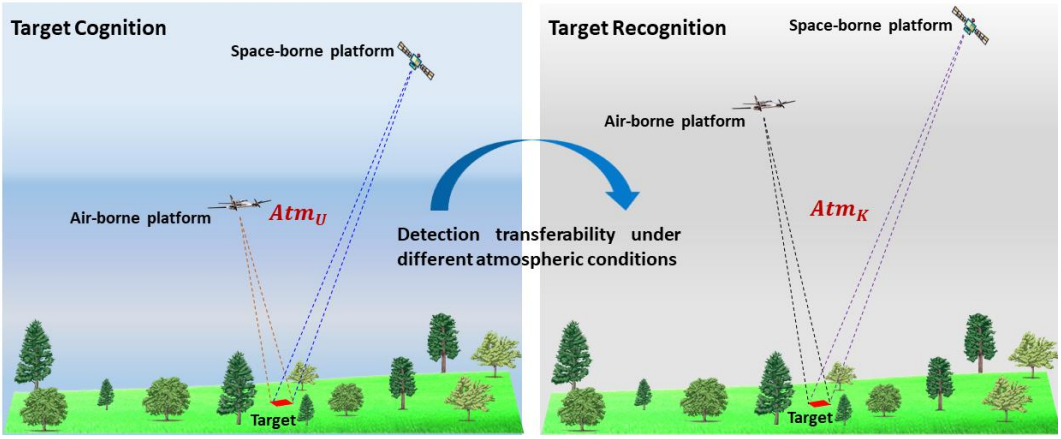

Figure 5.1: Two different space-time target detection scenarios, with differing atmospheric conditions (Atm_U, Atm_K), leading to a potential mismatch of atmospheric parameters.

5.2 Materials and methods

For the present study, we used the dataset described in the Chapter 4 and the details on in-situ target reference data processing can be found in the Section 4.2.1 and 4.2.2.

5.2.1 Data pre-processing: reference target spectra and imagery pre-processing

We deployed two different spectral sensing instruments: a point-based spectroradiometer and pixel-based THI, to collect the in-situ reference target reflectance spectra. Although the THI captures imagery at about 1cm spatial resolution, we have spatially resampled imagery to 20 cm spatial resolution. The THI raw data were calibrated using a white reference panel to obtain the radiance data cube and subsequently converted the radiance cube to reflectance cube using the in-scene empirical line (EL) method (Smith & Milton, 1999). Different patches (ROI) over the target were selected, and spectral responses were averaged to yield a THI in-situ target spectrum. In addition, we used a field spectroradiometer (Spectra Vista Corporation, HR-1024i, USA) to collect the point-based in-situ target spectrum in the 400-2500 nm wavelength range as per standard procedure (*Field Spectroscopy Guide with SVC I-Series Spectroradiometers*, 2010). Once all the reflectance target spectra are collected from the ground, they are further processed to match the spectral range of AVIRIS-NG and Sentinel-2 sensors via spectral resampling and convolution operation using

respective sensor response function (SRF). In the target spectral data acquired using the THI sensor, we omitted spectral data beyond 900 nm due to inherent sensor noise and low signal-to-noise ratio (SNR). In the case of THI-based input target reference, we resampled the AVIRIS-NG imagery to THI wavelength range which resulted in imagery with 104 spectral bands for target detection.

Since we used forward modelled target spectra for detection in this experiment, the target imagery needed to be of the top-of-atmosphere (TOA) radiance. We used the level-1 TOA radiance product for executing target detection using simulated target reference spectra in this chapter. Sentinel-2 was converted from original level L1C (TOA reflectance) to TOA radiance using the SNAP tool processor called Sen2Cor (Louis et al., 2016). We removed the bands in the water vapour absorption region of the AVIRIS-NG imagery between 1348–1443 nm,1804–1954 nm, and 2485–2500 nm. The resultant imagery contained 370 spectral bands. We resampled the Sentinel-2 satellite imagery to 10 m spatial resolution to match the target size.

5.2.2 Target signal simulation: Atmospheric processor

Since the electromagnetic radiations in the optical region undergo perturbation caused by atmospheric components such as aerosols, water particles, clouds, dust, etc., various physical-based radiative transfer models approximate different parameters to compensate for the net atmospheric effects. 6S incorporates various standard atmospheric models defined by approximation of climatic conditions, such as Tropical, Midlatitude Summer, etc. The atmospheric profiles have predefined columnar profiles (0-100kms) of different variables such as atmospheric pressure (mb), temperature (^{o}K), water vapor (g/m^3), and ozone concentrations (g/m^3) as a function of height (km). Further, based on aerosol properties such as AOT, the mean radius of the aerosol particle, real/imaginary refractive indices, particle distribution function, and angstrom coefficient, several standard aerosol models (continental, urban, maritime, desert, etc.) are defined in 6S model. As shown in equation (2.29), the values of ρ_{ac} for the targets are known a priori from the in-situ measurements, we can simulate L_{TOA} reaching the sensor owing to different atmospheric variables using equation (2.3). In literature, the form of TOA radiance described by equation (2.29) is known as the FM. The radiance

spectral library is constructed by running multiple runs of 6S on the input in-situ target surface reflectance. A schematic diagram of the overall process is shown in Figure 5.2.

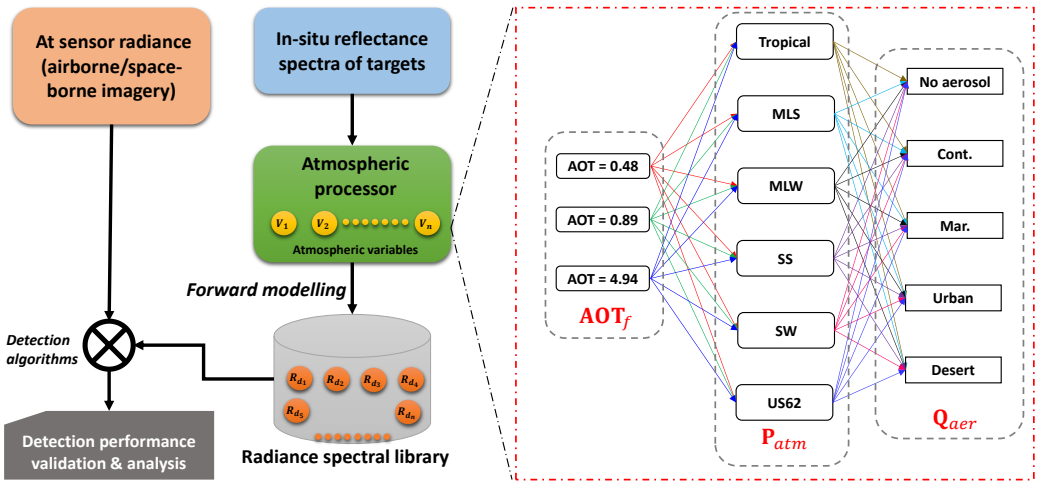

MLS : midlatitude summer; **MLW :** midlatitude winter; **SS :** subartic summer; **SW :** subartic winter; **Cont. :** continental; **Mar. :** Maritime

Figure 5.2: 6S RT model-based target modelling system design for evaluating spectral target detection performance in multi-platform remote sensing imagery setup.

We considered two cases of target radiance spectra simulation: (i) simulation corresponding to a grid of different AOT values (0-5) for a predefined atmospheric (Tropical) and aerosol (Continental) profile, and (ii) simulation corresponding to different combinations of atmospheric and aerosol profile at a given AOT = {0.48,0.89,4.94} corresponding to equivalent visibility of approximately 15km, 7km, and 1 km respectively (Bhatia et al., 2018). Considering the geographical location of the target scene (Tamil Nadu, India), a tropical atmospheric profile with a continental aerosol model were selected (Mishra et al., 2020) for the predefined parameters of the case (i). Denoting different atmospheric profiles as $\mathbf{P}_{atm}$= {Tropical, Midlatitude Summer, Midlatitude Winter, Subartic Summer, Subartic Winter, US62}, aerosol profiles as $\mathbf{Q}_{aer}$ ={No aerosol, Continental, Maritime, Urban, Desert), TOA radiance $\mathbf{TOA}_{\mathrm{RAD}}(r)_i$, for case (i) is represented as:

$$\mathbf{TOA}_{\mathrm{RAD}}(r)_i = \boldsymbol{\psi}_{\mathbf{P}_{atm_{Tropical}}, \mathbf{Q}_{aer_{Continental}}}(\mathbf{AOT}_{var}), \quad (5.1)$$

where,

$\mathbf{AOT}_{var} = \{0, 0.5, 1, 1.5, 2, 2.5, 3, 3.5, 4, 4.5, 5\}$, and subscript i= values of TOA radiance at different AOT values

An example illustrating the simulated radiance spectra from the atmospheric processor following equation (5.1) is shown in Figure 5.3.

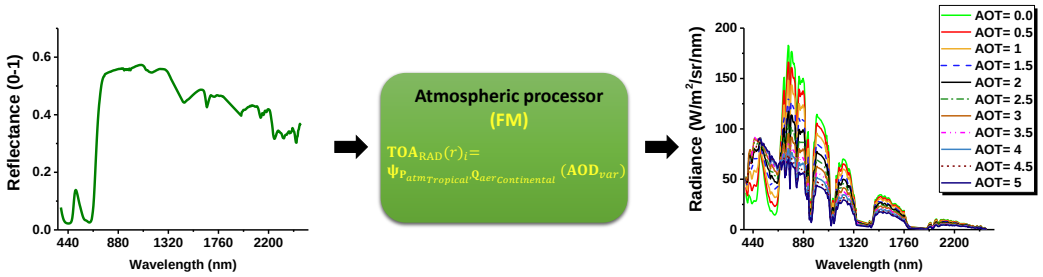

Figure 5.3: FM approach for simulation of the N1G target radiance spectra using Equation (5.1) for various AOT values using the in-situ reflectance spectra

Further, $\mathbf{TOA}_{\mathrm{RAD}}(r)_i$ for case (ii) at different discrete values of AOT is given as:

$$\mathbf{TOA}_{\mathrm{RAD}}(r)_i = \boldsymbol{\psi}_{\mathbf{AOT}_f}\left(\mathbf{P}_{atm_p}, \mathbf{Q}_{aer_q}\right), \quad (5.2)$$

where, $\mathbf{AOT}_f = \{0.48, 0.89, 4.94\}$, subscripts p and q represent different atmospheric and aerosol profiles.

5.2.3 Target detection algorithms

Since targets in this experiment fall under both the full-pixel and sub-pixel category, we used MF, ACE, and CEM detectors. A detailed discussion on the formulation of these detectors can be found in the Section 2.2.

5.2.4 Quantitative evaluation of detection performance and spectral analysis

The target detection results using the algorithms described above from airborne and space-borne imagery were compared for all the simulated target reflectance spectra (shown as radiance spectral library in Fig. 5.2). We have used the receiver operating curve ROC, a graph between the probability of false alarm (P_{FA}) and the probability of

detection (P_D), for reporting the detection performance, as described in the Section 4.2.5 (equation 4.1).

We have carried out a quantitative spectral analysis of the simulated target spectra compared to the imagery target radiance spectra since both spectra's conformity is often found to influence the detection results. The spectral analysis also gives an insight into the underlying physical process that might result in a mismatch between imagery derived target spectra and the input reference target spectra caused by a mismatch of the atmospheric model assumption. For each of the simulated target radiance spectra, we have applied multiple spectral matching metrics: spectral angle mapper (SAM) (Kruse et al., 1993b), and spectral information divergence (SID) (Chang, 2000b), and compared it to the image derived (both from the airborne and space-borne platforms) target radiance. The mathematical formulation of SAM and SID is described in the section 4.2.5 (equation 4.2 and 4.3).

5.3 Results

In this section, we present the results of target detection for various TOA radiance spectra simulated under different atmospheric conditions. For ease of comparison of the performance by various algorithms, we benchmarked the P_{FA} for detection results at $P_D = 75\%$ for airborne image and $P_D = 50\%$ for space-borne image (Jha and Nidamanuri 2020). To illustrate this, we present an example (result for N1G by MF under various AOT conditions), shown in Figure 5.4, showing the approach used to report results in this chapter. We fixed the P_D at 75% (shown by the horizontal dotted line) and noted the first intersection point of the ROC curve and the $P_D = 75\%$ line to identify the respective P_{FA}.

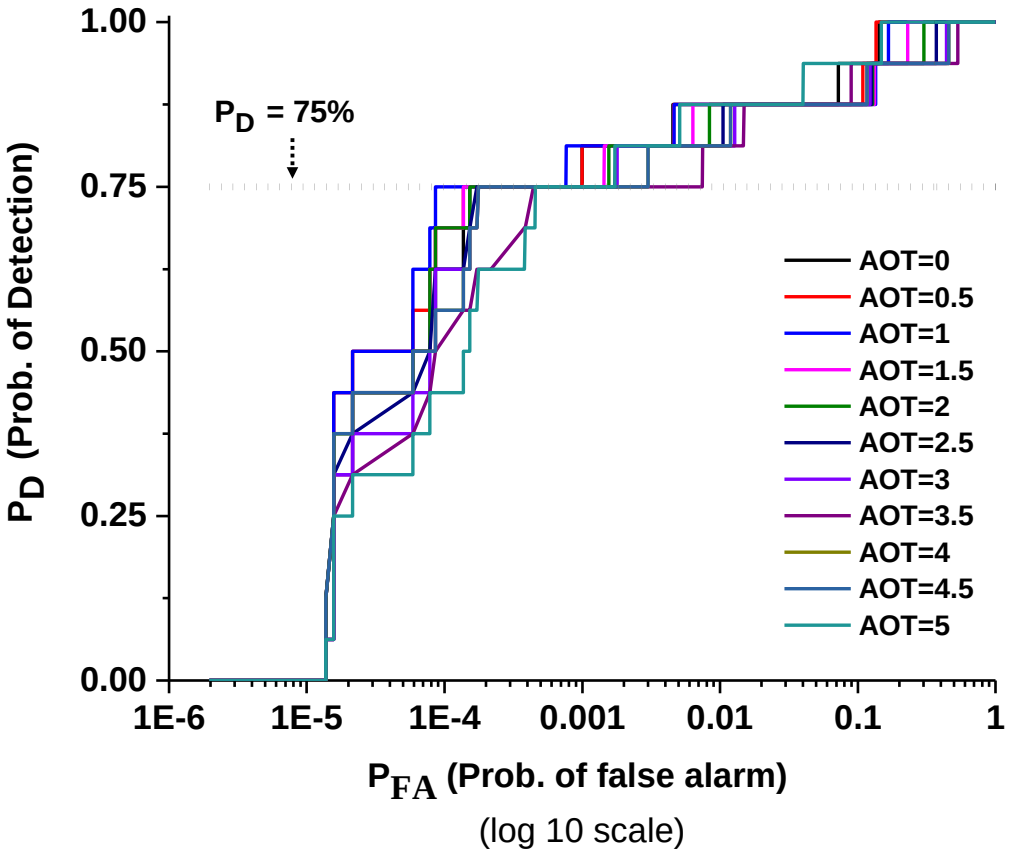

Figure 5.4: An example target detection result for the N1G target under varying AOT conditions by the MF target detection algorithm.

5.3.1 Target Detection performance from airborne imagery for simulated target spectra induced by AOT and atmospheric model assumption

5.3.1.1 Target detection performance under varying AOT condition

This section presents the target detectability at various AOT values in the range 0 - 5 for two different input target reference sources, i.e., point and pixel mode with a tropical atmosphere and continental aerosol model.

5.3.1.1.1 Detection statistics for point-based field spectra

Figure 5.5 shows the target detection performance by various target detectors for different target materials as a function of AOT. The input reference spectrum was simulated using the point-based in-situ reflectance spectra. The influence of AOT on

the detection performance is evident as the degree of detectability amongst the used algorithms varies significantly from one another and also differs from material to material of the targets used in the experiment. The robustness of detection due to the target spectra mismatch between reference and image spectra depends substantially on the AOT. As shown in Figure 5.5, AOT's effect is profound after a certain threshold, such as after AOT=2.5 in the case of N1G (Figure 5.4(a)). The detection rate is least affected by the variation of AOT for the CEM detector. ACE, which detects materials based on spectral features (geometry-based), misses the target in most cases, even at low AOT values (higher visibility). For instance, for targets N2R, N3Y, and N4B, the P_{FA} is unusually high (0.35, 0.674, 0.39 at even low values of AOT). Moreover, in the cases where MF has detected targets unambiguously (e.g., for N1G, C1W), the change in AOT has resulted in a substantial increase in the number of FAs.

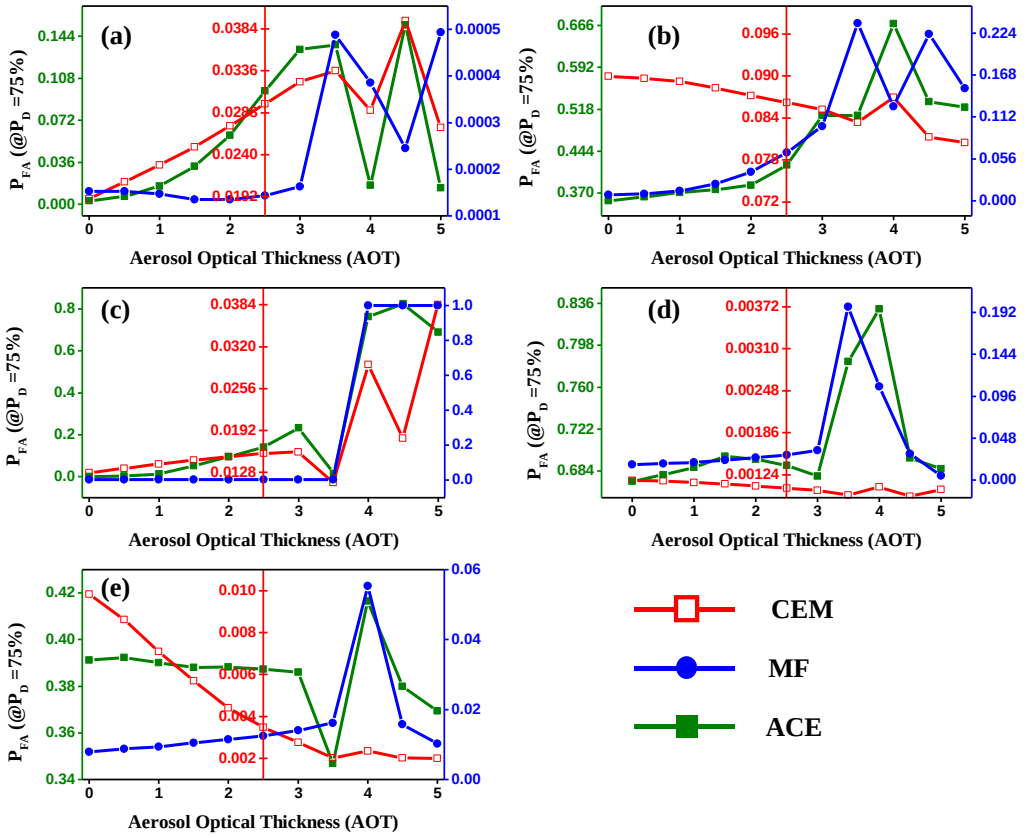

Figure 5.5: Target detection in airborne imagery: variation of P_{FA} due to changes in AOT for target detection in airborne imagery. Illustrated are P_{FA} values when the $P_D = 75\%$ for targets (a) N1G, (b) N2R, (c) C1W, (d) N3Y, and (e) N4B with simulated TOA target radiance spectra at different AOT values between 0 and 5 using point-based target reflectance.

5.3.1.1.2 Detection statistics for pixel-based target spectra

Figure 5.6 shows the target detection performance for different target materials as a function of AOT, when spectra from THI were used as the input reference spectra. The input reference spectra were simulated from the THI based reflectance spectra. In general, target detectability in airborne imagery using THI-based reference spectra in the radiance domain seems to have been substantially influenced by target contrast and background components (i.e., we see a variation with all materials, even at lower AOT's). It is evident from Figure 5.6 that although N1G and N2R are satisfactorily detected from all three algorithms ($P_{FA} \sim 10^{-2} - 10^{-3}$), we might conclude that the MF and ACE detectors failed to detect the target. The failure of ACE and the MF can be attributed to a mismatch of the simulated spectra and image spectra. In the case where successful detection of targets is possible, algorithms are almost impervious to change of AOT value up to 2.5.

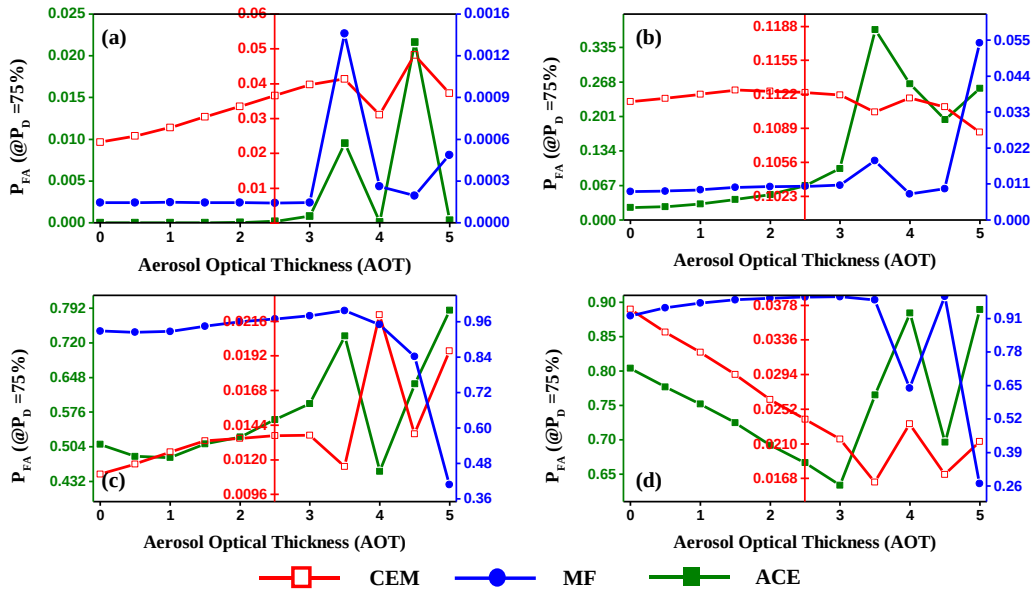

Figure 5.6: Airborne imagery detection results. Illustrated are P_{FA} values when the $P_D = 75\%$ for targets (a) N1G, (b) N2R, (c) C1W, (d) N3Y, and (e) N4B with simulated TOA target radiance spectra at different AOT values between 0 and 5 using pixel-based THI target reflectance.

5.3.1.2 Target detection performance as a function of standard aerosol models for different standard atmospheric models at various AOT values

In this section, we analyse the effects of varying the aerosol model (e.g., continental, maritime, etc.) within a given atmospheric model (e.g., tropical, US62, etc.) at different levels of AOT. Similar to section 5.3.1.1, we present the result for point and pixel-based source of the target reference sources.

5.3.1.2.1 Detection statistics for point-based field spectra

Figure 5.7-5.11 shows the target detection performance of different detectors for the targets N1G (Figure 5.7), N2R (Figure 5.8), C1W (Figure 5.9), N3Y (Figure 5.10), and N4B (Figure 5.11). The x-axis represents different aerosol models (i.e., N-Aero = no aerosol, Cont. =continental, Mar. = Maritime, Urb. = Urban, and Des. = Desert) wherever applicable. Detection results indicate inherent randomness in the performance. The performance is heavily penalized when choosing the "wrong" atmospheric model compared to a mismatch related to the aerosol model. For a lower AOT value (0.48 and 0.89), we see the aerosol models' influence at a given atmospheric model is not significant. However, at a high AOT value, the detection performance stability reduces to a purely random phenomenon. Generally, for most of the targets, such as N2R, N3Y, and N4B, the performance of the ACE detector is poor since the number of false alarms (FAs) for detection at P_D=75% is staggeringly high, possibly caused by the sensitivity of the ACE detector to the spectral variability introduced in the reference target signal by the TOA radiance signal simulation process. MF and CEM are least affected by the aerosol model's variation, albeit different atmospheric models yield different results. A tropical atmospheric model produces the best results for the MF detector, whereas CEM performs best for the Subarctic winter atmospheric model. We observe that the MF yields the best detection results ($P_{FA} \sim 10^{-4}$) for a particular atmospheric model (Tropical), but at the same time is very sensitive to changes in an atmospheric model (FAs amplify to 10-100 times). Although CEM yields inferior results compared to the MF for some of the targets (FAs in the range of $10^{-2}\sim10^{-3}$ for N1G, C1W), the general takeaway is that the results are relatively stable and robust across various atmospheric models. This can be attributed to the

nature of the MF detector, which is more sensitive to spectra shape in contrast to CEM, which can discriminate targets based on signal contrast of targets and background.

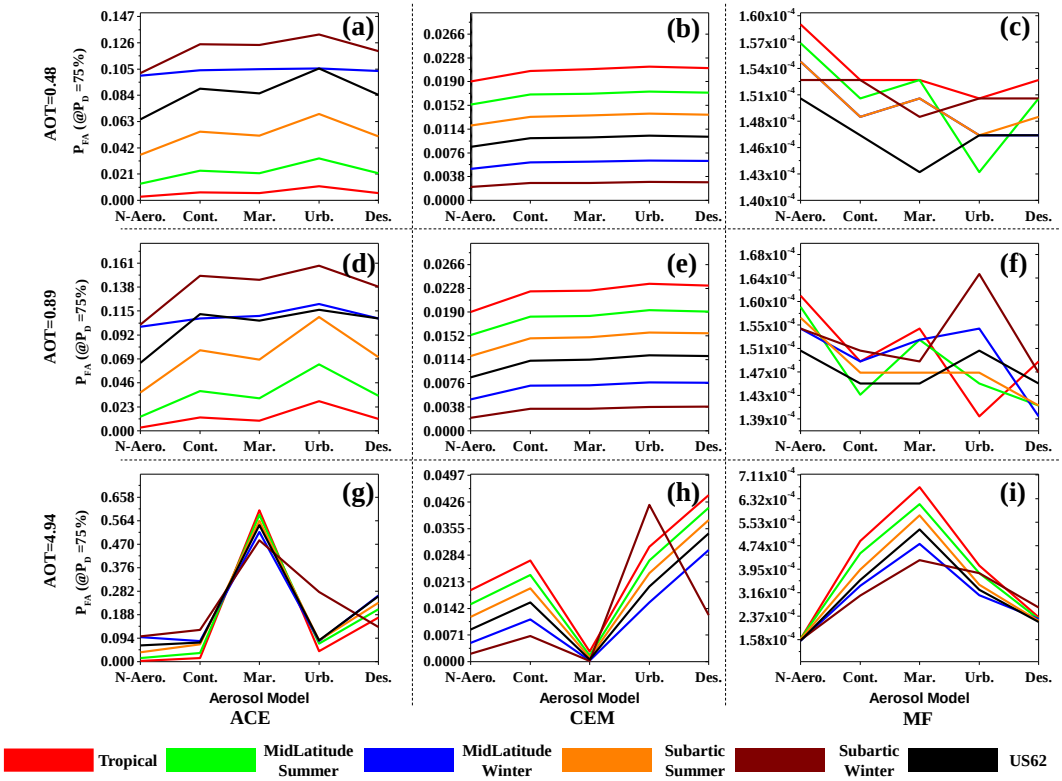

Figure 5.7: Airborne imagery detection results. Illustrated are P_{FA} values when the $P_D = 75\%$ for the N1G target with simulated TOA target radiance spectra at (a-c) AOT = 0.48, (d-f) AOT = 0.89, and (g-i) AOT = 4.94 for different standard aerosol models (i.e., x-axis) at given standard atmospheric models (i.e., coloured line) using point-based target reflectance.

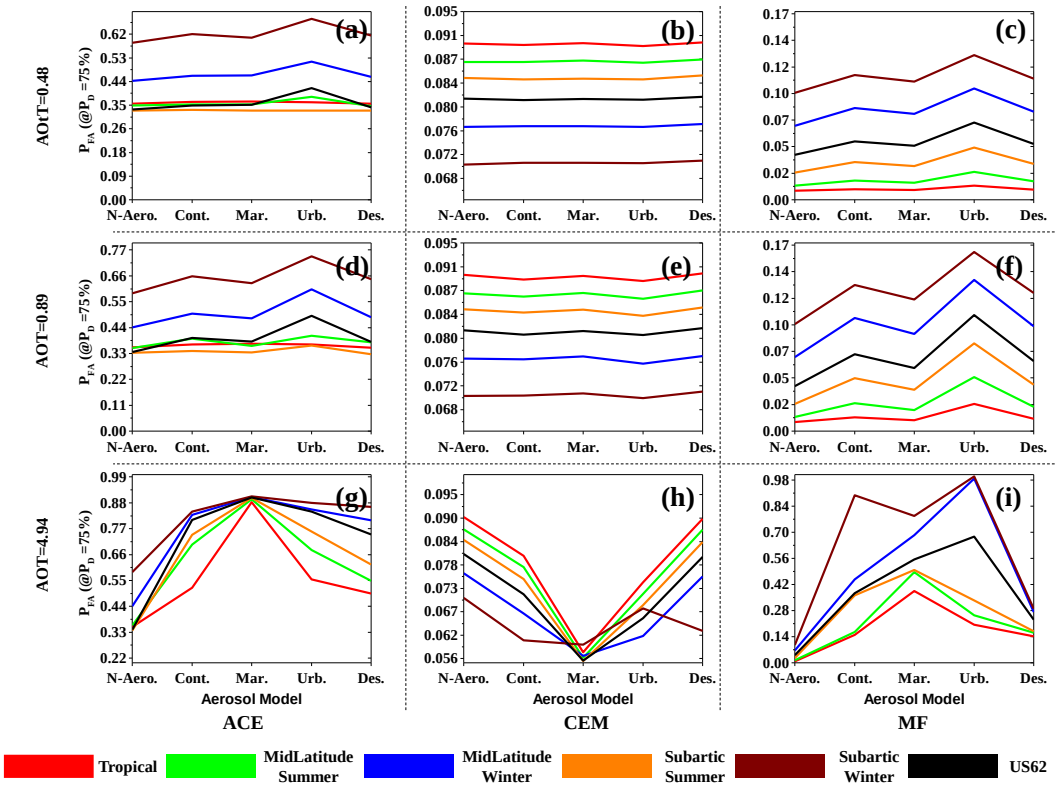

Figure 5.8: Airborne imagery detection results. Illustrated are P_{FA} values when the $P_D = 75\%$ for the N2R target with simulated TOA target radiance spectra at (a-c) AOT = 0.48, (d-f) AOT = 0.89, and (g-i) AOT = 4.94 for different standard aerosol models (i.e., x-axis) at given standard atmospheric models (i.e., coloured line) using point-based target reflectance.

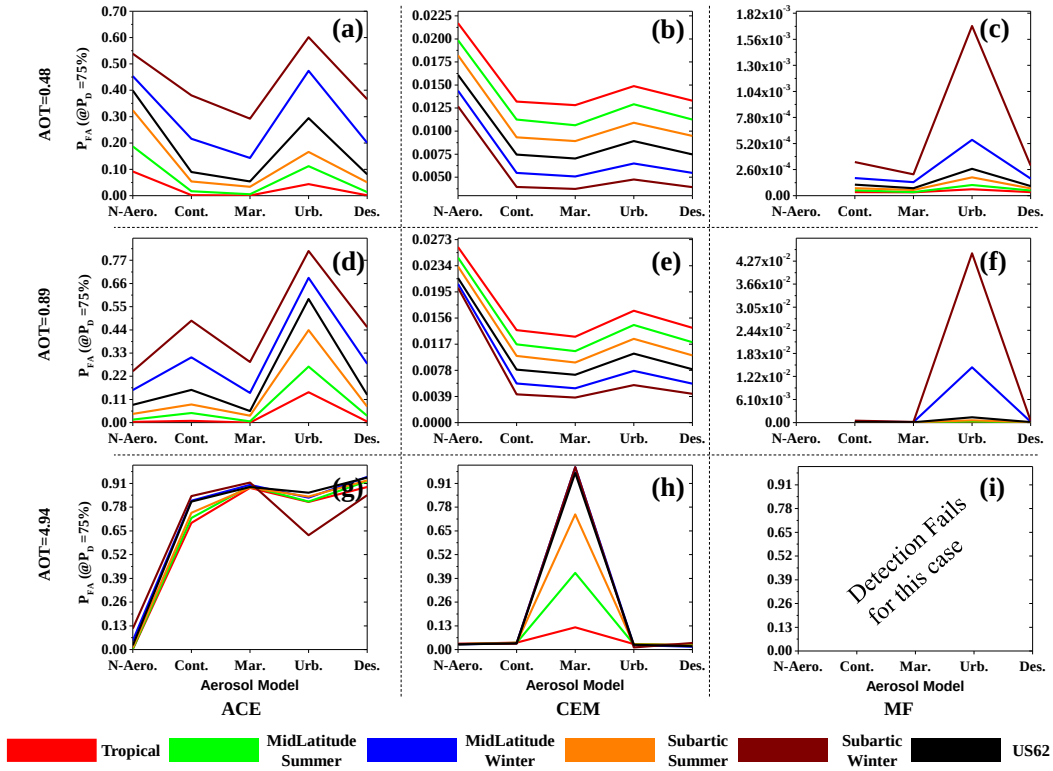

Figure 5.9: Airborne imagery detection results. Illustrated are P_{FA} values when the $P_D = 75\%$ for the C1W target with simulated TOA target radiance spectra at (a-c) AOT = 0.48, (d-f) AOT = 0.89, and (g-i) AOT = 4.94 for different standard aerosol models (i.e., x-axis) at given standard atmospheric models (i.e., coloured line) using point-based target reflectance.

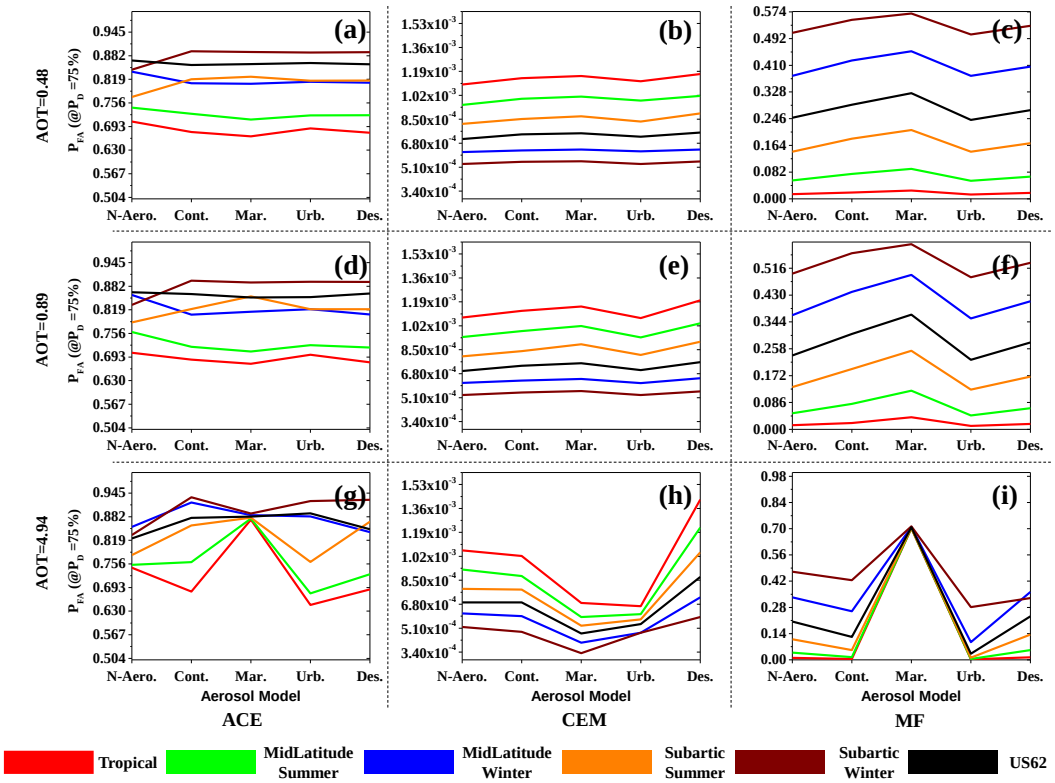

Figure 5.10: Airborne imagery detection results. Illustrated are P_{FA} values when the $P_D = 75\%$ for the N3Y target with simulated TOA target radiance spectra at (a-c) AOT = 0.48, (d-f) AOT = 0.89, and (g-i) AOT = 4.94 for different standard aerosol models (i.e., x-axis) at given standard atmospheric models (i.e., coloured line) using point-based target reflectance.

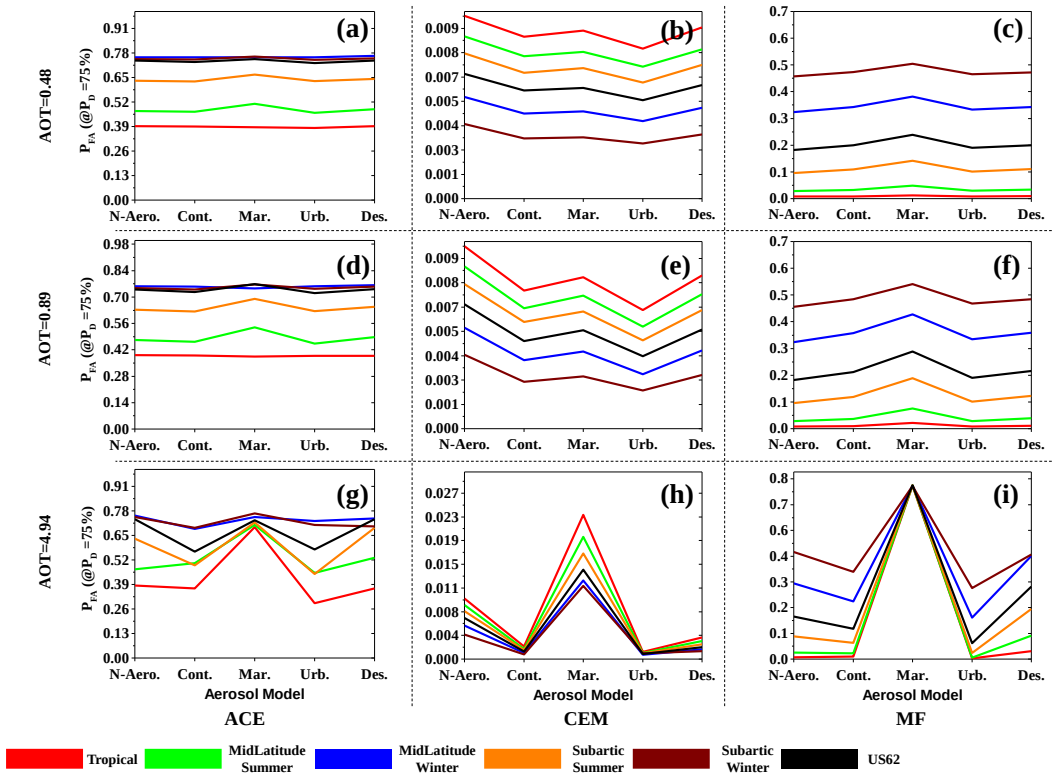

Figure 5.11: Airborne imagery detection results. Illustrated are P_{FA} values when the $P_D = 75\%$ for the N4B target with simulated TOA target radiance spectra at (a-c) AOT = 0.48, (d-f) AOT = 0.89, and (g-i) AOT = 4.94 for different standard aerosol models (i.e., x-axis) at given standard atmospheric models (i.e., coloured line) using point-based target reflectance.

5.3.1.2.2 Detection statistics for pixel-based target spectra

We present selected results for the targets whose detection rate is either relatively the best or worst for brevity. Detection results for the N1G target in the THI-based in-situ spectrum indicate the best detectability among all the targets, as shown in Figure 5.12, while the N4B target has the lowest detection rate. Although the choice of atmospheric model and aerosol model at different AOT values does play a role in the levels of P_D and P_{FA}, the overall FA rate for N1G remains low regardless of the choice of different aerosol and atmospheric models. Among the ACE, CEM, and MF detectors, the lowest P_{FA} is obtained using ACE with an order of $10^{-5} - 10^{-6}$ followed by MF with a FA rate at 10^{-4}. However, with a higher degree of AOT level (AOT = 4.94), ACE's performance takes a significant hit and the P_{FA} increases approximately 100 times to a level of 10^{-4}. On the other hand, although CEM's P_{FA} is highest amongst all the detection algorithms for the N1G target, the detection rate remains stable for

different changes in aerosol and atmospheric models at several values of AOT, suggesting the robust nature of the detector. In Figure 5.13, we see that the performance levels of both ACE and MF change from a high detectability rate for N1G (Figure 5.12) to a complete failure for the case of N4B (Figure 5.13). As observed for the case of point-based in-situ target spectra, spectral detectors like ACE and MF fail to detect most of the targets, whereas the CE delivers a $P_{FA} \sim 10^{-3}$ for a tropical atmospheric model and a maritime aerosol model at all AOT levels.

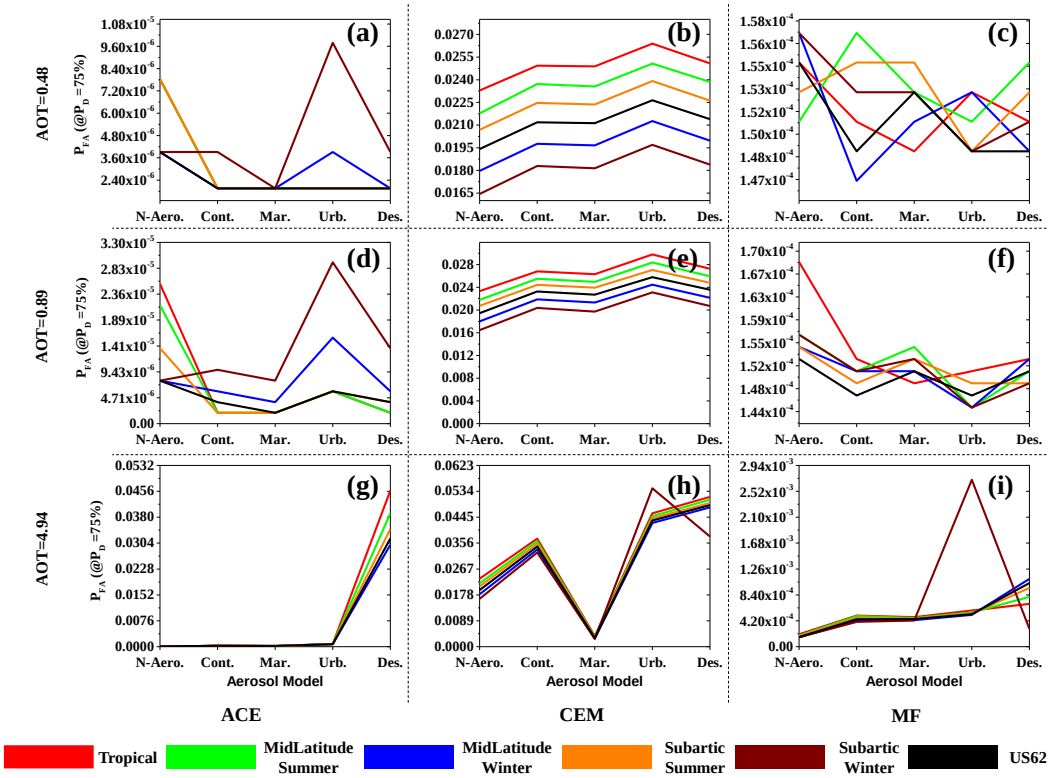

Figure 5.12: Airborne imagery detection results. Illustrated are P_{FA} values when the $P_D = 75\%$ for the N1G target with simulated TOA target radiance spectra at (a-c) AOT = 0.48, (d-f) AOT = 0.89, and (g-i) AOT = 4.94 for different standard aerosol models (i.e., x-axis) at given standard atmospheric models (i.e., coloured line) using pixel-based THI target reflectance.

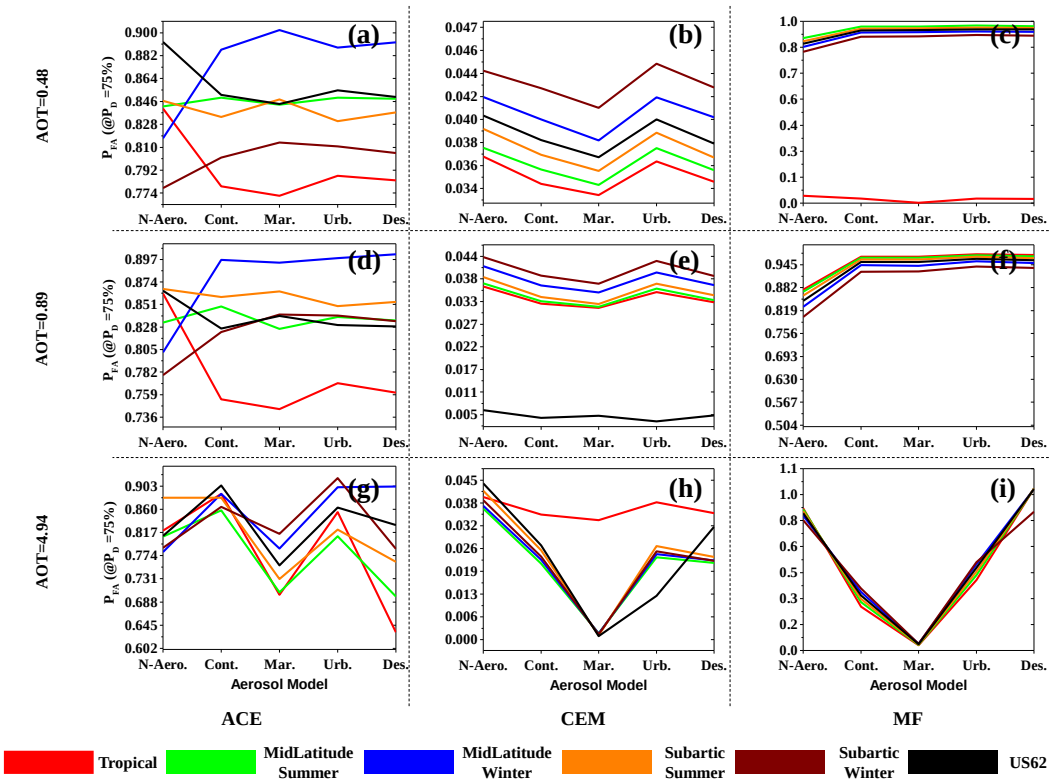

Figure 5.13: Airborne imagery detection results. Illustrated are P_{FA} values when the $P_D = 75\%$ for the N4B target with simulated TOA target radiance spectra at (a-c) AOT = 0.48, (d-f) AOT = 0.89, and (g-i) AOT = 4.94 for different standard aerosol models (i.e., x-axis) at given standard atmospheric models (i.e., coloured line) using pixel-based THI target reflectance.

5.3.2 Spectral target detection from space-borne imagery for simulated target spectra induced by AOT and atmospheric model assumption

5.3.2.1 Target detection performance under varying AOT condition

5.3.2.1.1 Detection statistics for point-based field spectra

Figure 5.14 shows the detection performance from space-borne imagery (Sentinel-2) using various detectors for all the simulated (i.e., different AOT values) target TOA radiance spectra derived from the field-based point reference spectra. Unlike the airborne sensor, the detectability of targets seems to be substantially influenced by choice of AOT. The spectral variability caused by different AOT values plays an important role in detection. While the target detectors such as ACE and MF fail to detect

all the targets, the CEM detector delivers an overall satisfactory performance with FAs in the range of $10^{-2}\sim10^{-4}$. In particular, detection of N1G by CEM shows a highly random nature of detection using TOA radiance spectra. In contrast, successful detection of N2R, C1W (albeit high FA than N2R), and N3Y indicate the possibility of target detection from a space-borne platform. Missed targets such as N4B indicate the limited use of the space-borne remote imagery to detect dark materials, i.e., materials with low spectral radiant intensity for a point-based target reference.

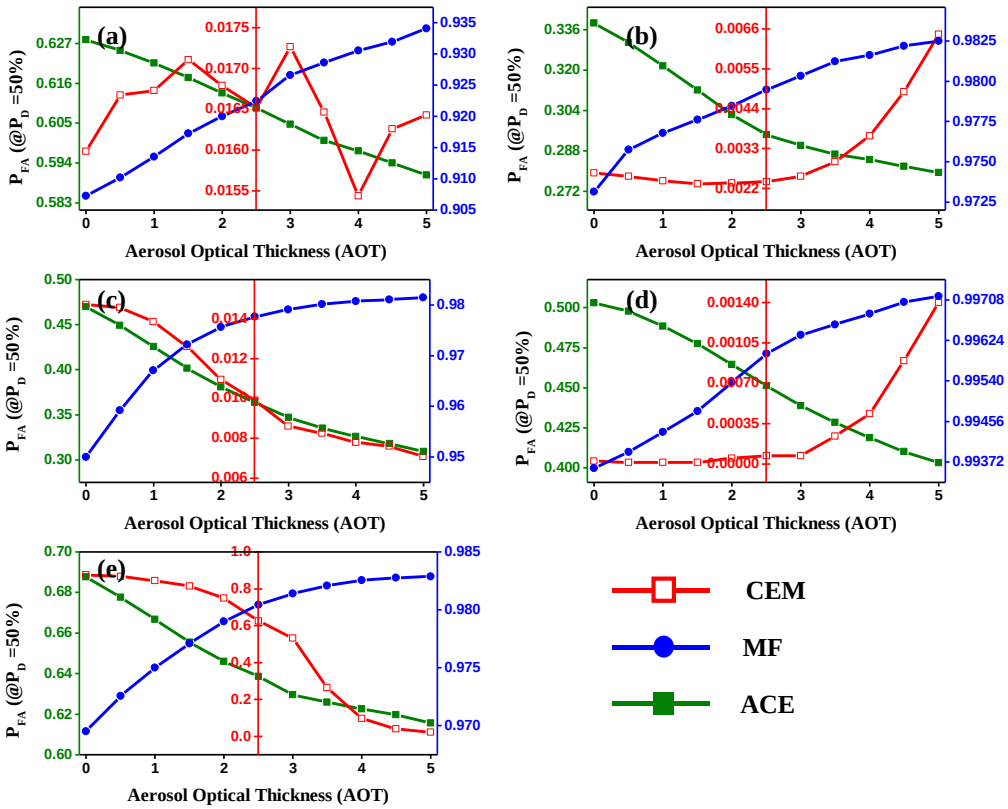

Figure 5.14: Space-borne imagery detection results. Illustrated are P_{FA} values when the $P_D = 50\%$ for the targets (a) N1G, (b) N2R, (c) C1W, (d) N3Y, and (e) N4B with simulated TOA target radiance spectra at different AOT values between 0 and 5 using the point-based target reflectance.

5.3.2.1.2 Detection statistics for pixel-based THI spectra

Results of target detection in the space-borne imagery, when using the pixel-based THI spectra as reference target spectra, are shown in Figure 5.15. The influence of AOT on the detection performance is evident for most of the targets. We observe a performance degradation pattern with increasing AOT values for all the detectors across all the target

materials. Unlike the previously observed low detection using point-based reference spectra for different AOT values, we now observe much-improved detection results using the pixel-based THI reference target spectra with lower FAs. Except for N3Y, all the target detectors can detect the targets with an acceptable P_{FA} (10^{-2}~10^{-6}) at lower values (e.g., in the range 0 – 1) of the AOT, which is a clear advantage of pixel-based THI spectra over point-based spectra. Specifically, for targets N1G and N2R, there is a gradual change in detectability performance with AOT variation. In the case of N1G, FAs are low ($10^{-2} \sim 10^{-3}$) for AOT $\leq$ 0.5; while for N2R, there is minimal performance degradation on changing AOT until 2.5, and all the three detectors detected both the targets. Detection of N4B by the MF and CEM at a low FA ($P_{FA} = 0 \sim 10^{-5}$, although for AOT≤1.5) is encouraging. In contrast to the poor detection of a dark target (Section 3.2.1.1), while using the point-based in-situ target spectra, detection results from the pixel-based THI target reference spectra are comparatively superior. This suggests that the acquisition of ground target reference spectra using an imaging spectroradiometer is a better alternative over the general point-based spectroradiometer, especially in difficult and inaccessible terrain.

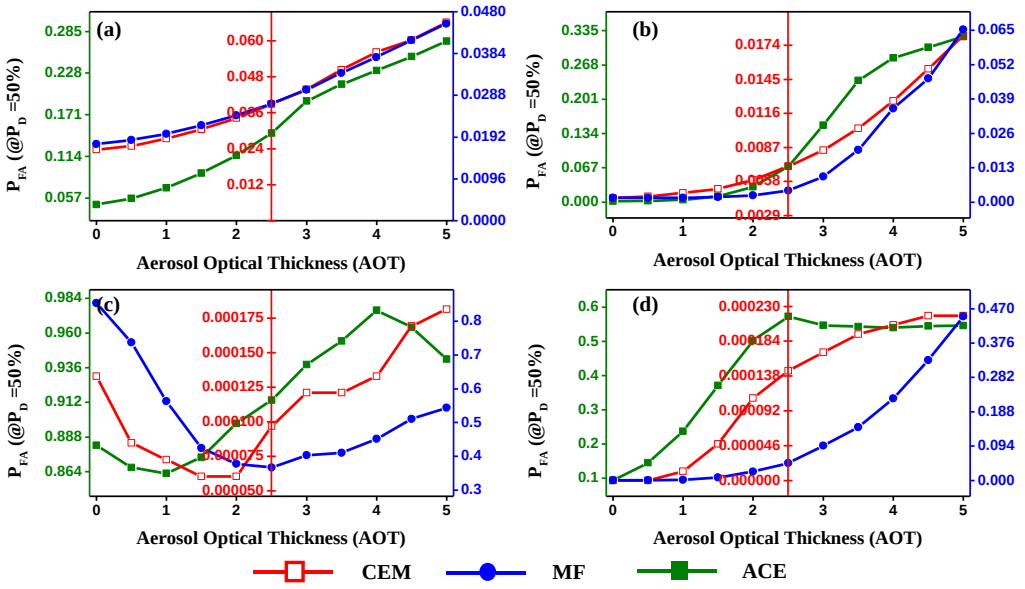

Figure 5.15: Space-borne imagery detection results. Illustrated are P_{FA} values when the $P_D = 50\%$ for the targets (a) N1G, (b) N2R, (c) N3Y, and (d) N4B with simulated TOA target radiance spectra at different AOT values between 0 and 5 using pixel-based THI target reflectance.

5.3.2.2 Target detection performance as a function of standard aerosol models for different standard atmospheric models at various AOT values

5.3.2.2.1 Detection statistics for point-based field spectra

We present the best-case scenario of detection performance in Figure 5.16, while the worst-case scenario, where all the targets are missed, is shown in Figure 5.17. As observed in the previous section 5.1.2.1.1, the detection of targets using the FM approach from a space-borne platform for point-based in-situ target reference remains a challenge. For N3Y, CEM's performance is satisfactory (Figure 5.15(b-h)), and at a lower value of AOT (0.48 and 0.89), no significant impact of atmospheric-aerosol models is observed.

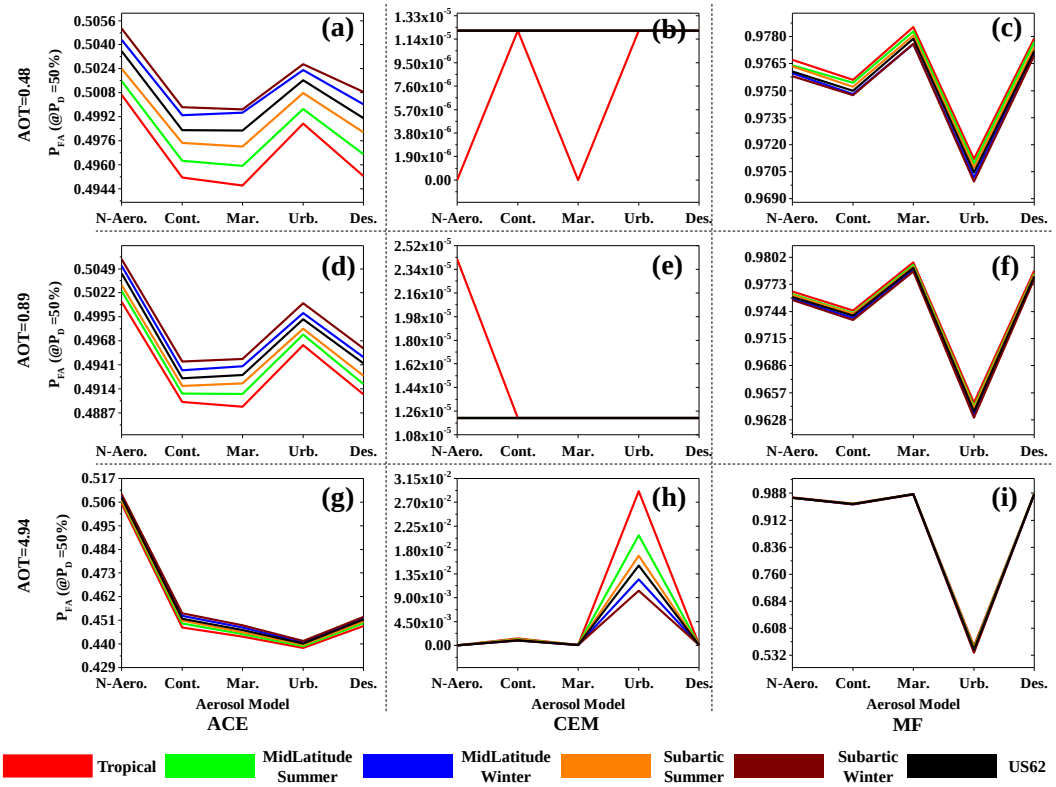

Figure 5.16: Space-borne imagery detection results. Illustrated are P_{FA} values when the $P_D = 50\%$ for the N3Y target with simulated TOA target radiance spectra at (a-c) AOT = 0.48, (d-f) AOT = 0.89, and (g-i) AOT = 4.94 for different standard aerosol models (i.e., x-axis) at given standard atmospheric models (i.e., coloured line) using the point-based target reflectance.

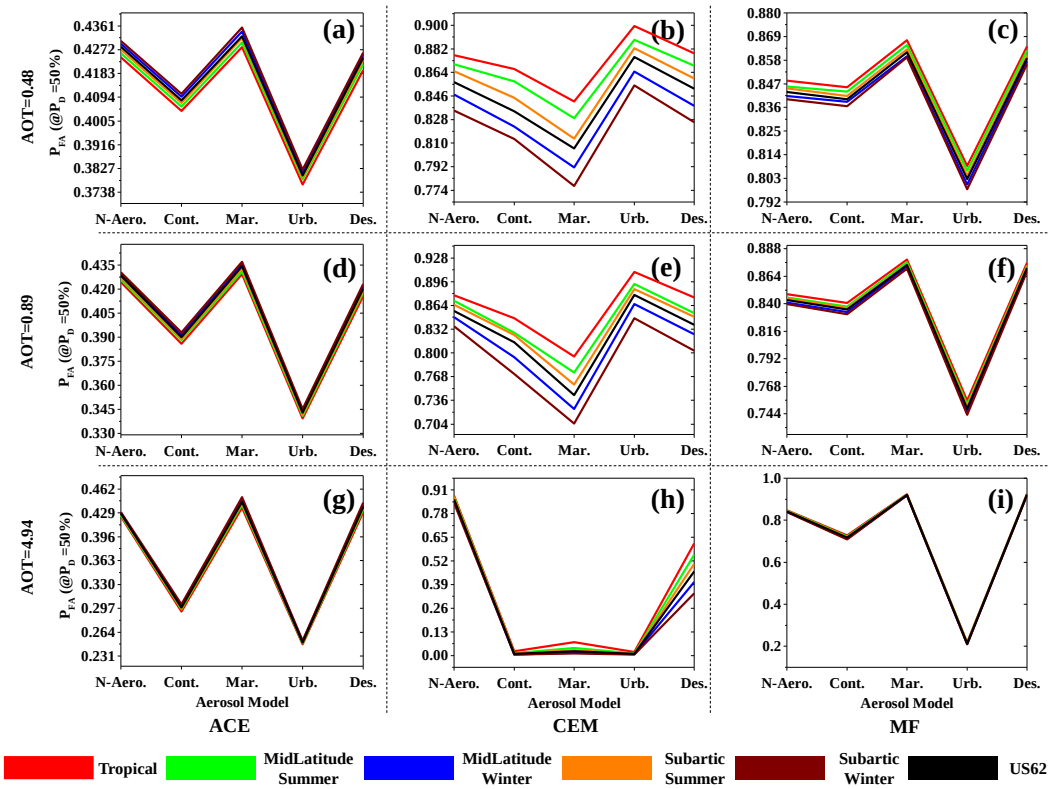

Figure 5.17: Space-borne imagery detection results. Illustrated are P_{FA} values when the $P_D = 50\%$ for the N4B target with simulated TOA target radiance spectra at (a-c) AOT = 0.48, (d-f) AOT = 0.89, and (g-i) AOT=4.94 for different standard aerosol models (i.e., x-axis) at given standard atmospheric models (i.e., coloured line) using the point-based target reflectance.

However, at AOT=4.94 (Figure 5.15(h)), we observe that, for all the atmospheric profiles, aerosol models such as continental, desert, and maritime yield a low number of FAs. In contrast, for the urban aerosol model, FAs depend upon the atmospheric profiles. Since most of the targets are not detectable by ACE and MF (high FA rate), the analysis of patterns in FAs for different combinations of atmospheric conditions and aerosol models becomes trivial.

5.3.2.2.1 Detection statistics for pixel-based THI spectra

We now present the best-case scenario related to detection performance in Figure 5.18 (observed for N2R), while the worst-case scenario is shown in Figure 5.19, where the spectral detectors miss N3Y. A combination of AOT values, aerosol models, and atmospheric models plays a crucial role in determining target detectors' performance for pixel-based input reference. As observed in Figure 5.18, although all the target

detectors detect N2R at lower AOT values with $P_{FA} \sim 10^{-3}$, the impact of aerosol models is evident. For instance, in the case of N2R detection by ACE (Figure 5.18(a)), the performance degradation between maritime aerosol and an urban aerosol model is 50%. Also, at AOT = 4.94, detection is most difficult by all detectors. Interestingly, for AOT $\leq$ 0.89, the pattern of FA change is almost identical for all detectors. As observed in previous sections, CEM is least affected by choice of aerosol models (~ 5-10% increase of FAs). Whereas other spectral detectors such as ACE and MF are substantially affected. As observed for the case of point-based target reference, detection of N3Y using radiance spectra with the FM approach did not yield a better result, especially for the ACE and MF detectors.

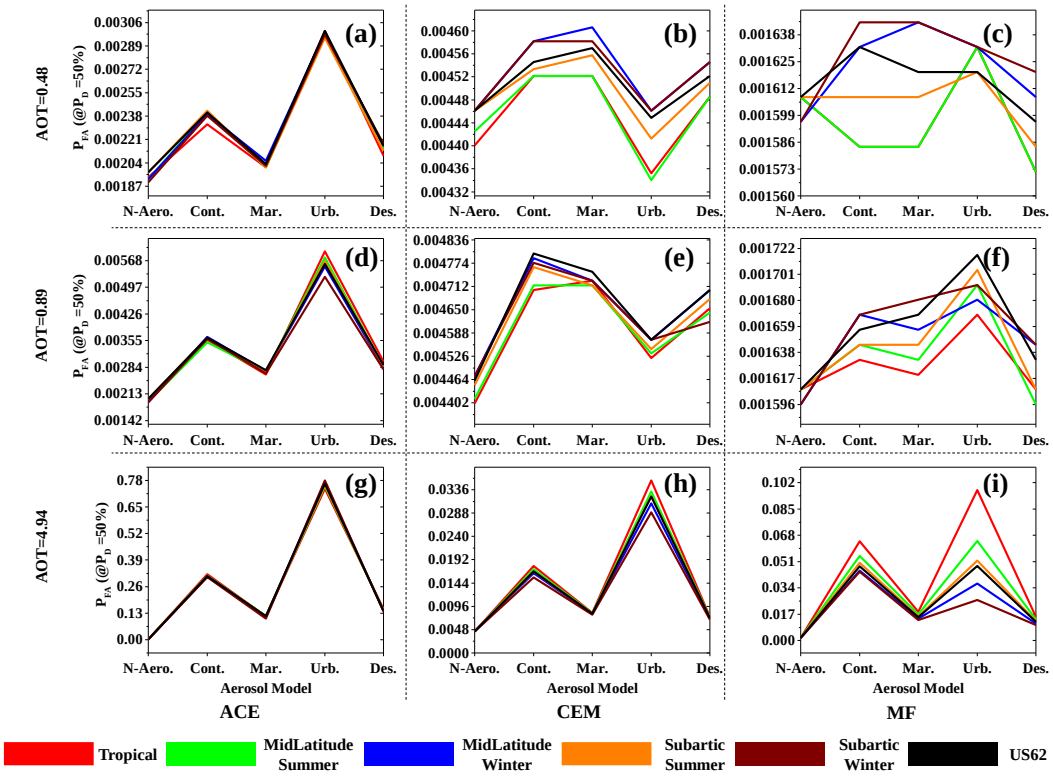

Figure 5.18: Space-borne imagery detection results. Illustrated are P_{FA} values when the $P_D = 50\%$ for the N2R target with simulated TOA target radiance spectra at (a-c) AOT = 0.48, (d-f) AOT = 0.89, and (g-i) AOT = 4.94 for different standard aerosol models (i.e., x-axis) at given standard atmospheric models (i.e., coloured line) using pixel-based THI target spectra.

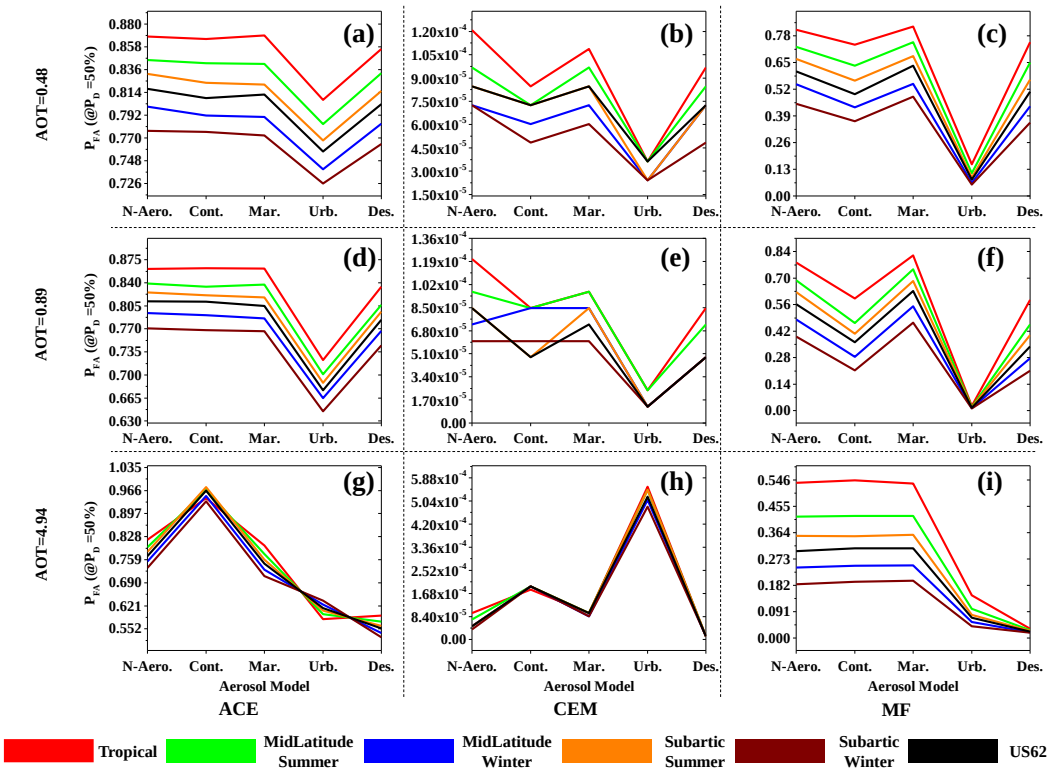

Figure 5.19: Space-borne imagery detection results. Illustrated are P_{FA} values when the $P_D = 50\%$ for the N3Y target with simulated TOA target radiance spectra at (a-c) AOT = 0.48, (d-f) AOT = 0.89, and (g-i) AOT = 4.94 for different standard aerosol models (i.e., x-axis) at given standard atmospheric models (i.e., coloured line) using pixel-based THI target spectra.

5.3.3 Quantitative spectral similarity analysis of simulated Vs. image spectra

The spectral similarity analysis between the target image spectrum from airborne imagery and the respective point-based in-situ reference spectrum is presented in Figure 5.20 and 5.21. The result provided in this section is limited to the airborne imagery with AOT=0.48 and 0.89, as sufficient inferences can be drawn about the underlying physical state of the atmospheric conditions, and the finding can be generalized for other cases as well. As evident in Figure 5.19 and 5.20, we can identify the atmospheric conditions i.e., probable aerosol models (i.e., x-axis) for a given atmospheric profile (coloured lines) which would yield successful detection results in unknown atmospheric conditions. For example, we find the Tropical and Midlatitude Summer atmospheric profile in the present experimental setup, with either the Continental or Maritime aerosol model, the best suited for the given experimental site. As observed from the results in Section 3.1.2, indeed, the Tropical atmospheric profile with the

Continental aerosol model does provide better results compared to other combinations of models. Furthermore, we find the spectral matching different across the targets, suggesting that there is an effect related to the spatial neighborhood, which is separate from parameters related to the atmosphere.

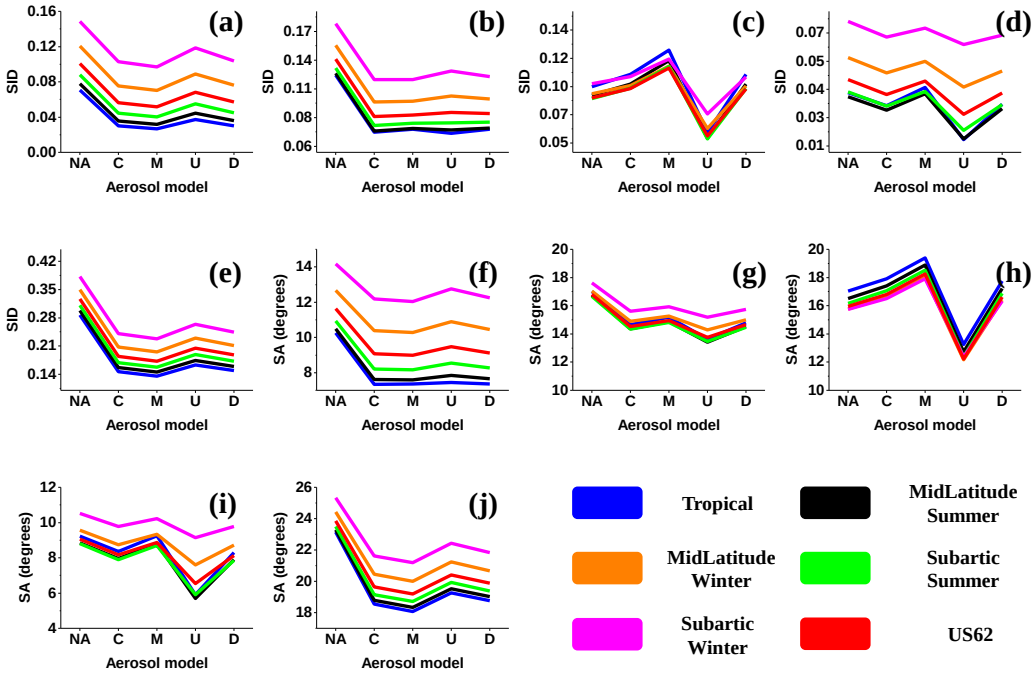

Figure 5.20: Spectral similarity score for the point-based in-situ target reference target spectra and the corresponding image spectra for (a, f, k, p) N1G, (b, g, l, q) N2R, (c, h, m, r) C1W, (d, i, n, s) N3Y, and (e, j, o, t) N4B targets at (a-j) AOT = 0.48 for different atmospheric (i.e., coloured lines) and aerosol models (i.e. x-axis where NA= no aerosol, C= Continental, M=Maritime, U=Urban and D= Desert).

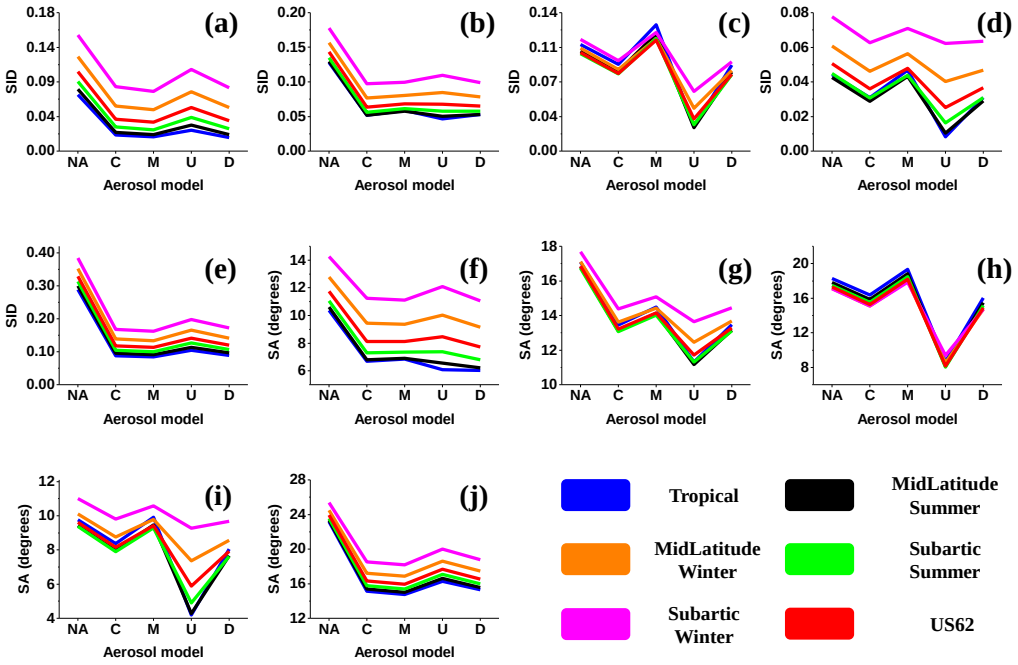

Figure 5.21: Spectral similarity score for the point-based in-situ target reference target spectra and the corresponding image spectra for (a, f, k, p) N1G, (b, g, l, q) N2R, (c, h, m, r) C1W, (d, i, n, s) N3Y, and (e, j, o, t) N4B targets at (a-j) AOT = 0.89 for different atmospheric (i.e., coloured lines) and aerosol models (i.e. x-axis where NA= no aerosol, C= Continental, M=Maritime, U=Urban and D= Desert).

5.4 Discussion

On-board methods for problems ranging from classification, anomaly detection, unmixing to target detection, etc., are projected to be future endeavours in the field of remote sensing. FM approach, operating in the radiance mode, helps to design an on-board computational framework for atmospheric effect with minimal time lag for realizing remote sensing based real-time target detection system. Spectral target detection by its nature involves sparsely populated pixels of the imagery, which increases the chance of a target miss with even a slight miscalculation of atmospheric parameters. Few seminal studies on target detection have shown the FM approach as a potential solution for a computationally efficient framework, although the effect of atmospheric variables on detection performance has not been taken into account. A study by Matteoli, Ientilucci, and Kerekes (2010) has laid out a detailed analysis of the

computational and operational aspects of the FM approach for target detection. They simulated different radiance spectra (81 in total) for various geometric and illumination parameters, but atmospheric variability parameters such as atmospheric models and aerosol models were not tested or evaluated. Axelsson et al. (2016) implemented the FM method for target detection but used in-scene information rather than the physics-based RT models to derive target information. Also, the dataset used in that study had a limited spectral channel range (400-1000 nm) acquired from an altitude of only1000 m, which inhibits observable effects of atmospheric variables on target detection performance. In this chapter, we have presented the FM approach to account for atmosphere-induced target uncertainty and variability in multi-platform target detection data, which to the best of our knowledge, has not been reported in the literature. We have also presented results from a hypothetical perspective where the spectral knowledge of a target in one given space-time frame can be transferred for detection in a different space-time framework. This involves two different sets of atmospheric components, and as a result, a mismatch of atmospheric parameters may hamper the detectability of the target. The experimental findings from this chapter could be used for drawing important inferences and to gain a comprehensive insight into the extent and nature of the atmosphere influences and impacts parameter mismatch and ultimately affects target detection performance.

5.4.1 Influence of spectral variation caused by varying AOT assumption on detection performance

AOT, which corresponds to columnar visibility, is among several atmospheric variables that could impact the sensor reaching radiance. Several studies have been conducted to establish the uncertainty caused by AOT while estimating biophysical parameters (Gillingham et al., 2013; Marcello et al., 2016). Most of the reported studies related to the reflectance uncertainty caused by AOT are focused on objects covering a large portion of the image (a class such as vegetation or forest). We found that there is no reported study on its impact on engineered material detection. Since AOT is sensitive to wavelength, absorption feature, surface albedo (Bhatia et al., 2015), and pixel to pixel differences in AOT levels (i.e., spatial variability)(Wilson et al., 2015), it is natural to expect that these effects would be reflected in target detection performance.

For the most efficient target detector (CEM) in detection from airborne imagery (Figure 5.5, section 5.3.1.1.1) for point-based in-situ target reference, the overall variation in detection performance is 2% -15% across all the targets for the simulated spectra at AOTs ≤ 2.5. For spectral detectors, MF and ACE, where targets can be deemed as detected (with lower FAs), the variation in detection range is found to be between 10% - 90% for most of the targets. A similar trend is observed in detection from space-borne imagery for point-based in-situ target reference. However, for pixel-based target reference, detection from airborne imagery shows substantial variation in detection with variation in AOT levels (e.g., ACE for N1G varies by 200% with AOT≤ 2.5). The variation is linear with a change in AOT levels for detection from space-borne imagery for pixel-based target reference.

Overall, detection performance and FAs are found to vary moderately across all the targets, albeit with different scales. Results indicate that the AOT mismatch effect yields different detection results for targets having different surface properties. Although the given targets in this experiment vary predominantly only in the visible portion of the EM spectrum, the varying effects of AOT mismatch across the targets suggest an involvement related to the background pixels and an AOT influence which seems to impact overall detection performance.

5.4.2 Influence of atmospheric model assumption and respective mismatch on target detection performance

Apart from the AOT, the other two critical parameters seen in several radiative transfer codes are the choice of atmospheric, and aerosol models. Typically, atmospheric models in 6S are modelled on the basis of fixed columnar profiles, which are pre-computed using standard models such as that by Goody and Yung (1995), Malkmus (1967), and McClatchey et al. (1971) for estimating gaseous transmittance, columnar water vapour, temperature, pressure, and ozone concentrations as a function of altitude. Similarly, aerosol models are formulated based on models by Lenoble (1985), D'Almeida et al. (1991). These models estimate the macroscopic properties of EM signal propagation in the atmosphere, which is beyond the scope of this chapter. For these reasons, they are often treated like a "black box" (Bhatia, 2018). However, since

these global models are widely used in remote sensing for atmospheric compensation and represent the atmospheric state in a given space-time, we have investigated their impact on target detection in this chapter. Results in section 5.3.1.2.1 for detection from airborne imagery using the point-based in-situ target reference indicate that the overall detection and levels of FAs are predominantly determined by choice of atmospheric profile. A mismatch of atmospheric profile can potentially lead to detection failure. We have noticed that for a given atmospheric profile (e.g., Tropical), there is an observable pattern related to the aerosol models on the number of FAs, which indicates the need for estimation of local aerosol models in all automated target detection frameworks. Interestingly, spectral target detectors such as ACE and MF have yielded low FAs for a tropical atmospheric profile. In contrast, the CEM detector offers a better result for the Subarctic winter atmospheric profile. This insinuates that the target detection results can be different across various detection algorithms for different atmospheric state variables.

We suggest that a detection framework for applications utilizing the FM approach for target detection must be designed keeping in mind the nature of the detection algorithm and its sensitivity to atmospheric state variables. A pixel-based target reference in airborne derived targets indicated that detection of dark targets (i.e., targets with lower reflection intensity) is a challenge and is prone to be influenced by choice of atmospheric parameters. On the other hand, although the detection is low for space-borne imagery using both a point-based and pixel-based target reference, the pattern observed in the levels of FAs was concurrent with the observations in Section 5.3.1.2 for the for the ACE and MF target detectors.

5.5 Chapter Conclusions

There have been considerable efforts to develop signal processing-based detection algorithms in this field. However, to a lesser degree, the underlying physical phenomena have largely been overlooked. The trivialization of the electromagnetic signal propagation model, ignoring the subtle atmospheric process, can produce ambiguous target detection results from various remote sensing platforms. In this chapter, assessment of hyperspectral target detection from a radiative transfer

perspective, further extending the FM approach for target detection to a multi-platform (airborne - space-borne) target detection setup, is presented. Accepting the notion that FM approach is computationally inexpensive, we recommend the FM approach for all kinds of on-board processing methods for detecting non-critical targets (i.e., environmental pollution surveillance, infrastructure build-up in strategic areas, unauthorized construction in protected forest areas, geochemical exploration, mineral prospecting, etc.).

From an atmospheric parameter modelling perspective, spectral target detection is susceptible to AOT, atmospheric profile, and aerosol model. AOT is found to be the most dominant factor among the parameters considered, having substantial implications on the detectability of targets. At a given AOT, the choice of atmospheric and aerosol profiles has a bearing on the levels of FAs. The wrong choice of atmospheric models can lead to a high rate of FAs. The variations in target detection due to AOT can be reduced to a moderate degree by choosing an appropriate detection algorithm (e.g., CEM for the present application). The validity of the hypothesis that targets can be detected by transferring target spectral knowledge from a known atmospheric state to an unknown state is case-specific. We found that a lack of a priori knowledge on the exact atmospheric condition can limit the target detection process. Tackling such problems requires a learning approach to model the targets that account for the atmospheric processes' induced spectral variability.

Two significant findings from this research, apart from the atmospheric perspective on target detection, are establishing the efficacy of the pixel-based in-situ target reference and the potential of detection of engineered targets from space-borne platforms. We have observed that the ground-based imaging spectroscopy method of target reference spectra acquisition has performed well with detection from space-borne imagery. The FM approach for space-borne imagery has yielded unambiguous detection of several targets in the experiment, which we find very encouraging for developing automatic satellite-based spectral target detection frameworks. We believe that the formulation of more experimental datasets and additional testing at different sites would further enhance our understanding of the target detection process and its intricate relation to atmospheric influences.

CHAPTER 6

SUMMARY, CONCLUSIONS, AND FUTURE DIRECTIONS

Prelude: This chapter presents an overall summary of the main conclusions and findings of the research activities carried out as part of this doctoral study. Further, contributions of this thesis in the context of spectral target detection in dynamic atmospheric conditions are presented. Finally, recommendations and directions for future research in this area are highlighted in this chapter.

6.1 Summary of the Chapters

Theoretically, algorithms for target detection using various simulated and ideal imagery scenarios shows substantial feasibility. On the other hand, realistic scenarios with complex target neighbourhoods and dynamic atmospheric conditions make it challenging to detect engineered targets. The performance from detection algorithms is a function of numerous variables such as atmospheric path effects, sensor properties, and target-background dynamics. This thesis has assessed the detectability of engineered targets in a multi-platform setup and quantitatively evaluated the influence of the various atmospheric parameter on spectral target detection. The pursuance of thesis objectives has led to the formulation of a region-sensitive open-end atmospheric correction model and novel benchmark dataset crucial for evaluating target detection performance of various algorithms.

The summary of the thesis is presented below chapter-wise.

Chapter 3: A open-ended region-sensitive atmospheric correction method named FACT was developed for various optical sensors and platforms. The chapter has laid out the methodological framework for the development of 6S based open-source

atmospheric correction method. Various techniques for the estimation of atmospheric parameters such as CWV and AOT from the satellite/airborne imagery were explored and have been successfully adapted for the FACT atmospheric correction method. A LUT approach was adapted for generating correction coefficients from the 6S RT code for various input parameters' combinations. Further, FACT has been exhaustively evaluated using various spatio-spectral statistical error measures against standard atmospheric correction methods such as FLAASH across various multispectral and hyperspectral sensors. The FACT yielded comparatively better results for the space-borne sensors than the airborne hyperspectral sensors, indicating the need for more robust atmospheric parameter estimation techniques. To produce more robust surface reflectance pertaining to regional scales, new atmospheric profiles are added to the FACT. The FACT offers a viable atmospheric correction alternative to commercially off-the-shelf atmospheric correction methods.

Chapter 4: In this chapter, the experimental setup for a multi-platform remote sensing benchmark dataset for the quantitative assessment of the spectral target detection was elaborated. Target detection performance as a function of sensor, platform, source of in-situ target spectral information, target-background dynamics, and algorithm was studied. Various statistical and subspace detection algorithms were applied on the benchmark dataset for the detection of targets, considering the different sources of reference target spectra, background, and the spectral continuity across the platforms. The accuracy of detection, is substantially influenced by the source of reference spectra and it is not true that ground-based point spectra offers best results. In addition, local background influences the confidence of target detectability, although not a deciding factor. Imaging spectroscopy-based in-situ target reference yields detection results at par with point-based non-imaging spectroscopic instruments, suggesting that a ground-based hyperspectral imager can be used for rapid acquisition of target reference spectra. The results also indicate the potential usage of satellite imagery-based target detection, although further experiments are required to bolster the generalization.

Chapter 5: We have extended the FM approach for target detection for the multi-platform target detection benchmark dataset formulated in Chapter 4. Some of the critical atmospheric parameters such as AOT, standard atmospheric profiles, and standard aerosol models are considered to quantify their influence on sensor reaching radiance signal. The targets acquired from platforms with different operational altitudes (airborne and space-borne) provides two different sets of concomitant atmospheric conditions, enabling us to assess atmosphere-induced uncertainty in target detection in its entirety. We have formulated the radiance spectral library by simulating TOA radiance spectra using the 6S RTM. Considering two cases of target radiance spectra simulation corresponding to a grid of different AOT values, atmospheric and aerosol profiles target the detection has been carried out using multiple target detection algorithms. Results indicate that knowledge based spectral targets can be detected in remote sensing data under different atmospheric model scenario using FM approach. Change in the magnitude of AOT across atmospheric models leads to decision-changing implications in the target detection modelling. The selection of a wrong atmospheric profile can potentially aggravate the numbers of FAs produced by a detection algorithm.

6.2 Major Contributions

The major contribution of this thesis, researching on spectral target detection and atmospheric modeling methods for detecting engineered targets, are listed below.

- Development of a region sensitive atmospheric correction model for hyperspectral and multi-spectra remote sensing sensors.

- Establishment of multi-platform optical remote sensing benchmark dataset for target detection in complex imaging environment.

- Analyses of target-background interactions influence on detection performance

- Quantification of the influence of atmospheric parameter on detection performance of engineered materials.

6.3 Recommendations for Future Research

We present some of the recommendations and directions of future research to extend and enhance the finding of the studies carried out in this thesis.

- At present, the developed atmospheric correction method FACT supports regional atmospheric models. Atmospheric models incorporating local aerosol models based on AERONET data can be included to make the atmospheric correction models sensitive to fine scale regional parameters.

- Complex target detection scene in this thesis can be used to extend the idea of setting up more experimental dataset for an exhaustive evaluation of detection algorithms.

- Accommodating neighborhood/background effect in target detection has been done using global background statistics. Using the concept of local context/background of a target and incorporating its effect in detection algorithm can be an interesting future work.

- The effect of atmospheric processes on spectral target detection can be further evaluated and used to formulate atmospherically invariant target detection algorithms.

- Target detection methods predominantly use statistical or subspace-based methods. Use of evolving machine learning techniques for target detection can also be tested.

- Close range hyperspectral imagery-based target detection is one of the challenging areas and experimental setting used in this thesis can be extended to formulate more UAVs/THI based benchmark dataset.

REFERENCES

Acito, N., Matteoli, S., Rossi, A., Diani, M., & Corsini, G. (2016). Hyperspectral airborne "Viareggio 2013 Trial" data collection for detection algorithm assessment. *IEEE Journal of Selected Topics in Applied Earth Observations and Remote Sensing*, *9*(6), 2365–2376.

Adão, T., Hruška, J., Pádua, L., Bessa, J., Peres, E., Morais, R., & Sousa, J. J. (2017). Hyperspectral imaging: A review on UAV-based sensors, data processing and applications for agriculture and forestry. *Remote Sensing*, *9*(11), 1110.

Adler-Golden, S., Berk, A., Bernstein, L. S., Richtsmeier, S., Acharya, P. K., Matthew, M. W., Anderson, G. P., Allred, C. L., Jeong, L. S., & Chetwynd, J. H. (1998). FLAASH, a MODTRAN4 atmospheric correction package for hyperspectral data retrievals and simulations. In *Summaries of the Seventh JPL Airborne Earth Science Workshop* (Vol. 1, pp. 9–14).

Agapiou, A., Hadjimitsis, D. G., Papoutsa, C., Alexakis, D. D., & Papadavid, G. (2011a). The importance of accounting for atmospheric effects in the application of NDVI and interpretation of satellite imagery supporting archaeological research: The case studies of Palaepaphos and Nea Paphos sites in Cyprus. *Remote Sensing*, *3*(12), 2605–2629.

Agapiou, A., Hadjimitsis, D. G., Papoutsa, C., Alexakis, D. D., & Papadavid, G. (2011b). The Importance of Accounting for Atmospheric Effects in the Application of NDVI and Interpretation of Satellite Imagery Supporting Archaeological Research: The Case Studies of Palaepaphos and Nea Paphos Sites in Cyprus. *Remote Sensing*, *3*(12), 2605–2629. https://doi.org/10.3390/rs3122605

Archer, C., Morgenstern, J., & Musallam, R. N. (2013). Improved target recognition with live atmospheric correction. In *Algorithms and Technologies for*

Multispectral, Hyperspectral, and Ultraspectral Imagery: Vol. XIX (Vol. 8743 (p. 87430). International Society for Optics and Photonics.

Ashton, E. A., & Schaum, A. (1998). Algorithms for the detection of sub-pixel targets in multispectral imagery. *Photogrammetric Engineering & Remote Sensing*, *64*(7), 723–731.

Axelsson, M., Friman, O., Haavardsholm, T. V., & Renhorn, I. (2016). Target detection in hyperspectral imagery using forward modeling and in-scene information. *ISPRS Journal of Photogrammetry and Remote Sensing*, *119*, 124–134.

Baldridge, A. M., Hook, S. J., Grove, C. I., & Rivera, G. (2009). The ASTER spectral library version 2.0. *Remote Sensing of Environment*, *113*(4), 711–715.

Baumgardner, M. F., Biehl, L. L., & Landgrebe, D. A. (2015). 220 band aviris hyperspectral image data set: June 12, 1992 indian pine test site 3. *Purdue University Research Repository*, *10*, 7 991.

Bentley, J. L. (1975). Multidimensional binary search trees used for associative searching. *Communications of the ACM*, *18*(9), 509–517.

Bhatia, N. (2018). *Uncertainty Propagation of Atmospheric Correction Parameters*. University of Twente.

Bhatia, N., Tolpekin, V. A., Reusen, I., Sterckx, S., Biesemans, J., & Stein, A. (2015). Sensitivity of Reflectance to Water Vapor and Aerosol Optical Thickness. *IEEE Journal of Selected Topics in Applied Earth Observations and Remote Sensing*, *8*(6), 3199–3208. https://doi.org/10.1109/JSTARS.2015.2425954

Bhatia, N., Tolpekin, V. A., Stein, A., & Reusen, I. (2018). Estimation of AOD Under Uncertainty: An Approach for Hyperspectral Airborne Data. *Remote Sensing*, *10*(6), 947. https://doi.org/10.3390/rs10060947

Bhattacharya, B. K., Green, R. O., Rao, S., Saxena, M., Sharma, S., Kumar, K. A., Srinivasulu, P., Sharma, S., Dhar, D., Bandyopadhyay, S., & Bhatwadekar, S. (2019). An overview of AVIRIS-NG airborne hyperspectral science campaign over India. *Current Science*, *116*, 1082–1088.

Bishop, C. A., Liu, J. G., & Mason, P. J. (2011). Hyperspectral remote sensing for mineral exploration in Pulang, Yunnan Province, China. *International Journal of Remote Sensing*, *32*(9), 2409–2426.

Borel, C. C., & Schlaepfer, D. (1996). Atmospheric Pre–Corrected Differential Absorption Techniques To Retrieve Columnar Water Vapor: Theory and Simulations. In *6th Annual JPL Airborne Earth Science Workshop, Jet Propulsion Laboratory* (pp. 13–21).

Brando, V. E., & Dekker, A. G. (2003). Satellite hyperspectral remote sensing for estimating estuarine and coastal water quality. *IEEE Transactions on Geoscience and Remote Sensing*, *41*(6), 1378–1387.

Briottet, X., Boucher, Y., Dimmeler, A., Malaplate, A., Cini, A., Diani, M., Bekman, H. H. P. T., Schwering, P., Skauli, T., Kasen, I., & Renhorn, I. (2006). Military applications of hyperspectral imagery. In *Targets and Backgrounds XII: Characterization and Representation* (Vol. 6239, p. 62390). International Society for Optics and Photonics.

Bru, D., Lubac, B., Normandin, C., Robinet, A., Leconte, M., Hagolle, O., Martiny, N., & Jamet, C. (2017). Atmospheric correction of multi-spectral littoral images using a PHOTONS/AERONET-based regional aerosol model. *Remote Sensing*, *9*(8), 814.

Bue, B. D., Thompson, D. R., Eastwood, M. L., Green, R. O., Gao, B. C., Keymeulen, D., Sarture, C. M., Mazer, A. S., & Luong, H. H. (2015). Real-Time Atmospheric Correction of AVIRIS-NG Imagery. *IEEE Trans. Geoscience and Remote Sensing*, *53*(12), 6419–6428.

Camps-Valls, G., Tuia, D., Gomez-Chova, L., Jimenez, S., & Malo, J. (2011). *Remote Sensing Image Processing. Synthesis Lectures on Image, Video, and Multimedia Processing.* (BOOK). Infoscience; Morgan and Claypool. https://infoscience.epfl.ch/record/174404

Carrère, V., & Conel, J. E. (1993). Recovery of atmospheric water vapor total column abundance from imaging spectrometer data around 940 nm—Sensitivity analysis and application to airborne visible/infrared imaging spectrometer (AVIRIS) data. *Remote Sensing of Environment*, *44*(2–3), 179–204.

Casey, J. T., & Kerekes, J. P. (2009). Misregistration impacts on hyperspectral target detection. *Journal of Applied Remote Sensing*, *3*(1), 033513.

Chang, C. I. (2000a). An information-theoretic approach to spectral variability, similarity, and discrimination for hyperspectral image analysis. *IEEE Transactions on Information Theory*, *46*(5), 1927–1932.

Chang, C. I. (2000b). An information-theoretic approach to spectral variability, similarity, and discrimination for hyperspectral image analysis. *IEEE Transactions on Information Theory*, *46*(5), 1927–1932.

Chang, C. I. (2003). *Hyperspectral imaging: Techniques for spectral detection and classification* (Vol. 1). Springer Science & Business Media.

Chen, S. Y., Lin, C., Chuang, S. J., & Kao, Z. Y. (2019). Weighted Background Suppression Target Detection Using Sparse Image Enhancement Technique for Newly Grown Tree Leaves. *Remote Sensing*, *11*(9), 1081.

Cheng, G., & Han, J. (2016). A survey on object detection in optical remote sensing images. *ISPRS Journal of Photogrammetry and Remote Sensing*, *117*, 11–28.

Cohen, Y., August, Y., Blumberg, D. G., & Rotman, S. R. (2012a). Evaluating Subpixel Target Detection Algorithms in Hyperspectral Imagery. *Journal of Electrical and Computer Engineering*, *2012*, 1–15. https://doi.org/10.1155/2012/103286

Cohen, Y., August, Y., Blumberg, D. G., & Rotman, S. R. (2012b). Evaluating subpixel target detection algorithms in hyperspectral imagery. *Journal of Electrical and Computer Engineering*.

Conel, J. E., Green, R. O., Vane, G., Bruegge, C. J., Alley, R. E., & Curtiss, B. J. (1987). *AIS-2 radiometry and a comparison of methods for the recovery of ground reflectance*.

D'Almeida, G. A., Koepke, P., & Shettle, E. P. (1991). *Atmospheric aerosols: Global climatology and radiative characteristics*. A Deepak Pub.

Dobigeon, N., Tits, L., Somers, B., Altmann, Y., & Coppin, P. (2014). A Comparison of Nonlinear Mixing Models for Vegetated Areas Using Simulated and Real Hyperspectral Data. *IEEE Journal of Selected Topics in Applied Earth Observations and Remote Sensing*, *7*(6), 1869–1878. https://doi.org/10.1109/JSTARS.2014.2328872

Dos Reis Salles, R., Souza Filho, C. R., Cudahy, T., Vicente, L. E., & Monteiro, L. V. S. (2017). Hyperspectral remote sensing applied to uranium exploration: A case study at the Mary Kathleen metamorphic-hydrothermal U-REE deposit, NW, Queensland, Australia. *Journal of Geochemical Exploration*, *179*, 36–50.

Du, B., & Zhang, L. (2014). Target detection based on a dynamic subspace. *Pattern Recognition*, *47*(1), 344–358. https://doi.org/10.1016/j.patcog.2013.07.005

Duran, O., & Petrou, M. (2007). A Time-Efficient Method for Anomaly Detection in Hyperspectral Images. *IEEE Transactions on Geoscience and Remote Sensing*, *45*(12), 3894–3904. https://doi.org/10.1109/TGRS.2007.909205

Eismann, M. T. (2012). *Hyperspectral remote sensing*. SPIE.

Fawcett, T. (2006). An introduction to ROC analysis. *Pattern Recognition Letters*, *27*(8), 861–874. https://doi.org/10.1016/j.patrec.2005.10.010

Field Spectroscopy Guide with SVC i-series Spectroradiometers. (2010). https://www.spectravista.com/wp-content/uploads/2019/12/SVC-Field-Spectroscopy-Guide-Rev-1-2019-10-22.pdf

Gao, B. C., Davis, C., & Goetz, A. (2006). A review of atmospheric correction techniques for hyperspectral remote sensing of land surfaces and ocean colour. *Geoscience and Remote Sensing Symposium, 2006. IGARSS 2006. IEEE International Conference On*, 1979–1981.

Gao, B. C., Heidebrecht, K. B., & Goetz, A. F. (1993). Derivation of scaled surface reflectances from AVIRIS data. *Remote Sensing of Environment*, *44*(2–3), 165–178.

Gao, B. C., Montes, M. J., Davis, C. O., & Goetz, A. F. (2009). Atmospheric correction algorithms for hyperspectral remote sensing data of land and ocean. *Remote Sensing of Environment*, *113*, 17–24.

Gholizadeh, M. H., Melesse, A. M., & Reddi, L. (2016). A comprehensive review on water quality parameters estimation using remote sensing techniques. *Sensors*, *16*(8).

Gilabert, M. A., Conese, C., & Maselli, F. (1994). An atmospheric correction method for the automatic retrieval of surface reflectances from TM images. *International Journal of Remote Sensing*, *15*(10), 2065–2086.

Gillingham, S. S., Flood, N., & Gill, T. K. (2013). On determining appropriate aerosol optical depth values for atmospheric correction of satellite imagery for biophysical parameter retrieval: Requirements and limitations under Australian conditions. *International Journal of Remote Sensing*, *34*(6), 2089–2100.

Goa, P. E., Skauli, T., Kasen, I., Haavardsholm, T. V., & Rodningsby, A. (2004). *Physical subspace models for invariant material identification: Subspace composition and detection performance* (L. Bruzzone, Ed.; p. 203). https://doi.org/10.1117/12.565612

Goodenough, A. A., & Brown, S. D. (2012). DIRSIG 5: Core design and implementation. In *Algorithms and Technologies for Multispectral, Hyperspectral, and Ultraspectral Imagery: Vol. XVIII (Vol. 8390* (p. 83900). International Society for Optics and Photonics.

Goody, R. M., & Yung, Y. L. (1995). *Atmospheric radiation: Theoretical basis*. Oxford university press.

Griffin, M. K., & Burke, H. H. K. (2003). Compensation of hyperspectral data for atmospheric effects. *Lincoln Laboratory Journal*, *14*(1), 29–54.

Gruninger, J. H., Ratkowski, A. J., & Hoke, M. L. (2004). *The sequential maximum angle convex cone (SMACC) endmember model. Algorithms and technologies for multispectral, hyperspectral, and ultraspectral imagery: Vol. X (Vol. 5425*. International Society for Optics and Photonics.

Guanter, L. (2006). New algorithms for atmospheric correction and retrieval of biophysical parameters in Earth Observation. In *Application to ENVISAT/MERIS data. Valencia–Estudi General* (pp. 86–94).

Guanter, L., Alonso, L., & Moreno, J. (2007). In *CHRIS Proba Atmospheric Correction Module. Algorithm Theoretical Basis Document; ESA ESRIN Contract* (p. 20442).

Gyaneshwar, D., & Nidamanuri, R. R. (2020). A real-time FPGA accelerated stream processing for hyperspectral image classification. *Geocarto International*, 1–18.

Harsanyi, J. C., & Chang, C. I. (1994). Hyperspectral image classification and dimensionality reduction: An orthogonal subspace projection approach. *IEEE Transactions on Geoscience and Remote Sensing*, *32*(4), 779–785.

Healey, G., & Slater, D. (1999). Models and methods for automated material identification in hyperspectral imagery acquired under unknown illumination and atmospheric conditions. *IEEE Transactions on Geoscience and Remote Sensing*, *37*(6), 2706–2717.

Hill, J., & Sturm, B. (1991). Radiometric correction of multitemporal Thematic Mapper data for use in agricultural land-cover classification and vegetation monitoring. *International Journal of Remote Sensing*, *12*(7), 1471–1491.

Hoff, L. E., Zeidler, J. R., & Yerkes, C. R. (1992). Adaptive multispectral image processing for the detection of targets in terrain clutter. In *Signal and Data Processing of Small Targets 1992* (Vol. 1698, pp. 100–115). International Society for Optics and Photonics.

Hook, S. J., & Rast, M. (1990). Mineralogic mapping using airborne visible infrared imaging spectrometer (aviris), shortwave infrared (swir) data acquired over cuprite, Nevada. *Proceedings of the Second Airborne Visible Infrared Imaging Spectrometer (AVIRIS) Workshop, JPL Publication*, 90–54.

Hou, Y., Zhang, Y., Yao, L., Liu, X., & Wang, F. (2016). Mineral target detection based on MSCPE_BSE in hyperspectral image. *Geoscience and Remote Sensing Symposium (IGARSS), 2016 IEEE International*, 1614–1617.

Hou, Y., Zhu, W., Wang, E., & Zhang, Y. (2019). A Hyperspectral Subspace Target Detection Method Based on AMUSE. *International Journal of Pattern Recognition and Artificial Intelligence*, *33*(12), 1954032. https://doi.org/10.1142/S0218001419540326

Hu, S., Zhang, L., Baig, M. H. A., & Tong, Q. (2012). Using MODTRAN4 to build up a general look-up-table database for the atmospheric correction of hyperspectral imagery. *Geoscience and Remote Sensing Symposium (IGARSS), 2012 IEEE International*, 2458–2461.

Hu, Y., Liu, L., Liu, L., Peng, D., Jiao, Q., & Zhang, H. (2014). A Landsat-5 atmospheric correction based on MODIS atmosphere products and 6S model. *IEEE Journal of Selected Topics in Applied Earth Observations and Remote Sensing*, *7*(5), 1609–1615.

Hyperspectral Imaging Market | Growth, Trends, and Forecasts (2020-2025). (n.d.). Retrieved January 11, 2021, from https://www.mordorintelligence.com/industry-reports/hyperspectral-imaging-market

Ientilucci, E. J. (2017). Spectral target detection considerations from a physical modeling perspective. *2017 IEEE International Geoscience and Remote Sensing Symposium (IGARSS)*, 1320–1323. https://doi.org/10.1109/IGARSS.2017.8127204

Ientilucci, E. J., & Adler-Golden, S. (2019). Atmospheric Compensation of Hyperspectral Data: An Overview and Review of In-Scene and Physics-Based Approaches. *IEEE Geoscience and Remote Sensing Magazine*, *7*(2), 31–50. https://doi.org/10.1109/MGRS.2019.2904706

Ientilucci, E. J., & Bajorski, P. (2006). *Statistical models for physically derived target sub-spaces* (S. S. Shen & P. E. Lewis, Eds.; p. 63020A). https://doi.org/10.1117/12.679525

Ientilucci, E. J., & Schott, J. R. (2005). Target detection in a structured background environment using an infeasibility metric in an invariant space. *Algorithms and Technologies for Multispectral, Hyperspectral, and Ultraspectral Imagery XI*, *5806*, 491–502.

Iordache, M.-D., Bioucas-Dias, J. M., & Plaza, A. (2011). Sparse Unmixing of Hyperspectral Data. *IEEE Transactions on Geoscience and Remote Sensing*, *49*(6), 2014–2039. https://doi.org/10.1109/TGRS.2010.2098413

Jensen, J. R. (2009). *Remote sensing of the environment: An earth resource perspective 2/e*. Pearson Education India.

Jha, S. S., & Nidamanuri, R. R. (2020). Gudalur Spectral Target Detection (GST-D): A New Benchmark Dataset and Engineered Material Target Detection in Multi-Platform Remote Sensing Data. *Remote Sensing*, *12*(13), 2145. https://doi.org/10.3390/rs12132145

Joshi, N., Baumann, M., Ehammer, A., Fensholt, R., Grogan, K., Hostert, P., Jepsen, M. R., Kuemmerle, T., Meyfroidt, P., Mitchard, E. T., & Reiche, J. (2016). A review of the application of optical and radar remote sensing data fusion to land use mapping and monitoring. *Remote Sensing*, *8*(1), 70.

Kanjir, U., Greidanus, H., & Oštir, K. (2018). Vessel detection and classification from spaceborne optical images: A literature survey. *Remote Sensing of Environment*, *207*, 1–26.

Kaufman, Y. J. (1993). Aerosol optical thickness and atmospheric path radiance. *Journal of Geophysical Research: Atmospheres*, *98*(D2), 2677–2692.

Kaufman, Y. J., & Sendra, C. (1988). Algorithm for automatic atmospheric corrections to visible and near-IR satellite imagery. *International Journal of Remote Sensing*, *9*(8), 1357–1381.

Kay, S. M. (1993). *Fundamentals of statistical signal processing*. Prentice Hall PTR.

Kim, T.-S., Oh, S., Chun, T. B., & Lee, M. (2019). Impact of Atmospheric Correction on the Ship Detection Using Airborne Hyperspectral Image. *IGARSS 2019-2019 IEEE International Geoscience and Remote Sensing Symposium*, 2190–2192.

Kokaly, R. F., Clark, R. N., Swayze, G. A., Livo, K. E., Hoefen, T. M., Pearson, N. C., Wise, R. A., Benzel, W. M., Lowers, H. A., Driscoll, R. L., & Klein, A. J. (2017). *USGS Spectral Library Version*, *7*(No. 1035).

Kolodner, M. A. (2008). Automated target detection system for hyperspectral imaging sensors. *Applied Optics*, *47*(28), F61–F70.

Kotchenova, S. Y., Vermote, E. F., Levy, R., & Lyapustin, A. (2008). Radiative transfer codes for atmospheric correction and aerosol retrieval: Intercomparison study. *Applied Optics*, 2215–2226.

Krawczyk, B. (2016). Learning from imbalanced data: Open challenges and future directions. *Progress in Artificial Intelligence*, *5*(4), 221–232. https://doi.org/10.1007/s13748-016-0094-0

Kruse, F. A. (1988). Minerals Associated With Hydrothermally Altered Rocks. *Remote Sensing of Environment*, *24*, 31–51.

Kruse, F. A., Lefkoff, A. B., Boardman, J. W., Heidebrecht, K. B., Shapiro, A. T., Barloon, P. J., & Goetz, A. F. H. (1993a). The spectral image processing system (SIPS)—Interactive visualization and analysis of imaging spectrometer data. *Remote Sensing of Environment*, *44*(2–3), 145–163.

Kruse, F. A., Lefkoff, A. B., Boardman, J. W., Heidebrecht, K. B., Shapiro, A. T., Barloon, P. J., & Goetz, A. F. H. (1993b). The spectral image processing system

(SIPS)—Interactive visualization and analysis of imaging spectrometer data. *Remote Sensing of Environment*, *44*(2–3), 145–163.

Landgrebe, D. A. (2005). *Signal theory methods in multispectral remote sensing* (Vol. 29). John Wiley & Sons.

Lenoble, J. (1985). *Radiative transfer in scattering and absorbing atmospheres: Standard computational procedures* (Vol. 300). A. Deepak Hampton, Va.

Liang, S. (2005). *Quantitative remote sensing of land surfaces* (Vol. 30). John Wiley & Sons.

Louis, J., Debaecker, V., Pflug, B., Main-Knorn, M., Bieniarz, J., Mueller-Wilm, U., Cadau, E., & Gascon, F. (2016). Sentinel-2 sen2cor: L2a processor for users. *Proceedings Living Planet Symposium 2016*, 1–8.

Makki, I., Younes, R., Francis, C., Bianchi, T., & Zucchetti, M. (2017). A survey of landmine detection using hyperspectral imaging. *ISPRS Journal of Photogrammetry and Remote Sensing*, *124*, 40–53.

Malkmus, W. (1967). Random Lorentz band model with exponential-tailed S- 1 line-intensity distribution function. *JOSA*, *57*(3), 323–329.

Mandanici, E. (2010). Implementation of Hyperion sensor routine in 6SV radiative transfer code. *Proceedings of the Hyperspectral Workshop*.

Manolakis, D. (2005). Taxonomy of detection algorithms for hyperspectral imaging applications. *Optical Engineering*, *44*(6), 066403–066403.

Manolakis, D. (2003). Detection algorithms for hyperspectral imaging applications: A signal processing perspective. *Advances in Techniques for Analysis of Remotely Sensed Data, 2003 IEEE Workshop On*, 378–384. http://ieeexplore.ieee.org/abstract/document/1295218/

Manolakis, D. G., Lockwood, R. B., & Cooley, T. W. (2016). *Hyperspectral imaging remote sensing: Physics, sensors, and algorithms*. Cambridge University Press.

Manolakis, D., Marden, D., & Shaw, G. A. (2003a). Hyperspectral image processing for automatic target detection applications. *Lincoln Laboratory Journal*, *14*(1), 79–116.

Manolakis, D., Marden, D., & Shaw, G. A. (2003b). Hyperspectral image processing for automatic target detection applications. *Lincoln Laboratory Journal*, *14*(1), 79–116.

Marcello, J., Eugenio, F., Perdomo, U., & Medina, A. (2016). Assessment of Atmospheric Algorithms to Retrieve Vegetation in Natural Protected Areas Using Multispectral High Resolution Imagery. *Sensors*, *16*(10), 1624. https://doi.org/10.3390/s16101624

Margalit, A., Reed, I. S., & Gagliardi, R. M. (1985). Adaptive optical target detection using correlated images. *IEEE Transactions on Aerospace and Electronic Systems*, *3*, 394–405.

Martins, V. S., Barbosa, C. C. F., De Carvalho, L. A. S., Jorge, D. S. F., Lobo, F. de L., & Novo, E. M. L. de M. (2017). Assessment of atmospheric correction methods for Sentinel-2 MSI images applied to Amazon floodplain lakes. *Remote Sensing*, *9*(4), 322.

Matteoli, S., Diani, M., & Theiler, J. (2014). An Overview of Background Modeling for Detection of Targets and Anomalies in Hyperspectral Remotely Sensed Imagery. *IEEE Journal of Selected Topics in Applied Earth Observations and Remote Sensing*, *7*(6), 2317–2336. https://doi.org/10.1109/JSTARS.2014.2315772

Matteoli, S., Ientilucci, E. J., & Kerekes, J. P. (2010). Operational and performance considerations of radiative-transfer modeling in hyperspectral target detection. *IEEE Transactions on Geoscience and Remote Sensing*, *49*(4), 1343–1355.

Matteoli, S., Ientilucci, E. J., & Kerekes, J. P. (2009). Comparison of radiative transfer in physics-based models for an improved understanding of empirical hyperspectral data. *2009 First Workshop on Hyperspectral Image and Signal*

Processing: Evolution in Remote Sensing, 1–4. https://doi.org/10.1109/WHISPERS.2009.5288986

McClatchey, R. A., Fenn, R. W., Selby, J. E. A., Volz, F. E., & Garing, J. S. (1971). Optical properties of the atmosphere AFCRL-71-0279. *Environmental Research Paper*, *354*, 108.

McClatchey, R. A., Fenn, R. W., Selby, J. E. A., Volz, F. E., & Garing, J. S. (1972). Optical properties of the atmosphere, AFCRL-72.0497. *Environmental Research Papers*, *411*.

Meerdink, S. K., Hook, S. J., Roberts, D. A., & Abbott, E. A. (2019). The ECOSTRESS spectral library version 1.0. *Remote Sensing of Environment*, *230*, 111196.

Minu, S., Shetty, A., Minasny, B., & Gomez, C. (2017). The role of atmospheric correction algorithms in the prediction of soil organic carbon from Hyperion data. *International Journal of Remote Sensing*, *38*(23), 6435–6456.

Mishra, M. K., Rathore, P. S., Misra, A., & Kumar, R. (2020). Atmospheric Correction of Multispectral VNIR Remote Sensing Data: Algorithm and Inter-sensor Comparison of Aerosol and Surface Reflectance Products. *Earth and Space Science*, *7*(9), e2019EA000710. https://doi.org/10.1029/2019EA000710

Molan, Y. E., Refahi, D., & Tarashti, A. H. (2014). Mineral mapping in the Maherabad area, eastern Iran, using the HyMap remote sensing data. *International Journal of Applied Earth Observation and Geoinformation*, *27*, 117–127.

Moller, F. (1957). Strahlung in der unteren Atmosphare. *Handbuch der Physik*, *48*, 155–253.

Nascimento, J. M., Véstias, M. P., & Martín, G. (2020). Hyperspectral compressive sensing with a system-on-chip FPGA. *IEEE Journal of Selected Topics in Applied Earth Observations and Remote Sensing*, *13*, 3701–3710.

Nia, M. S., Wang, D. Z., Bohlman, S. A., Gader, P. D., Graves, S. J., & Petrovic, M. (2015). Impact of atmospheric correction and image filtering on hyperspectral

classification of tree species using support vector machine. *Journal of Applied Remote Sensing*, *9*(1), 095990. https://doi.org/10.1117/1.JRS.9.095990

Palve, S. N. (2016). The application of remote sensing techniques for air pollution analysis and climate change on Indian subcontinent. *IOP Conference Series: Earth and Environmental Science*, *37*(1), 012076.

Pandya, M. R., Pathak, V. N., Shah, D. B., Trivedi, H. J., Chipade, R. A., Singh, R. P., & Kirankumar, A. S. (2015). Development of a scheme for atmospheric correction of Resourcesat-2 AWiFS data. *International Journal of Applied Earth Observation and Geoinformation*, *40*, 65–73.

Rahman, H. (2001). Influence of atmospheric correction on the estimation of biophysical parameters of crop canopy using satellite remote sensing. *International Journal of Remote Sensing*, *22*(7), 1245–1268.

Ren, H., & Chang, C. I. (2000). Target-constrained interference-minimized approach to subpixel target detection for hyperspectral images. *Optical Engineering*, *39*(12), 3138–3146.

Richter, R., & Schläpfer, D. (2011). Atmospheric/topographic correction for airborne imagery. In *ATCOR-4 user guide* (pp. 565–02).

Roberts, D. A., Yamaguchi, Y., & Lyon, R. J. P. (1986). Comparison of various techniques for calibration of AIS data. *NASA STI/Recon Technical Report N*, *87*, 21–30.

Robila, S. A., & Gershman, A. (2005). Spectral matching accuracy in processing hyperspectral data. *IEEE International Symposium on Signals, Circuits and Systems, 2005. ISSCS 2005*, *1*, 163–166.

Sabater, N., Vicent, J., Alonso, L., Cogliati, S., Verrelst, J., & Moreno, J. (2017). Impact of Atmospheric Inversion Effects on Solar-Induced Chlorophyll Fluorescence: Exploitation of the Apparent Reflectance as a Quality Indicator. *Remote Sensing*, *9*(6), 622. https://doi.org/10.3390/rs9060622

Scharf, L. L., & McWhorter, L. T. (1996). Adaptive matched subspace detectors and adaptive coherence estimators. *Conference Record of the Thirtieth Asilomar IEEE Conference on Signals, Systems and Computers*, 1114–1117.

Schläpfer, D., Borel, C. C., Keller, J., & Itten, K. I. (1998). Atmospheric precorrected differential absorption technique to retrieve columnar water vapor. *Remote Sensing of Environment*, *65*(3), 353–366.

Seong, N.-H., Jung, D., Kim, J., & Han, K.-S. (2020). Evaluation of NDVI Estimation Considering Atmospheric and BRDF Correction through Himawari-8/AHI. *Asia-Pacific Journal of Atmospheric Sciences*, *56*(2), 265–274. https://doi.org/10.1007/s13143-019-00167-0

Smith, G. M., & Milton, E. J. (1999). The use of the empirical line method to calibrate remotely sensed data to reflectance. *International Journal of Remote Sensing*, *20*(13), 2653–2662. https://doi.org/10.1080/014311699211994

Snyder, D., Kerekes, J., Fairweather, I., Crabtree, R., Shive, J., & Hager, S. (2008a). Development of a web-based application to evaluate target finding algorithms. *IGARSS 2008-IEEE International Geoscience and Remote Sensing Symposium*, *2*, 915.

Snyder, D., Kerekes, J., Fairweather, I., Crabtree, R., Shive, J., & Hager, S. (2008b). Development of a web-based application to evaluate target finding algorithms. *IGARSS 2008-IEEE International Geoscience and Remote Sensing Symposium*, *2*, 915.

Sundberg, R. (2018). The Impact of Cloud Shadows on Subpixel Target Detection. *2018 9th Workshop on Hyperspectral Image and Signal Processing: Evolution in Remote Sensing (WHISPERS)*, 1–5.

Theiler, J., Ziemann, A., Matteoli, S., & Diani, M. (2019). Spectral variability of remotely sensed target materials: Causes, models, and strategies for mitigation and robust exploitation. *IEEE Geoscience and Remote Sensing Magazine*, *7*(2), 8–30.

Themistocleous, K., Hadjimitsis, D., Retalis, A., & Chrysoulakis, N. (2012). Development of a new image based atmospheric correction algorithm for aerosol optical thickness retrieval using the darkest pixel method. *Journal of Applied Remote Sensing*, *6*, 1–12. https://doi.org/10.1117/1.JRS.6.063538

Thompson, D. R., Gao, B. C., Green, R. O., Roberts, D. A., Dennison, P. E., & Lundeen, S. R. (2015). Atmospheric correction for global mapping spectroscopy: ATREM advances for the HyspIRI preparatory campaign. *Remote Sensing of Environment*, *167*, 64–77.

Thompson, D. R., Guanter, L., Berk, A., Gao, B.-C., Richter, R., Schläpfer, D., & Thome, K. J. (2019). Retrieval of atmospheric parameters and surface reflectance from visible and shortwave infrared imaging spectroscopy data. *Surveys in Geophysics*, *40*(3), 333–360.

Tirelli, C., Curci, G., Manzo, C., Tuccella, P., & Bassani, C. (2015). Effect of the aerosol model assumption on the atmospheric correction over land: Case studies with CHRIS/PROBA hyperspectral images over Benelux. *Remote Sensing*, *7*(7), 8391–8415.

Trym Vegard Haavardsholm, Torbjorn Skauli, & Ingebjorg Kasen. (2007). A physics-based statistical signature model for hyperspectral target detection. *2007 IEEE International Geoscience and Remote Sensing Symposium*, 3198–3201. https://doi.org/10.1109/IGARSS.2007.4423525

van der Meer, F. (2006). The effectiveness of spectral similarity measures for the analysis of hyperspectral imagery. *International Journal of Applied Earth Observation and Geoinformation*, *8*(1), 3–17. https://doi.org/10.1016/j.jag.2005.06.001

Vermote, E. F. T. D., Tanré, D., Deuzé, J. L., Herman, M., Morcrette, J. J., & Kotchenova, S. Y. (2006). Second simulation of a satellite signal in the solar spectrum-vector (6SV. *6S User Guide Version*, *3*, 1–55.

Vermote, E. F., Tanre, D., Deuze, J. L., Herman, M., & Morcette, J.-J. (1997). Second Simulation of the Satellite Signal in the Solar Spectrum, 6S: An overview. *IEEE Transactions on Geoscience and Remote Sensing*, *35*(3), 675–686. https://doi.org/10.1109/36.581987

Wang, Z., & Xue, J.-H. (2017). The matched subspace detector with interaction effects. *Pattern Recognition*, *68*, 24–37. https://doi.org/10.1016/j.patcog.2017.03.002

Wilson, R. T. (2013). Py6S: A Python interface to the 6S radiative transfer model. *Computers & Geosciences*, *51*(2), 166.

Wilson, R. T., Milton, E. J., & Nield, J. M. (2015). Are visibility-derived AOT estimates suitable for parameterizing satellite data atmospheric correction algorithms? *International Journal of Remote Sensing*, *36*(6), 1675–1688. https://doi.org/10.1080/01431161.2015.1023558

Wood, L. (1989). *Survey of ERIM approaches applicable to semi-automatic target detection and cueing for multispectral and multisensor exploitation*. Environmental Research Inst of Michigan Ann Arbor.

Yadav, D., Arora, M. K., Tiwari, K. C., & Ghosh, J. K. (2018a). Parameters affecting target detection in VNIR and SWIR range. *The Egyptian Journal of Remote Sensing and Space Science*, *21*(3), 325–333.

Yadav, D., Arora, M. K., Tiwari, K. C., & Ghosh, J. K. (2018b). Parameters affecting target detection in VNIR and SWIR range. *The Egyptian Journal of Remote Sensing and Space Science*, *21*(3), 325–333.

Yarbrough, A. W., Mendenhall, M. J., & Martin, R. K. (2010). The effects of atmospheric mis-estimation on hyperspectral-based adaptive matched filter target detection as measured by the bhattacharyya coefficient. *2010 2nd Workshop on Hyperspectral Image and Signal Processing: Evolution in Remote Sensing*, 1–4.

Yuen, P. W., & Richardson, M. (2010). An introduction to hyperspectral imaging and its application for security, surveillance and target acquisition. *The Imaging Science Journal*, *58*(5), 241–253.

Zhang, L., Zhang, L., Tao, D., Huang, X., & Du, B. (2014). Hyperspectral Remote Sensing Image Subpixel Target Detection Based on Supervised Metric Learning. *IEEE Transactions on Geoscience and Remote Sensing*, *52*(8), 4955–4965. https://doi.org/10.1109/TGRS.2013.2286195

LIST OF PUBLICATIONS BASED ON THESIS

Papers in peer reviewed international journals

1. **Jha, S. S.**, Manohar Kumar, C. V. S. S., & Nidamanuri, R. R. (2019). Flexible atmospheric compensation technique (FACT): a 6S based atmospheric correction scheme for remote sensing data. ***Geocarto International***, 1-19.
2. **Jha, S. S.**, & Nidamanuri, R. R. (2020). Gudalur Spectral Target Detection (GST-D): A New Benchmark Dataset and Engineered Material Target Detection in Multi-Platform Remote Sensing Data. ***Remote Sensing***, 12(13), 2145.
3. **Jha, S. S.**, Kumar, M., & Nidamanuri, R. R. (2020). Multi-platform optical remote sensing dataset for target detection. ***Data in Brief***, *33*, 106362.
4. **Jha S.S.**, Nidamanuri R.R. (2020). Dynamics of target detection using drone based hyperspectral imagery. In: Jain K., Khoshelham K., Zhu X., Tiwari A. (Eds). Lecture Notes in Civil Engineering, Vol 51. **Springer**, https://doi.org/10.1007/978-3-030-37393-1_10
5. **Jha, S. S.,** Nidamanuri, R. R., and Emmett J. I. (2021). Influence of atmospheric modelling on spectral target detection in multi-platform remote sensing data. ***ISPRS Journal of Photogrammetry and Remote Sensing (in review).***

Conference Proceedings

1. **Jha, S.S.** and Nidamanuri R.R. (2020). Repercussions of inconsistent atmospheric modelling on spectral target detection performance in a multi-platform remote sensing data, IEEE India Geoscience and Remote Sensing Young Researchers Conclave 2020, 18-20, Dec. 2020 **(won the best oral presentation under the theme: Methods and Algorithms)**.
2. **Jha, S. S.**, & Nidamanuri, R. R. (2019). Dynamics of target detection using drone based hyperspectral imagery. In International Conference on Unmanned Aerial System in Geomatics (pp. 91-97). Springer, Cham.